

3 Fermi Large Area Telescope Fourth Source Catalog

4 THE *Fermi*-LAT COLLABORATION

5 ABSTRACT

6 We distribute a new release of the fourth *Fermi* Large Area Telescope source catalog
7 (4FGL) containing spectral energy distributions averaged over 8 years and light curves
8 with 1-year intervals. This supersedes the FL8Y source list distributed in 2018^{a)}.

9 Based on the first eight years of science data from the *Fermi* Gamma-ray Space
10 Telescope mission in the energy range from 50 MeV to 1 TeV, it is the deepest yet
11 in this energy range. Relative to the 3FGL catalog, the 4FGL catalog has twice as
12 much exposure as well as a number of analysis improvements, including an updated
13 model for the Galactic diffuse γ -ray emission. The 4FGL catalog includes 5065
14 sources above 4σ significance, for which we provide localization and spectral properties.
15 Seventy-five sources are modeled explicitly as spatially extended, and overall 355
16 sources are considered as identified based on angular extent, periodicity or correlated
17 variability observed at other wavelengths. For 1323 sources we have not found plausible
18 counterparts at other wavelengths. More than 3130 of the identified or associated
19 sources are active galaxies of the blazar class, and 239 are pulsars.

20 *Keywords:* Gamma rays: general — surveys — catalogs

21 1. INTRODUCTION

22 This document presents the fourth catalog of high-energy γ -ray sources (4FGL) detected in the
23 first eight years of the *Fermi* Gamma-ray Space Telescope mission by the Large Area Telescope
24 (LAT). The list is final and this version contains all the source information usually released in Fermi
25 catalogs, although the light curves with small intervals are still missing. A detailed comparison with
26 previous *Fermi*-LAT catalogs and the careful assessment of c sources (probably related to imperfect
27 modeling of diffuse emission) are also deferred to a future release. As in the Third LAT Source
28 Catalog (hereafter 3FGL, [Acero et al. 2015](#)) sources are included based on the statistical significance
29 of their detection considered over the entire time period of the analysis. For this reason the 4FGL
30 catalog does not contain transient γ -ray sources which are only significant over a short duration (such
31 as γ -ray bursts, solar flares, most novae).

32 The 4FGL catalog builds on several generations of *Fermi*-LAT catalogs (Table 1). It benefits from
33 a number of improvements with respect to the 3FGL, besides the twice longer exposure:

- 34 1. Pass 8 data¹ were used (§ 2.2). The principal difference relative to the P7REP data used for
35 3FGL is about 20% larger acceptance at all energies and improved angular resolution above 3
36 GeV.

^{a)} See <https://fermi.gsfc.nasa.gov/ssc/data/access/lat/fl8y/>.

¹ See http://fermi.gsfc.nasa.gov/ssc/data/analysis/documentation/Pass8_usage.html.

Acronym	Data/IRF/Diffuse model	Energy range/Duration	Sources	Analysis/Reference
1FGL	P6_V3_DIFFUSE gll_iem_v02	0.1 – 100 GeV 11 months	1451 point	Unbinned, F/B Abdo et al. (2010a)
2FGL	P7SOURCE_V6 gal_2yearp7v6_v0	0.1 – 100 GeV 2 years	1873 point	Binned, F/B Nolan et al. (2012)
3FGL	P7REP_SOURCE_V15 gll_iem_v06	0.1 – 300 GeV 4 years	3033 point	Binned, F/B Acero et al. (2015)
FGES	P8R2_SOURCE_V6 gll_iem_v06	10 GeV – 2 TeV 6 years	46 extended	Binned, PSF, $ b < 7^\circ$ Ackermann et al. (2017)
3FHL	P8R2_SOURCE_V6 gll_iem_v06	10 GeV – 2 TeV 7 years	1556 point	Unbinned, PSF Ajello et al. (2017)
FHES	P8R2_SOURCE_V6 gll_iem_v06	1 GeV – 1 TeV 7.5 years	24 extended	Binned, PSF, $ b > 5^\circ$ Ackermann et al. (2018)
4FGL	P8R3_SOURCE_V2 new (§ 2.4.1)	0.05 GeV – 1 TeV 8 years	5098 point	Binned, PSF this work

Table 1. The table describes the previous *Fermi*-LAT catalogs mentioned in the text. In the Analysis column, F/B stands for *Front/Back*, and PSF for PSF event types^a. In the Sources column, point or extended refer to the catalog’s objective.

^aSee https://fermi.gsfc.nasa.gov/ssc/data/analysis/LAT_essentials.html.

- 37 2. A new model of the underlying diffuse Galactic emission (§ 2.4) was developed.
- 38 3. We introduced weights in the maximum likelihood analysis (§ 3.2) in order to mitigate the
- 39 effect of systematic errors due to our imperfect knowledge of the Galactic diffuse emission.
- 40 4. We explicitly modeled 75 sources as extended emission regions (§ 3.4), up from 25 in 3FGL.
- 41 5. To study the associations of LAT sources with counterparts at other wavelengths, we updated
- 42 several of the counterpart catalogs, and correspondingly recalibrated the association procedure.
- 43 Section 2 describes the LAT, the data, and the models for the diffuse backgrounds, celestial and
- 44 otherwise. Section 3 describes the construction of the catalog, with emphasis on what has changed
- 45 since the analysis for the 3FGL catalog. Section 4 describes the catalog itself, while § 5 details the
- 46 associations and identifications. We provide appendices with technical details of the analysis and of
- 47 the format of the electronic version of the catalog.

48 2. INSTRUMENT & BACKGROUND

49 2.1. *The Large Area Telescope*

50 The LAT detects γ rays in the energy range 20 MeV to more than 1 TeV, measuring their arrival
51 times, energies, and directions. The field of view of the LAT is 2.4 sr at 1 GeV. The per-photon angular
52 resolution (point-spread function, PSF, 68% containment radius) is $\sim 5^\circ$ at 100 MeV, decreasing to
53 0.8° at 1 GeV (averaged over the acceptance of the LAT), varying with energy approximately as $E^{-0.8}$
54 and asymptoting at $\sim 0.1^\circ$ above 20 GeV². The tracking section of the LAT has 36 layers of silicon

² See http://www.slac.stanford.edu/exp/glast/groups/canda/lat_Performance.htm.

55 strip detectors interleaved with 16 layers of tungsten foil (12 thin layers, 0.03 radiation length, at
 56 the top or *Front* of the instrument, followed by 4 thick layers, 0.18 radiation lengths, in the *Back*
 57 section). The silicon strips track charged particles, and the tungsten foils facilitate conversion of γ
 58 rays to positron-electron pairs. Beneath the tracker is a calorimeter composed of an 8-layer array of
 59 CsI crystals (~ 8.5 total radiation lengths) to determine the γ -ray energy. More information about
 60 the LAT is provided in [Atwood et al. \(2009\)](#), and the in-flight calibration of the LAT is described in
 61 [Abdo et al. \(2009a\)](#), [Ackermann et al. \(2012a\)](#) and [Ackermann et al. \(2012b\)](#).

62 The LAT is also an efficient detector of the intense background of charged particles from cosmic
 63 rays and trapped radiation at the orbit of the *Fermi* satellite. A segmented charged-particle
 64 anticoincidence detector (plastic scintillators read out by photomultiplier tubes) around the tracker
 65 is used to reject charged-particle background events. Accounting for γ rays lost in filtering charged
 66 particles from the data, the effective collecting area is ~ 8000 cm² at 1 GeV at normal incidence (for
 67 the P8R3_SOURCE_V2 event selection used here; see below). The live time is nearly 76%, limited
 68 primarily by interruptions of data taking when *Fermi* is passing through the South Atlantic Anomaly
 69 ($\sim 15\%$) and readout dead-time fraction ($\sim 9\%$).

70 2.2. The LAT Data

71 The data for the 4FGL catalog were taken during the period 2008 August 4 (15:43 UTC) to 2016
 72 August 2 (05:44 UTC) covering eight years. As for 3FGL, intervals around solar flares and bright
 73 GRBs were excised. Overall about two days were excised due to solar flares, and 39 ks due to 30
 74 GRBs. The precise time intervals corresponding to selected events are recorded in the GTI extension
 75 of the FITS file (Appendix A). The maximum exposure (4.5×10^{11} cm² s at 1 GeV) is reached at the
 76 North celestial pole. The minimum exposure (2.7×10^{11} cm² s at 1 GeV) is reached at the celestial
 77 equator.

78 The current version of the LAT data is Pass 8 P8R3 ([Atwood et al. 2013](#); [Bruehl et al. 2018](#)). It
 79 offers 20% more acceptance than P7REP ([Bregeon et al. 2013](#)) and a narrower PSF at high energies.
 80 Both aspects are very useful for source detection and localization ([Ajello et al. 2017](#)). We used the
 81 Source class event selection, with the Instrument Response Function (IRF) P8R3_SOURCE_V2.
 82 We took advantage of the new PSF event types, which avoid mixing poorly localized events (PSF0)
 83 with high-quality ones (PSF3).

84 The lower bound of the energy range was set to 50 MeV, down from 100 MeV in 3FGL, in order to
 85 constrain the spectra better at low energy. It does not help detecting or localizing sources because of
 86 the very broad PSF below 100 MeV. The upper bound was raised from 300 GeV in 3FGL to 1 TeV.
 87 This is because as the source-to-background ratio decreases, the sensitivity curve (Figure 18 of [Abdo
 88 et al. 2010a](#), 1FGL) shifts to higher energies. The 3FHL catalog ([Ajello et al. 2017](#)) went up to 2 TeV,
 89 but only 566 events exceed 1 TeV over 8 years (to be compared to 714 thousands above 10 GeV).

90 2.3. Zenith angle selection

91 The zenith angle cut was set such that the contribution of the Earth limb at that zenith angle was
 92 less than 10% of the total (Galactic + isotropic) background. Integrated over all zenith angles, the
 93 residual Earth limb contamination is less than 1%. We kept PSF3 event types with zenith angles
 94 less than 80° between 50 and 100 MeV, PSF2 and PSF3 event types with zenith angles less than
 95 90° between 100 and 300 MeV, and PSF1, PSF2 and PSF3 event types with zenith angles less than

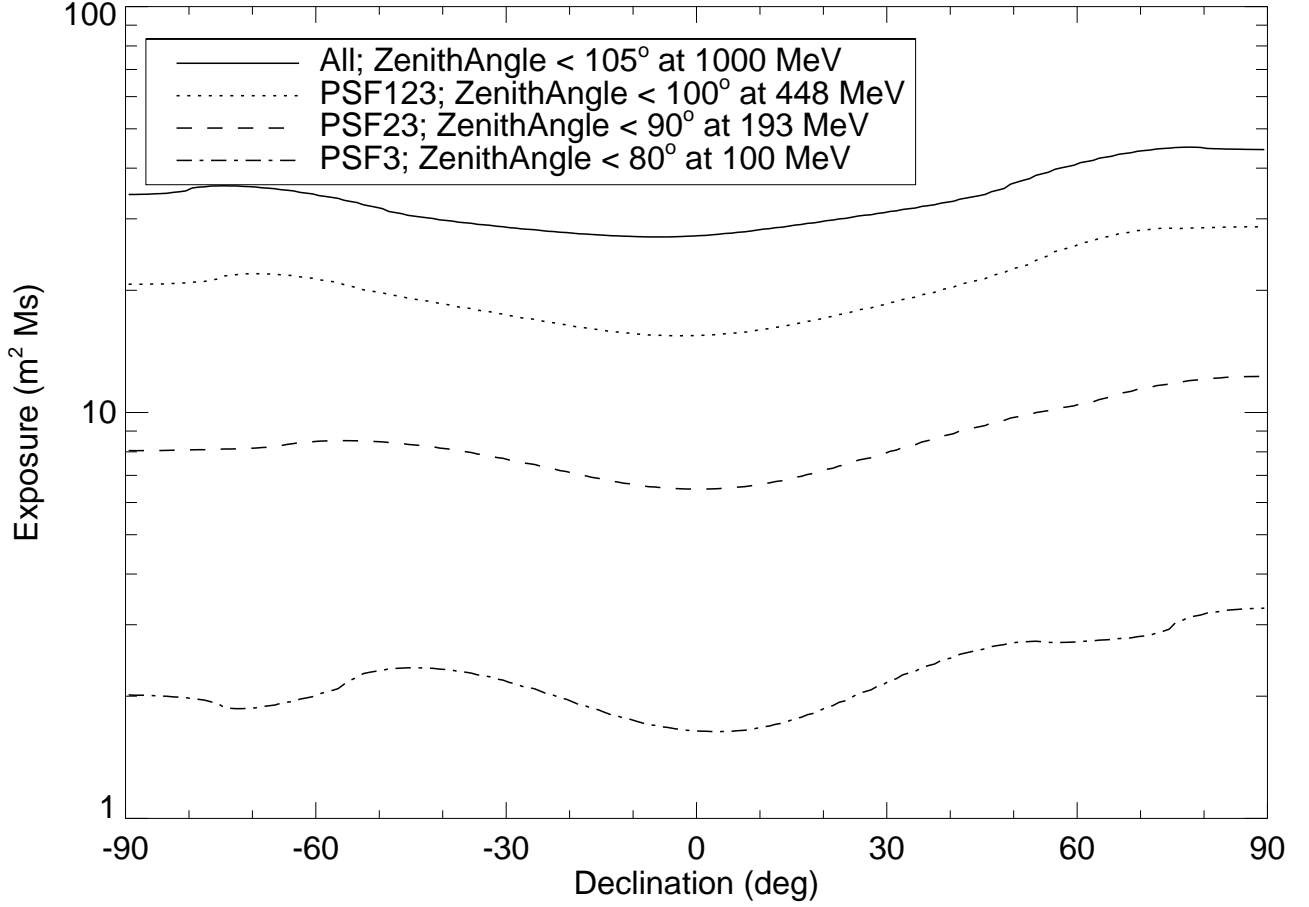


Figure 1. Exposure as a function of declination and energy, averaged over right ascension, summed over all relevant event types as indicated in the figure legend.

96 100° between 300 MeV and 1 GeV. Above 1 GeV we kept all events with zenith angles less than 105°
 97 (Table 2).

98 The resulting integrated exposure over 8 years is shown in Figure 1. The dependence on declination
 99 is due to the combination of the inclination of the orbit, the rocking angle, and the off-axis effective
 100 area. The north-south asymmetry is due to the South-Atlantic Anomaly over which the instrument
 101 is switched off. Because of the regular precession of the orbit every 53 days, the dependence on right
 102 ascension is small when averaged over long periods of time. The dependence on energy is due to the
 103 increase of the effective area up to 1 GeV, and the addition of new event types at 100 MeV, 300 MeV
 104 and 1 GeV. The off-axis effective area depends somewhat on energy and event type. This introduces
 105 a slight dependence of the shape of the curve on energy.

106 Selecting on zenith angle applies a kind of time selection (which depends on direction in the sky).
 107 This means that the effective time selection at low energy is not exactly the same as at high energy.
 108 The periods of time during which a source is at zenith angle $< 105^\circ$ but (for example) $> 90^\circ$
 109 last typically a few minutes every orbit. This is shorter than the main variability time scales of
 110 astrophysical sources, and therefore not a concern. There remains however the modulation due to
 111 the precession of the spacecraft orbit on longer time scales over which blazars can vary. This is not

Energy interval (GeV)	NBins	ZMax (deg)	Ring width (deg)	Pixel size (deg)				
				PSF0	PSF1	PSF2	PSF3	All
0.05 – 0.1	3	80	7	0.6	
0.1 – 0.3	5	90	7	0.6	0.6	
0.3 – 1	6	100	5	...	0.4	0.3	0.2	
1 – 3	5	105	4	0.4	0.15	0.1	0.1	
3 – 10	6	105	3	0.25	0.1	0.05	0.04	
10 – 1000	10	105	2	0.04

Table 2. The 15 components (all in binned mode) of the Summed Likelihood approach used in 4FGL. Components in a given energy interval share the same number of energy bins, the same zenith angle selection and the same RoI size, but have different pixel sizes in order to adapt to the PSF width. Each filled entry under Pixel size corresponds to one component of the summed likelihood. NBins is the number of energy bins in the interval, ZMax is the zenith angle cut, Ring width refers to the difference between the RoI core and the extraction region, as explained in item 5 of § 3.2.

112 a problem for a catalog (it can at most appear as a spectral effect, and should average out when
 113 considering statistical properties) but it should be kept in mind when extracting spectral parameters
 114 of individual variable sources. We used the same zenith angle cut for all event types in a given energy
 115 interval in order to reduce systematics due to that time selection.

116 Because the data are limited by systematics at low energies everywhere in the sky (Appendix B)
 117 rejecting half of the events below 300 MeV and 75% of them below 100 MeV does not impact the
 118 sensitivity (if we had kept these events, the weights would have been lower).

119 2.4. Model for the Diffuse Gamma-Ray Background

120 2.4.1. Diffuse emission of the Milky Way

121 We extensively updated the model of the Galactic diffuse emission for the 4FGL analysis, using the
 122 same P8R3 data selections (PSF types, energy ranges, and zenith angle limits). The development
 123 of the model will be described in detail elsewhere. Here we summarize the primary differences from
 124 the model developed for the 3FGL catalog (Acero et al. 2016a). In both cases, the model is based
 125 on linear combinations of templates representing components of the Galactic diffuse emission. For
 126 4FGL we updated all of the templates, and added a new one as described below.

127 We have adopted the new, all-sky high-resolution, 21-cm spectral line HI4PI survey (HI4PI
 128 Collaboration et al. 2016) as our tracer of H I, and extensively refined the procedure for partitioning
 129 the H I and H₂ (traced by the 2.6-mm CO line) into separate ranges of Galactocentric distance
 130 (‘rings’), by decomposing the spectra into individual line profiles, so the broad velocity dispersion of
 131 massive interstellar clouds does not effectively distribute their emission very broadly along the line of
 132 sight. We also updated the rotation curve, and adopted a new procedure for interpolating the rings
 133 across the Galactic center and anticenter, now incorporating a general model for the surface density
 134 distribution of the interstellar medium to inform the interpolation, and defining separate rings for
 135 the Central Molecular Zone (within ~150 pc of the Galactic center and between 150 pc and 600 pc
 136 of the center). With this approach, the Galaxy is divided into ten concentric rings.

137 The template for the inverse Compton emission is still based on a model interstellar radiation field
 138 and cosmic-ray electron distribution (calculated in GALPROP v56, described in Porter et al. 2017)³
 139 but now we formally subdivide the model into rings (with the same Galactocentric radius ranges as
 140 for the gas templates), which are fit separately in the analysis, to allow some spatial freedom relative
 141 to the static all-sky inverse-Compton model.

142 We have also updated the template of the ‘dark gas’ component, representing interstellar gas that
 143 is not traced by the HI and CO line surveys, by comparison with the *Planck* dust optical depth map⁴.
 144 The dark gas is inferred as the residual component after the best-fitting linear combination of total
 145 $N(\text{HI})$ and W_{CO} are subtracted, i.e., as the component not correlated with the atomic and molecular
 146 gas spectral line tracers, in a procedure similar to that used in Acero et al. (2016a). In particular, as
 147 before we retained the negative residuals as a ‘column density correction map’.

148 New with the 4FGL model we incorporated a template representing the contribution of unresolved
 149 Galactic sources, derived based on a model spatial distribution and luminosity function developed
 150 based on the distribution of Galactic sources in Acero et al. (2015) and an analytical evaluation of
 151 the flux limit for source detection as a function of direction on the sky.

152 As for the 3FGL-era model, we iteratively determined and re-fit a model component that represents
 153 non-template diffuse γ -ray emission, primarily Loop I and the *Fermi* bubbles. To avoid overfitting
 154 the residuals, and possibly suppressing faint Galactic sources, we spectrally and spatially smoothed
 155 the residual template.

156 The model fitting was performed using Gardian (Ackermann et al. 2012c), as a summed likelihood
 157 analysis. This procedure involves transforming the ring maps described above into spatial-spectral
 158 templates evaluated in GALPROP. We used model $^S\text{L}^Z\text{G}^R\text{30}^T\text{150}^C\text{2}$ from Ackermann et al. (2012c).
 159 The model is a linear combination of these templates, with free scaling functions of various forms
 160 for the individual templates. For components with the largest contributions, a piecewise continuous
 161 function, linear in the logarithm of energy, with nine degrees of freedom was used. Other components
 162 had a similar scaling function with five degrees of freedom, or power-law scaling, or overall scale
 163 factors, chosen to give the model adequate freedom while reducing the overall number of free
 164 parameters. The model also required a template for the point and small-extended sources in the
 165 sky. We iterated the fitting using preliminary versions of the 4FGL catalog. This template was
 166 also given spectral degrees of freedom. Other diffuse templates, described below and not related to
 167 Galactic emission, were included in the model fitting.

168 2.4.2. Isotropic background

169 The isotropic diffuse background was derived from fits to the eight-year data set excluding the
 170 Galactic plane ($|b| > 10^\circ$) using the Galactic diffuse emission model described above and a preliminary
 171 version of the 4FGL catalog. The diffuse background includes charged particles misclassified as γ
 172 rays. We implicitly assume that the acceptance for these residual charged particles is the same as
 173 for γ rays in treating these diffuse background components together. For the analysis we derived the
 174 contributions to the isotropic background separately for all event types.

175 2.4.3. Solar and lunar template

³ <http://galprop.stanford.edu>

⁴ COM_CompMap_Dust-GNILC-Model-Opacity_2048_R2.01.fits, Planck Collaboration et al. (2016)

176 The quiescent Sun and the Moon are fairly bright γ -ray sources. The Sun moves in the ecliptic but
 177 the solar γ -ray emission is extended because of cosmic-ray interactions with the solar radiation field;
 178 detectable emission from inverse Compton scattering of cosmic-ray electrons on the radiation field
 179 of the Sun extends several degrees from the Sun (Abdo et al. 2011). The Moon is not an extended
 180 source in this way but the lunar orbit is inclined somewhat relative to the ecliptic and the Moon
 181 moves through a larger fraction of the sky than the Sun. Averaged over time, the γ -ray emission
 182 from the Sun and Moon trace a region around the ecliptic. Without any correction this can seriously
 183 affect the spectra and light curves, so starting with 3FGL we model that emission.

184 The Sun and Moon emission are modulated by the solar magnetic field which deflects cosmic rays
 185 more (and therefore reduces γ -ray emission) when the Sun is at maximum activity. For that reason
 186 the model used in 3FGL (based on the first 18 months of data when the Sun was near minimum) was
 187 not adequate for 8 years. We used the improved model of the Moon (Ackermann et al. 2016a) and
 188 a data-based model of the solar disk and inverse Compton scattering on the solar light (S. Raino,
 189 private communication).

190 We combined those models with calculations of their motions and of the exposure of the observations
 191 by the LAT to make templates for the equivalent diffuse component over 8 years using *gtsuntemp*
 192 (Johannesson et al. 2013). For 4FGL we used two different templates: one for the inverse Compton
 193 emission on the solar light (pixel size $0^\circ 25'$) and one for the sum of the solar and lunar disks. For the
 194 latter we reduced the pixel size to $0^\circ 125'$ in order to describe the disks accurately, and computed a
 195 specific template for each event type / maximum zenith angle combination of Table 2 (because their
 196 exposure maps are not identical). As for 3FGL those components have no free parameter.

197 2.4.4. Residual Earth limb template

198 For 3FGL we reduced the low-energy Earth limb emission by selecting zenith angles less than 100° ,
 199 and modeled the residual contamination approximately. For 4FGL we chose to cut harder on zenith
 200 angle at low energies and select event types with the best PSF (§ 2.3). That procedure eliminates
 201 the need for a specific Earth limb component in the model.

202 3. CONSTRUCTION OF THE CATALOG

203 The procedure used to construct the 4FGL catalog has a number of improvements relative to that
 204 of the 3FGL catalog. In this section we review the procedure, emphasizing what was done differently.
 205 The significances (§ 3.2) and spectral parameters (§ 3.3) of all catalog sources were obtained using
 206 the standard *pyLikelihood* framework (Python analog of *gtlike*) in the LAT Science Tools⁵ (version
 207 v11r7p0). The localization procedure (§ 3.1), which relies on *pointlike*, provided the source positions,
 208 the starting point for the spectral fitting, and a comparison for estimating the reliability of the results
 209 (§ 3.7.2).

210 Throughout the text we denote as RoIs, for Regions of Interest, the regions in which we extract
 211 the data. We use the Test Statistic $TS = 2(\log \mathcal{L} - \log \mathcal{L}_0)$ (Mattox et al. 1996) to quantify how
 212 significantly a source emerges from the background, comparing the maximum value of the likelihood
 213 function \mathcal{L} over the RoI including the source in the model with \mathcal{L}_0 , the value without the source.

214 3.1. Detection and Localization

⁵ See <http://fermi.gsfc.nasa.gov/ssc/data/analysis/documentation/Cicerone/>.

215 This section describes the generation of a list of candidate sources, with locations and initial spectral
 216 fits. This initial stage uses *pointlike* (Kerr 2010). Compared with the *gtlike*-based analysis described
 217 in § 3.2 to 3.7, it uses the same time range and IRFs, but the partitioning of the sky, the weights,
 218 the computation of the likelihood function and its optimization are independent. Energy dispersion
 219 is neglected. Events below 100 MeV are useless for source detection and localization, and are ignored
 220 at this stage. Since this version of the computation of the likelihood function is used for localization,
 221 it needs to represent a valid estimate of the probability of observing a point source with the assumed
 222 spectral function.

223 The process started with an initial set of sources from the 3FGL analysis, not just those reported in
 224 that catalog, but also including all candidates failing the significance threshold (i.e., with $10 < TS <$
 225 25). It used the 75 spatially extended sources listed in § 3.4, and the three-source representation
 226 of the Crab (§ 3.3). The same spectral models were considered for each source as in § 3.3, but the
 227 favored model (power law or curved) was not necessarily the same.

228 The generation of a candidate list of sources, with locations and initial spectral fits is substantially
 229 the same as for 3FGL. The sky was partitioned using HEALPix⁶ (Górski et al. 2005) with $N_{\text{side}} = 12$,
 230 resulting in 1728 tiles of ~ 25 deg² area. The RoIs included events in cones of 5° radius about the
 231 center of the tiles. The data were binned into 16 energy bands from 100 MeV to 1 TeV (up from
 232 14 bands to 316 GeV in 3FGL), and, as before, separated into the *Front* and *Back* event types.
 233 However, only *Front* events were used below 316 MeV, to avoid the poor PSF and contribution of
 234 the Earth limb. All sources within the tile and those nearby, in the adjacent and second rings, were
 235 included in the model. Only the spectral models and positions of sources within the central tile were
 236 allowed to vary to optimize the likelihood. To account for correlations with fixed nearby sources,
 237 and a factor of three overlap for the data, iterations were performed until log likelihoods for all RoIs
 238 changed by less than 10.

239 We assumed here that the isotropic spectrum was exactly constant over the sky, but readjusted the
 240 Galactic diffuse emission. Starting with a version of the Galactic diffuse model (§ 2.4.1) without its
 241 non-template diffuse γ -ray emission, we derived an alternative adjustment by optimizing the Galactic
 242 diffuse normalization for each RoI and the eight bands below 10 GeV. These numbers were turned into
 243 an 8-layer map which was smoothed, then applied to the diffuse model itself. Then the corrections
 244 were measured again. This process converged after two iterations, such that no more corrections
 245 were needed. The advantage of the procedure, compared to fitting parameters in each RoI (§ 3.2), is
 246 that the effective predictions do not vary abruptly from an RoI to its neighbors.

247 After a set of iterations had converged, the localization procedure was applied, and source positions
 248 updated for a new set of iterations. At this stage, new sources were occasionally added using the
 249 residual *TS* procedure described below. The detection and localization process resulted in ~ 8020
 250 candidate point sources with $TS > 10$. The fit validation and likelihood weighting were done as in
 251 3FGL.

252 3.1.1. Detection of additional sources

253 As for 3FGL, the same implementation of the likelihood used for optimizing source parameters was
 254 used to test for the presence of additional point sources. This is inherently iterative, in that the
 255 likelihood is valid to the extent that it represents an accurate measure of the model prediction. Thus

⁶ <http://healpix.sourceforge.net>.

α	β	E_0 (GeV)	Comment
1.7	0.0	50.00	Hard
2.2	0.0	1.00	Intermediate
2.7	0.0	0.25	Soft
2.0	0.5	2.00	Curved, but not a pulsar
2.0	0.3	1.00	Pulsar-like

Table 3. The table describes the five spectral shapes used for source finding in 4FGL. The spectral parameters α , β and E_0 refer to the LogParabola spectral shape (Eq. 2).

256 source detection depends on having nearby stronger sources already included. Since 3FGL was based
 257 on four years of data, one can expect many more sources. As we accumulated more and more data
 258 since then, the source list gradually evolved. A measure of success is that subsequent source finding
 259 adds little to the total. As before, an iteration starts with choosing a HEALPix $N_{side} = 128$ grid,
 260 3.1 M points with average separation 0.15 degrees. But now, instead of testing a single power-law
 261 spectrum, we try five spectral shapes; three are power laws with different indices, two with significant
 262 curvature. Table 3 lists the spectral shapes used for the templates.

263 For each trial position, and each of the five templates, the normalizations were optimized, and
 264 the resulting TS associated with the pixel. Then, as before, but independently for each template, a
 265 cluster analysis selected groups of pixels with $TS > 16$, as compared to $TS > 10$ for 3FGL. Each
 266 cluster defined a seed, with a position defined by weighting the TS values. Finally, the five sets of
 267 potential seeds were compared, and, for those within 1° , the seed with the largest TS was selected
 268 for inclusion.

269 3.1.2. Localization

270 The position of each source was determined by maximizing the likelihood with respect to its position
 271 only. That is, all other parameters are kept fixed. The possibility that a shifted position would affect
 272 the spectral models or positions of nearby sources is accounted for by iteration. Ideally the log
 273 likelihood is a quadratic form in any pair of angular variables, assuming small angular offsets. We
 274 define LTS, for Localization Test Statistic, to be twice the log of the likelihood ratio of any position
 275 with respect to the maximum; the LTS evaluated for a grid of positions is called an LTS map. We fit
 276 the distribution of LTS to a quadratic form to determine the uncertainty ellipse, the major and minor
 277 axes and orientation. We also define a measure, the localization quality (LQ), of how well the actual
 278 LTS distribution matches this expectation by reporting the sum of the squares of the deviations of
 279 eight points evaluated from the fit at a circle of radius corresponding to twice the geometric mean of
 280 the two Gaussian sigmas.

281 We flagged apparently significant sources that do not have good localization fits ($LQ > 8$) with Flag
 282 9 (§ 3.7.3) and for them estimated the position and uncertainty by performing a moment analysis of
 283 the LTS function instead of fitting a quadratic form. Some sources that did not have a well-defined
 284 peak in the likelihood were discarded by hand, on the consideration that they were most likely related
 285 to residual diffuse emission. Another possibility is that two adjacent sources produce a dumbbell-like
 286 shape; for a few of these cases we added a new source by hand.

287 As in 3FGL, we checked the brightest sources spatially associated with likely multiwavelength
 288 counterparts, comparing their localizations with the well-measured positions of the counterparts. The

289 smaller statistical source localization errors in 4FGL allowed us to estimate the absolute precision Δ_{abs}
 290 (at the 95% confidence level) more accurately to $\sim 0^{\circ}.0075$, up from $\sim 0^{\circ}.005$ in 3FGL. The systematic
 291 factor f_{rel} was the same 1.05 as in 3FGL. Eq. 1 shows how the statistical errors Δ_{stat} are transformed
 292 into total errors Δ_{tot} :

$$\Delta_{\text{tot}}^2 = (f_{\text{rel}} \Delta_{\text{stat}})^2 + \Delta_{\text{abs}}^2 \quad (1)$$

293 applies to the two ellipse axes separately.

294 3.2. Significance and Thresholding

295 The framework for this stage of the analysis is inherited from the 3FGL catalog. It splits the
 296 sky into RoIs, varying typically half a dozen sources near the center of the RoI at the same time.
 297 There are 1748 RoIs for 4FGL, listed in the ROIs extension of the catalog (Appendix A). The global
 298 best fit is reached iteratively, injecting the spectra of sources in the outer parts of the RoI from the
 299 previous step or iteration. In this approach the diffuse emission model (§ 2.4) is taken from the global
 300 templates (including the spectrum, unlike what is done with *pointlike* in § 3.1) but it is modulated
 301 in each RoI by three parameters: normalization (at 1 GeV) and small corrective slope of the Galactic
 302 component and normalization of the isotropic component.

303 Among more than 8,000 seeds coming from the localization stage, we keep only sources with $TS >$
 304 25, corresponding to a significance of just over 4σ evaluated from the χ^2 distribution with 4 degrees
 305 of freedom (position and spectral parameters of a power-law source, [Mattox et al. 1996](#)). The model
 306 for the current RoI is readjusted after removing each seed below threshold, so that the final model fits
 307 the full data. The low-energy flux of the seeds below threshold (a fraction of which are real sources)
 308 can be absorbed by neighboring sources closer than the PSF radius.

309 As in 3FGL we manually added known LAT pulsars that could not be localized by the automatic
 310 procedure without phase selection. However none of those reached $TS > 25$ in 4FGL.

311 We introduced a number of improvements with respect to 3FGL (by decreasing order of
 312 importance):

- 313 1. In 3FGL we had already noted that systematic errors due to an imperfect modeling of diffuse
 314 emission were larger than statistical errors in the Galactic plane, and at the same level over
 315 the entire sky. With twice as much exposure and an improved effective area at low energy
 316 with Pass 8, the effect now dominates. The approach adopted in 3FGL (comparing runs
 317 with different diffuse models) allowed characterizing the effect globally and flagging the worst
 318 offenders, but left purely statistical errors on source parameters. In 4FGL we introduce weights
 319 in the maximum likelihood approach (Appendix B). This allows obtaining directly (although in
 320 an approximate way) smaller TS and larger parameter errors, reflecting the level of systematic
 321 uncertainties. We estimated the relative spatial and spectral residuals in the Galactic plane
 322 where the diffuse emission is strongest. The resulting systematic level $\epsilon \sim 3\%$ was used to
 323 compute the weights. This is by far the most important improvement, which avoids reporting
 324 many dubious soft sources.
- 325 2. The automatic iteration procedure at the next-to-last step of the process was improved. There
 326 are now two iteration levels. In a standard iteration the sources and source models are fixed
 327 and only the parameters are free. An RoI and all its neighbors are run again until $\log \mathcal{L}$ does
 328 not change by more than 10 from the previous iteration. Around that we introduce another

iteration level (superiterations). At the first iteration of a given superiteration we reenter all seeds and remove (one by one) those with $TS < 16$. We also systematically check a curved spectral shape vs a power law fit to each source at this first iteration, and keep the curved spectral shape if the fit is significantly better (§ 3.3). At the end of a superiteration an RoI (and its neighbors) enters the next superiteration until $\log \mathcal{L}$ does not change by more than 10 from the last iteration of the previous superiteration. This procedure stabilizes the spectral shapes, particularly in the Galactic plane. Seven superiterations were required to reach full convergence.

3. The fits are now performed from 50 MeV to 1 TeV, and the overall significances (`Signif_Avg`) as well as the spectral parameters refer to the full band. The total energy flux, on the other hand, is still reported between 100 MeV and 100 GeV. For hard sources with photon index less than 2 integrating up to 1 TeV would result in much larger uncertainties. The same is true for soft sources with photon index larger than 2.5 when integrating down to 50 MeV.
4. We considered the effect of energy dispersion in the approximate way implemented in the Science Tools. The effect of energy dispersion is calculated globally for each source, and applied to the whole 3D model of that source, rather than accounting for energy dispersion separately in each pixel. This approximate rescaling captures the main effect at a very minor computational cost. The effect of energy dispersion on the spectra is relatively small. It tends to increase the energy flux (by 4% on average), to reduce the width of the power-law index distribution (by making hard sources softer and soft sources harder, but changing the index by less than 0.02), and to make spectra more curved (because energy dispersion acts as a convolution) but increasing β by only 0.01 on average. In evaluating the likelihood function the effects of energy dispersion were not applied to the isotropic background and the Sun/Moon components whose spectra were obtained from the data without considering energy dispersion.
5. We used smaller RoIs at higher energy because we are interested in the core region only, which contains the sources whose parameters come from that RoI (sources in the outer parts of the RoI are entered only as background). The core region is the same for all energy intervals, and the RoI is obtained by adding a ring to that core region, whose width adapts to the PSF and therefore decreases with energy (Table 2). This does not affect the result because the outer parts of the RoI would not have been correlated to the inner sources at high energy anyway, but saves memory and CPU time.
6. At the last step of the fitting procedure we tested all spectral shapes described in § 3.3 (including log-normal for pulsars and cutoff power law for other sources), readjusting the parameters (but not the spectral shapes) of neighboring sources.

We used only binned likelihood analysis in 4FGL because unbinned mode is much more CPU intensive, and does not support weights or energy dispersion. We split the data into fifteen components, selected according to PSF event type and described in Table 2. As explained in § 2.4.4 at low energy we kept only the event types with the best PSF. Each event type selection has its own isotropic diffuse template (because it includes residual charged-particle background, which depends on event type). A single component is used above 10 GeV in order to save memory and CPU time:

at high energy the background under the PSF is small, so keeping the event types separate does not improve significance very much; it would help for localization, but this is done separately (§ 3.1.2).

A known inconsistency in acceptance exists between Pass 8 PSF event types. It is easy to see on bright sources or the entire RoI spectrum and peaks at the level of 10% between PSF0 (positive residuals, underestimated effective area) and PSF3 (negative residuals, overestimated effective area) at a few GeV. In that range all event types were considered so the effect on source spectra should be minor. Below 1 GeV the PSF0 event type was discarded so the inconsistency could introduce a downward bias (appearing as slightly too hard spectra) but the discrepancy is lower at low energy. The bias on power-law index is estimated to be ~ -0.01 .

3.3. Spectral Shapes

The spectral representation of sources largely follows what was done in 3FGL, considering three spectral models (power law, power law with subexponential cutoff, and log-normal). We changed two important things in the way we parametrize the cutoff power law:

- The cutoff energy was replaced by an exponential factor (a in Eq. 3) which is allowed to be positive. This makes the simple power law a special case of the cutoff power law and allows fitting that model to all sources.
- We set the exponential index (b in Eq. 3) to $2/3$ (instead of 1) for all pulsars that are too faint for it to be left free. This recognizes the fact that $b < 1$ (subexponential) in all bright pulsars. Among the six brightest pulsars, three have $b \sim 0.55$ and three have $b \sim 0.75$). We chose $2/3$ as a simple intermediate value.

We use three spectral representations in 4FGL. For all of them the normalization (flux density K) is defined at a reference energy E_0 (`Pivot_Energy` in the tables) chosen such that the error on K is minimal.

- a log-normal representation (`LogParabola` in the tables) for all significantly curved spectra except pulsars, 3C 454.3 and the Small Magellanic Cloud (SMC):

$$\frac{dN}{dE} = K \left(\frac{E}{E_0} \right)^{-\alpha - \beta \log(E/E_0)} \quad (2)$$

where \log is the natural logarithm. The parameters K , α (spectral slope at E_0) and the curvature β appear as `LP_Flux_Density`, `LP_Index` and `LP_beta` in the tables, respectively. No significantly negative β (spectrum curved upwards) was found. The maximum allowed β was set to 1 as in 3FGL.

- a subexponentially cutoff power law for all significantly curved pulsars (`PLSuperExpCutoff` in the tables):

$$\frac{dN}{dE} = K \left(\frac{E}{E_0} \right)^{-\Gamma} \exp(a(E_0^b - E^b)) \quad (3)$$

where E_0 and E in the exponential are expressed in MeV. The parameters K , Γ (low-energy spectral slope), a (exponential factor in MeV^{-b}) and b (exponential index) appear as `PLEC_Flux_Density`, `PLEC_Index`, `PLEC_Expfactor` and `PLEC_Exp_Index` in the tables,

respectively. Note that in the Science Tools that spectral shape is called `PLSuperExpCutoff2` and no E_0^b term appears in the exponential, so the error on K in the tables was obtained from the covariance matrix. The minimum Γ was set to 0 (in 3FGL it was set to 0.5, but a smaller b results in a smaller Γ). No significantly negative a (spectrum curved upwards) was found.

- a simple power-law form (Eq. 3 without the exponential term) for all sources not significantly curved. For those parameters K and Γ appear as `PL_Flux_Density` and `PL_Index` in the tables.

A source is considered significantly curved if $TS_{\text{curv}} > 9$ (3σ significance) where $TS_{\text{curv}} = 2 \log(\mathcal{L}(\text{curved spectrum})/\mathcal{L}(\text{power-law}))$. When this is achieved the global model (used to fit neighboring sources) uses the curved representation. We used a lower TS_{curv} threshold than in 3FGL (where it was 16, or 4σ) for two reasons. First, all bright sources are actually significantly curved downwards so there is no good reason to penalize the curved models too much. Second, the power-law model tends to exceed the data at both ends of the spectrum, where constraints are weak. It is not a worry at high energy, but at low energy the collection of faint sources modeled as power laws generates an effectively diffuse excess in the model, which will make the curved sources more curved than they should be. Using a `LogParabola` spectral shape for all sources would be even better physically, but the very large correlation between sources at low energy due to the broad PSF makes that unstable. The curvature significance is reported as `LP_SigCurv` or `PLEC_SigCurv`, replacing the former unique `Signif_Curve` column of 3FGL. Both values were derived from TS_{curv} and corrected for systematic uncertainties on the effective area following Eq. 3 of 3FGL. As a result, 52 `LogParabola` sources (with $TS_{\text{curv}} > 9$) have `LP_SigCurv` less than 3.

Sources with curved spectra are considered significant whenever $TS > 25 + 9 = 34$. This is conservative enough, and accepts a few more strongly curved faint sources (pulsar-like) than the 3FGL criterion which requested $TS > 25$ in the power-law representation.

One more pulsar (PSR J1057–5226) was fit with a free exponential index, besides the six sources modeled in this way in 3FGL. The Crab was modeled with three spectral components as in 3FGL, but the inverse Compton emission of the nebula was represented as a log-normal law instead of a simple power law. The parameters of that component were fixed to $\alpha = 1.75$, $\beta = 0.08$, $K = 5.5 \times 10^{-13}$ ph/cm²/MeV/s at 10 GeV, mimicking the broken power-law fit by Buehler et al. (2012). They were unstable (too much correlation with the pulsar) without phase selection. Four other sources had fixed parameters in 3FGL. These were freed in 4FGL.

Overall in 4FGL seven sources (the six brightest pulsars and 3C 454.3) were fit as `PLSuperExpCutoff` with free b (Eq. 3), 215 pulsars were fit as `PLSuperExpCutoff` with $b = 2/3$, the SMC was fit as `PLSuperExpCutoff` with $b = 1$, 1332 sources were fit as `LogParabola` (including the fixed inverse Compton component of the Crab and 38 other extended sources) and the rest were represented as power laws. The larger fraction of curved spectra compared to 3FGL is due to the lower TS_{curv} threshold.

The way the parameters are reported has changed as well:

- The spectral shape parameters are now explicitly associated to the spectral model they come from. They are reported as `Shape_Param` where `Shape` is one of `PL` (`PowerLaw`), `PLEC` (`PLSuperExpCutoff`) or `LP` (`LogParabola`) and `Param` is the parameter name. Columns `Shape_Index` replace `Spectral_Index` which was ambiguous.

- All sources were fit with the three spectral shapes, so all fields are filled. The curvature significance is calculated twice by comparing power law with both log-normal and exponentially cutoff power law (although only one is actually used to switch to the curved shape in the global model, depending on whether the source is a pulsar or not). There are also three `Shape_Flux_Density` columns referring to the same `Pivot_Energy`.

This representation allows comparing unassociated sources with either pulsars or blazars using the same spectral shape. The preferred spectral shape (reported as `SpectrumType`) remains what is used in the global model, when the source is part of the background (i.e., when fitting the other sources). It is also what is used to derive the fluxes, their uncertainties and the significance.

3.4. Extended Sources

As for the 3FGL catalog, we explicitly model as spatially extended those LAT sources that have been shown in dedicated analyses to be resolved by the LAT. The catalog process does not involve looking for new extended sources, testing possible extension of sources detected as point-like, nor refitting the spatial shapes of known extended sources.

Most templates are geometrical, so they are not perfect matches to the data and the source detection often finds residuals on top of extended sources, which are then converted into additional point sources. As in 3FGL those additional point sources were voluntarily deleted from the model, except if they met two of the following criteria: associated, much harder than the extended source (`Pivot_Energy` larger by a factor e or more), or very significant ($TS > 100$). Contrary to 3FGL, that procedure was applied inside the Cygnus X cocoon as well.

The latest pre-4FGL compilation is the 55 extended sources entered in 3FHL, which includes the result of the systematic search for new sources in the Galactic plane ($|b| < 7^\circ$) above 10 GeV (FGES, Ackermann et al. 2017). Two of those were not propagated to 4FGL:

- FGES J1800.5–2343 was replaced by the W 28 template from 3FGL, and the nearby excesses (Hanabata et al. 2014) were left to be modeled as point sources.
- FGES J0537.6+2751 was replaced by the radio template of S 147 used in 3FGL, which fits better than the disk used in the FGES paper (S 147 is a soft source, so it was barely detected above 10 GeV).

MSH 15-56 was replaced by two morphologically distinct components, following Devin et al. (2018): one for the SNR (SNR mask in the paper), the other one for the PWN inside it (radio template). We added back the W 30 SNR on top of FGES J1804.7–2144 (coincident with HESS J1804–216). The two overlap but the best localization clearly moves with energy from W 30 to HESS J1804–216.

Eighteen sources were added, resulting in 75 extended sources in 4FGL:

- The Rosette nebula and Monoceros SNR (too soft to be detected above 10 GeV) were characterized by Katagiri et al. (2016b). We used the same templates.
- The systematic search for extended sources outside the Galactic plane above 1 GeV (FHES, Ackermann et al. 2018) found sixteen reliable extended sources. Five of them were already known as extended sources. We ignored two others: M 31 (extension only marginally significant) and SNR G119.5+10.2 around PSR J0007+7303 (not significant without phase gating). We introduced the nine remaining FHES sources (including the Crab nebula and the ρ Oph

molecular cloud). One of them (J1741.6-3917) was reported by Araya (2018a) as well, with similar extension.

- Four HESS sources were found to be extended sources in the *Fermi* range as well: J1534-571 (Araya 2017), J1808-204 (Yeung et al. 2016), J1809-193 and J1813-178 (Araya 2018b).
- Three extended sources were discovered in the search for GeV emission from magnetars (Li et al. 2017a). They contain SNRs (Kes 73, Kes 79 and G42.8+0.6 respectively) but are much bigger than the radio SNRs. One of them (around Kes 73) was also noted by Yeung et al. (2017).

Table 4 lists the source name, origin, spatial template and the reference for the dedicated analysis. These sources are tabulated with the point sources, with the only distinction being that no position uncertainties are reported and their names end in e (see Appendix A). Unidentified point sources inside extended ones are indicated as “xxx field” in the ASSOC2 column of the catalog.

Table 4. Extended Sources Modeled in the 4FGL Analysis

4FGL Name	Extended Source	Origin	Spatial Form	Extent [deg]	Reference
J0058.0–7245e	SMC Galaxy	Updated	Map	1.5	Caputo et al. (2016)
J0221.4+6241e	HB 3	New	Disk	0.8	Katagiri et al. (2016a)
J0222.4+6156e	W 3	New	Map	0.6	Katagiri et al. (2016a)
J0322.6–3712e	Fornax A	3FHL	Map	0.35	Ackermann et al. (2016c)
J0427.2+5533e	SNR G150.3+4.5	3FHL	Disk	1.515	Ackermann et al. (2017)
J0500.3+4639e	HB 9	New	Map	1.0	Araya (2014)
J0500.9–6945e	LMC FarWest	3FHL	Map ^a	0.9	Ackermann et al. (2016d)
J0519.9–6845e	LMC Galaxy	New	Map ^a	3.0	Ackermann et al. (2016d)
J0530.0–6900e	LMC 30DorWest	3FHL	Map ^a	0.9	Ackermann et al. (2016d)
J0531.8–6639e	LMC North	3FHL	Map ^a	0.6	Ackermann et al. (2016d)
J0534.5+2201e	Crab nebula IC	New	Gaussian	0.03	Ackermann et al. (2018)
J0540.3+2756e	S 147	3FGL	Disk	1.5	Katsuta et al. (2012)
J0617.2+2234e	IC 443	2FGL	Gaussian	0.27	Abdo et al. (2010b)
J0634.2+0436e	Rosette	New	Map	(1.5, 0.875)	Katagiri et al. (2016b)
J0639.4+0655e	Monoceros	New	Gaussian	3.47	Katagiri et al. (2016b)
J0822.1–4253e	Puppis A	3FHL	Disk	0.443	Ackermann et al. (2017)
J0833.1–4511e	Vela X	2FGL	Disk	0.91	Abdo et al. (2010c)
J0851.9–4620e	Vela Junior	3FHL	Disk	0.978	Ackermann et al. (2017)
J1023.3–5747e	Westerlund 2	3FHL	Disk	0.278	Ackermann et al. (2017)
J1036.3–5833e	FGES J1036.3–5833	3FHL	Disk	2.465	Ackermann et al. (2017)
J1109.4–6115e	FGES J1109.4–6115	3FHL	Disk	1.267	Ackermann et al. (2017)
J1208.5–5243e	SNR G296.5+10.0	3FHL	Disk	0.76	Ajero et al. (2016b)
J1213.3–6240e	FGES J1213.3–6240	3FHL	Disk	0.332	Ackermann et al. (2017)
J1303.0–6312e	HESS J1303–631	3FGL	Gaussian	0.24	Aharonian et al. (2005)
J1324.0–4330e	Centaurus A (lobes)	2FGL	Map	(2.5, 1.0)	Abdo et al. (2010d)
J1355.1–6420e	HESS J1356–645	3FHL	Disk	0.405	Ackermann et al. (2017)
J1409.1–6121e	FGES J1409.1–6121	3FHL	Disk	0.733	Ackermann et al. (2017)
J1420.3–6046e	HESS J1420–607	3FHL	Disk	0.123	Ackermann et al. (2017)
J1443.0–6227e	RCW 86	3FHL	Map	0.3	Ajello et al. (2016)
J1501.0–6310e	FHES J1501.0–6310	New	Gaussian	1.29	Ackermann et al. (2018)

Table 4 continued on next page

Table 4 (continued)

4FGL Name	Extended Source	Origin	Spatial Form	Extent [deg]	Reference
J1507.9–6228e	HESS J1507–622	3FHL	Disk	0.362	Ackermann et al. (2017)
J1514.2–5909e	MSH 15–52	3FHL	Disk	0.243	Ackermann et al. (2017)
J1533.9–5712e	HESS J1534–571	New	Disk	0.4	Araya (2017)
J1552.4–5612e	MSH 15–56 PWN	New	Map	0.08	Devin et al. (2018)
J1552.9–5607e	MSH 15–56 SNR	New	Map	0.3	Devin et al. (2018)
J1553.8–5325e	FGES J1553.8–5325	3FHL	Disk	0.523	Ackermann et al. (2017)
J1615.3–5146e	HESS J1614–518	3FGL	Disk	0.42	Lande et al. (2012)
J1616.2–5054e	HESS J1616–508	3FGL	Disk	0.32	Lande et al. (2012)
J1626.9–2431e	FHES J1626.9–2431	New	Gaussian	0.29	Ackermann et al. (2018)
J1631.6–4756e	FGES J1631.6–4756	3FHL	Disk	0.256	Ackermann et al. (2017)
J1633.0–4746e	FGES J1633.0–4746	3FHL	Disk	0.61	Ackermann et al. (2017)
J1636.3–4731e	SNR G337.0–0.1	3FHL	Disk	0.139	Ackermann et al. (2017)
J1642.1–5428e	FHES J1642.1–5428	New	Disk	0.696	Ackermann et al. (2018)
J1652.2–4633e	FGES J1652.2–4633	3FHL	Disk	0.718	Ackermann et al. (2017)
J1655.5–4737e	FGES J1655.5–4737	3FHL	Disk	0.334	Ackermann et al. (2017)
J1713.5–3945e	RX J1713.7–3946	3FHL	Map	0.56	H. E. S. S. Collaboration et al. (2018a)
J1723.5–0501e	FHES J1723.5–0501	New	Gaussian	0.73	Ackermann et al. (2018)
J1741.6–3917e	FHES J1741.6–3917	New	Disk	1.65	Ackermann et al. (2018)
J1745.8–3028e	FGES J1745.8–3028	3FHL	Disk	0.528	Ackermann et al. (2017)
J1801.3–2326e	W 28	2FGL	Disk	0.39	Abdo et al. (2010e)
J1804.7–2144e	HESS J1804–216	3FHL	Disk	0.378	Ackermann et al. (2017)
J1805.6–2136e	W 30	2FGL	Disk	0.37	Ajello et al. (2012)
J1808.2–2028e	HESS J1808–204	New	Disk	0.65	Yeung et al. (2016)
J1810.3–1925e	HESS J1809–193	New	Disk	0.5	Araya (2018b)
J1813.1–1737e	HESS J1813–178	New	Disk	0.6	Araya (2018b)
J1824.5–1351e	HESS J1825–137	2FGL	Gaussian	0.75	Grondin et al. (2011)
J1834.1–0706e	SNR G24.7+0.6	3FHL	Disk	0.214	Ackermann et al. (2017)
J1834.5–0846e	W 41	3FHL	Gaussian	0.23	Abramowski et al. (2015)
J1836.5–0651e	FGES J1836.5–0651	3FHL	Disk	0.535	Ackermann et al. (2017)
J1838.9–0704e	FGES J1838.9–0704	3FHL	Disk	0.523	Ackermann et al. (2017)
J1840.8–0453e	Kes 73	New	Disk	0.32	Li et al. (2017a)
J1840.9–0532e	HESS J1841–055	3FGL	2D Gaussian	(0.62, 0.38)	Aharonian et al. (2008)
J1852.4+0037e	Kes 79	New	Disk	0.63	Li et al. (2017a)
J1855.9+0121e	W 44	2FGL	2D Ring	(0.30, 0.19)	Abdo et al. (2010f)
J1857.7+0246e	HESS J1857+026	3FHL	Disk	0.613	Ackermann et al. (2017)
J1908.6+0915e	SNR G42.8+0.6	New	Disk	0.6	Li et al. (2017a)
J1923.2+1408e	W 51C	2FGL	2D Disk	(0.375, 0.26)	Abdo et al. (2009b)
J2021.0+4031e	γ -Cygni	3FGL	Disk	0.63	Lande et al. (2012)
J2028.6+4110e	Cygnus X cocoon	3FGL	Gaussian	3.0	Ackermann et al. (2011a)
J2045.2+5026e	HB 21	3FGL	Disk	1.19	Pivato et al. (2013)
J2051.0+3040e	Cygnus Loop	2FGL	Ring	1.65	Katagiri et al. (2011)
J2129.9+5833e	FHES J2129.9+5833	New	Gaussian	1.09	Ackermann et al. (2018)
J2208.4+6443e	FHES J2208.4+6443	New	Gaussian	0.93	Ackermann et al. (2018)
J2301.9+5855e	CTB 109	3FHL	Disk	0.249	Ackermann et al. (2017)
J2304.0+5406e	FHES J2304.0+5406	New	Gaussian	1.58	Ackermann et al. (2018)

Table 4 continued on next page

Table 4 (*continued*)

4FGL Name	Extended Source	Origin	Spatial Form	Extent [deg]	Reference
-----------	-----------------	--------	--------------	--------------	-----------

^aEmissivity model.

NOTE— List of all sources that have been modeled as spatially extended. The Origin column gives the name of the *Fermi*-LAT catalog in which that spatial template was introduced. The Extent column indicates the radius for Disk (flat disk) sources, the 68% containment radius for Gaussian sources, the outer radius for Ring (flat annulus) sources, and an approximate radius for Map (external template) sources. The 2D shapes are elliptical; each pair of parameters (*a*, *b*) represents the semi-major (*a*) and semi-minor (*b*) axes.

3.5. Flux Determination

Thanks to the improved statistics, the source photon fluxes in 4FGL are reported in seven energy bands (1: 50 to 100 MeV; 2: 100 to 300 MeV; 3: 300 MeV to 1 GeV; 4: 1 to 3 GeV; 5: 3 to 10 GeV; 6: 10 to 30 GeV; 7: 30 to 300 GeV) extending both below and above the range (100 MeV to 100 GeV) covered in 3FGL. Up to 10 GeV, the data files were exactly the same as in the global fit (Table 2). In order to get the best sensitivity between 10 and 30 GeV, we split the data into 4 components per event type, using pixel size 0°:04 for PSF3, 0°:05 for PSF2, 0°:1 for PSF1 and 0°:2 for PSF0. In band 7 we used unbinned likelihood, which is as precise while using much smaller files. It does not allow correcting for energy dispersion, but this is not an important issue in that band. The fluxes were obtained by freezing the spectral index to that obtained in the fit over the full range and adjusting the normalization in each spectral band. For the curved spectra (§ 3.3) the spectral index in a band was set to the local spectral slope at the logarithmic mid-point of the band $\sqrt{E_n E_{n+1}}$, restricted to be in the interval [0,5].

In each band, the analysis was conducted in the same way as for the 3FGL catalog. In order to adapt more easily to new band definitions, the results (fluxes and uncertainties, νF_ν and significances) are reported in a set of four vector columns (Table 9: Flux_Band, Unc_Flux_Band, nuFnu, Sqrt_TS_Band) instead of a set of four columns per band as in previous FGL catalogs.

The spectral fit quality is computed in a more precise way than in 3FGL from twice the sum of log-likelihood differences, as we did for the variability index (Sect. 3.6 of the 2FGL paper). The contribution from each band S_i^2 also accounts for systematic uncertainties on effective area via

$$S_i^2 = \frac{2\sigma_i^2}{\sigma_i^2 + (f_i^{\text{rel}} F_i^{\text{fit}})^2} [\log \mathcal{L}_i(F_i^{\text{best}}) - \log \mathcal{L}_i(F_i^{\text{fit}})] \quad (4)$$

where *i* runs over all bands, F_i^{fit} is the flux predicted by the global model, F_i^{best} is the flux fitted to band *i* alone, σ_i is the statistical error (upper error if $F_i^{\text{best}} \leq F_i^{\text{fit}}$, lower error if $F_i^{\text{best}} > F_i^{\text{fit}}$) and the spectral fit quality is simply $\sum_i S_i^2$. The systematic uncertainties⁷ f_i^{rel} are set to 0.15 in the first band, 0.1 in the second and the last bands, and 0.05 in bands 3 to 6. The uncertainty is larger in the first band because only PSF3 events are used.

Too large values of spectral fit quality are flagged (Flag 10 in Table 5). Since there are 7 bands and (for most sources, which are fit with the power-law model) 2 free parameters, the flag is set when $\sum_i S_i^2 > 20.5$ (probability 10^{-3} for a χ^2 distribution with 5 degrees of freedom). Only 6 sources trigger this. We also set the same flag whenever any individual band is off by more than 3σ ($S_i^2 > 9$). This occurs in 26 sources. Among the 27 sources flagged with Flag 10 (examples in Figure 2), the

⁷ See https://fermi.gsfc.nasa.gov/ssc/data/analysis/LAT_caveats.html.

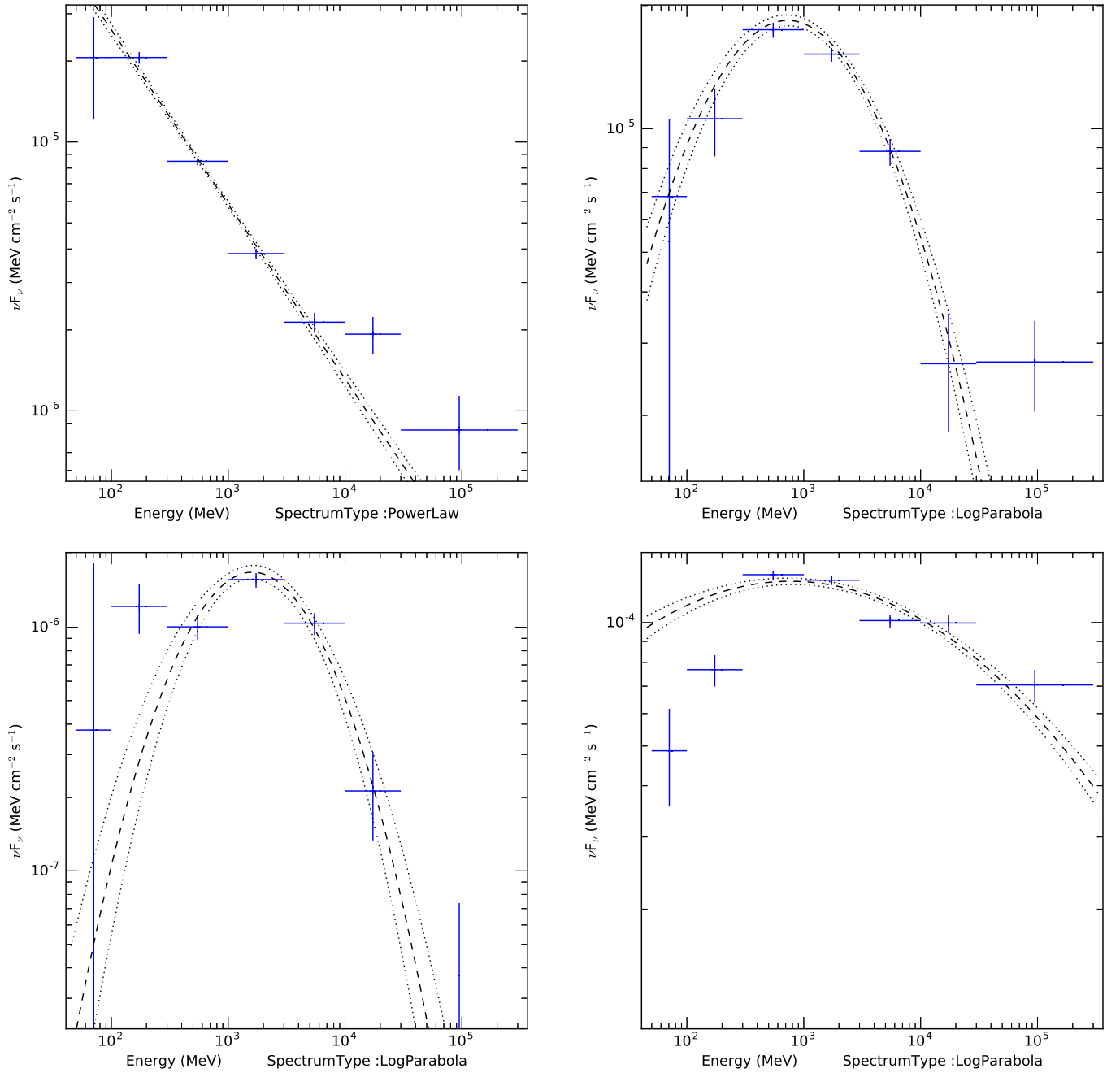


Figure 2. Spectral energy distribution of four sources flagged with bad spectral fit quality (Flag 10 in Table 5). On all plots the dashed line is the best fit from the analysis over the full energy range, and the dotted lines show the uncertainty obtained from the covariance matrix on the spectral parameters. The vertical scale is not the same in all plots. Top left, the Cen A radio galaxy (4FGL J1325.5–4300) fit by a power law with $\Gamma = 2.65$: it is a good representation up to 10 GeV, but the last two points deviate from the power-law fit. Top right, the Large Magellanic Cloud (4FGL J0519.9–6845e): the fitted LogParabola spectrum appears to drop too fast at high energy. Bottom left, the unassociated source 4FGL J0336.0+7502: the low-energy points deviate from the LogParabola fit. Bottom right, the Cygnus X cocoon (4FGL J2028.6+4110e): the first two points deviate from the LogParabola fit in a way that is probably not real.

527 Vela pulsar and Geminga are very bright sources for which our spectral representation is not good
 528 enough. A few show signs of a real second component in the spectrum, such as Cen A (H. E. S. S.
 529 Collaboration et al. 2018b). Several would be better fit by a different spectral model: the LMC
 530 probably decreases at high energy as a power law like our own Galaxy, 4FGL J0336.0+7502 is better
 531 fit by a PLSuperExpCutoff model. This unassociated source at 15° latitude is strongly curved and
 532 non-variable: it is a good milli-second pulsar candidate. Other sources show deviations at low energy
 533 and are in confused regions or close to a brighter neighbor, such as the Cygnus X cocoon. This
 534 extended source contains many point sources inside it and the PSF below 300 MeV is too broad to
 535 provide a reliable separation.

536 The fluxes in the 50 to 100 MeV band are very hard to estimate, because of the enormous confusion.
 537 The average distance between sources (1.7°) is about equal to the half width at half maximum of PSF3
 538 events in that band, so it is nearly always possible to set a source to 0 and compensate by a suitable
 539 combination of flux adjustments in its neighbors. This is why only 34 sources have $TS > 25$ in that
 540 band (all are bright sources with global $TS > 700$). This is much less than the 198 low-energy sources
 541 reported by Principe et al. (2018, 1FLE). The reason is that in 4FGL we consider that all sources in
 542 the catalog can have low-energy emission, so the total source flux is distributed over 5000 sources,
 543 whereas 1FLE focussed on finding individual peaks.

544 At the other extreme, 618 sources have $TS > 25$ in the 30 to 300 GeV band, which is entirely
 545 limited by photon counting ($TS > 25$ in that band corresponds to about 5 events). Only 13 of those
 546 are not associated to a 3FHL or FHES source. The brightest of them (at $TS = 54$ in that band) is
 547 a hard source associated with 1RXS J224123.5+294244, mostly significant in the last year, after the
 548 3FHL time range.

549 As in past FGL catalogs, the photon fluxes between 1 and 100 GeV as well as the energy fluxes
 550 between 100 MeV and 100 GeV were derived from the full-band analysis assuming the best spectral
 551 shape, and their uncertainties come from the covariance matrix. Even though the full analysis is
 552 carried out down to 50 MeV and up to 1 TeV in 4FGL, we have not changed the energy range over
 553 which we quote fluxes so that they can be easily compared with fluxes in past catalogs. The photon
 554 fluxes above 100 GeV are negligible except in the very hardest power-law sources, and the energy
 555 fluxes below 100 MeV and above 100 GeV are not precisely measured (even for soft and hard sources,
 556 respectively).

557

3.6. Variability

558 For this intermediate 4FGL version, the light curves were computed over 1-year intervals. This
 559 is much faster and more stable than fitting smaller time intervals, and provides a good variability
 560 assessment already. We used binned likelihood and the same data as in the main run up to 10 GeV
 561 (Table 2), but in order to save disk space and CPU time we merged event types together. Above
 562 10 GeV we used unbinned likelihood (more efficient when there are few events). We ignored events
 563 above 100 GeV (unimportant for variability).

564 As in 3FGL the fluxes in each interval were obtained by freezing the spectral parameters to those
 565 obtained in the fit over the full range and adjusting the normalization. As in previous FGL catalogs,
 566 the fluxes in each interval are reported as photon fluxes between 0.1 and 100 GeV.

567 The weights appropriate for one year were computed using the procedure explained in Appendix B,
 568 entering the same data cube divided by 8 (we use the same weights in each year), and ignoring the
 569 last steps specific to splitting event types. The weights are of course much larger than those for 8

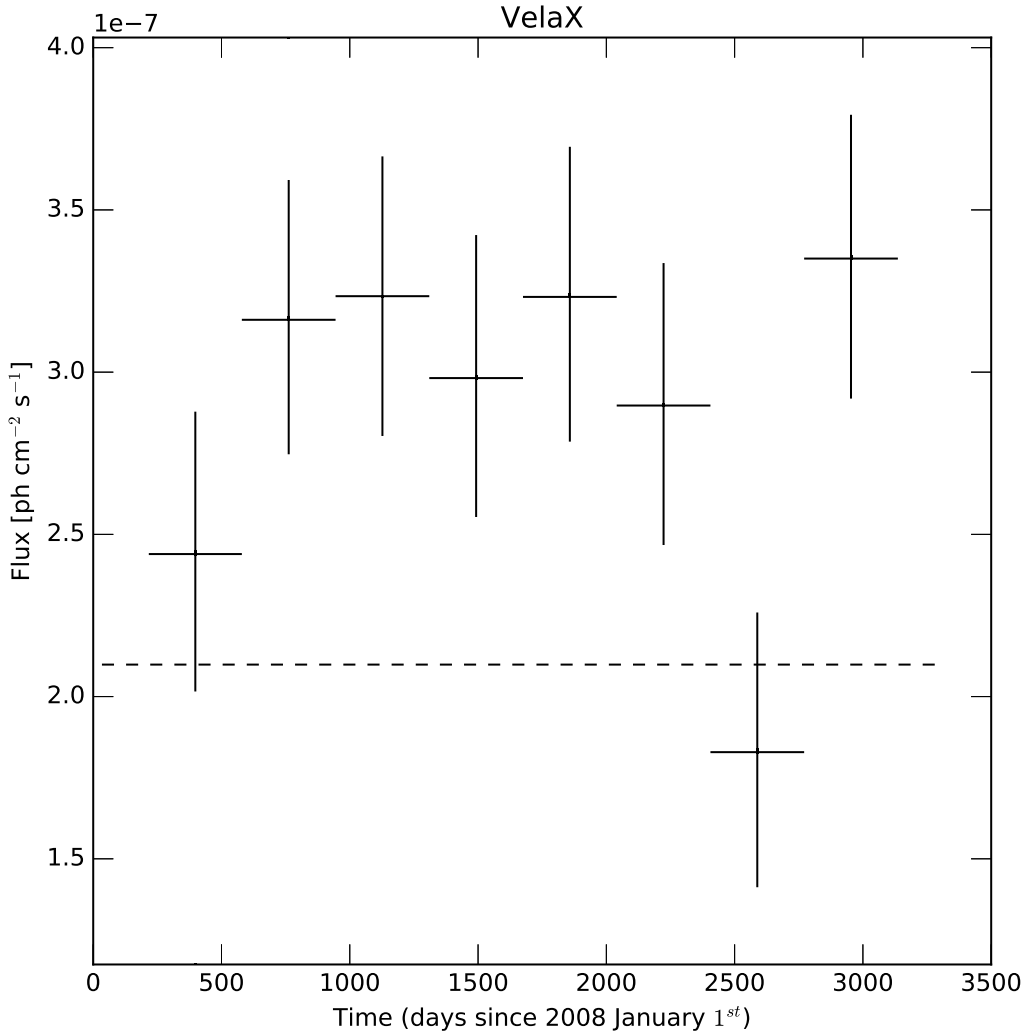


Figure 3. Light curve of Vela X (the flux is given in the 0.1 to 100 GeV band), which is an extended source that should not be variable. Indeed the monthly fluxes are compatible with a constant (the average flux is 2.9×10^{-7} ph cm^{-2} s^{-1}), but not with the flux extracted over the full eight years (dashed line, too low). That inconsistency is due to differences in the data analysis settings between the global fit and the fits per year (the weights in particular). Vela X is very close to the very bright Vela pulsar, so it is strongly attenuated by the weights. For most sources the average flux is much closer to the global flux.

570 years, but remain a significant correction (the weights are less than 0.2 in the Galactic Ridge up to
571 300 MeV).

572 Because of the different weights between the full analysis and that in 1-year intervals, the average
573 flux from the light curve F_{av} can differ somewhat from the flux in the total analysis F_{glob} (low energies
574 are less attenuated in the analysis over 1-year intervals). This is illustrated in Figure 3. In 4FGL we
575 compute the variability index TS_{var} (reported as `Variability_Index` in the FITS file) as

$$TS_{\text{var}} = 2 \sum_i [\log \mathcal{L}_i(F_i) - \log \mathcal{L}_i(F_{\text{glob}})] - \max(\chi^2(F_{\text{glob}}) - \chi^2(F_{\text{av}}), 0) \quad (5)$$

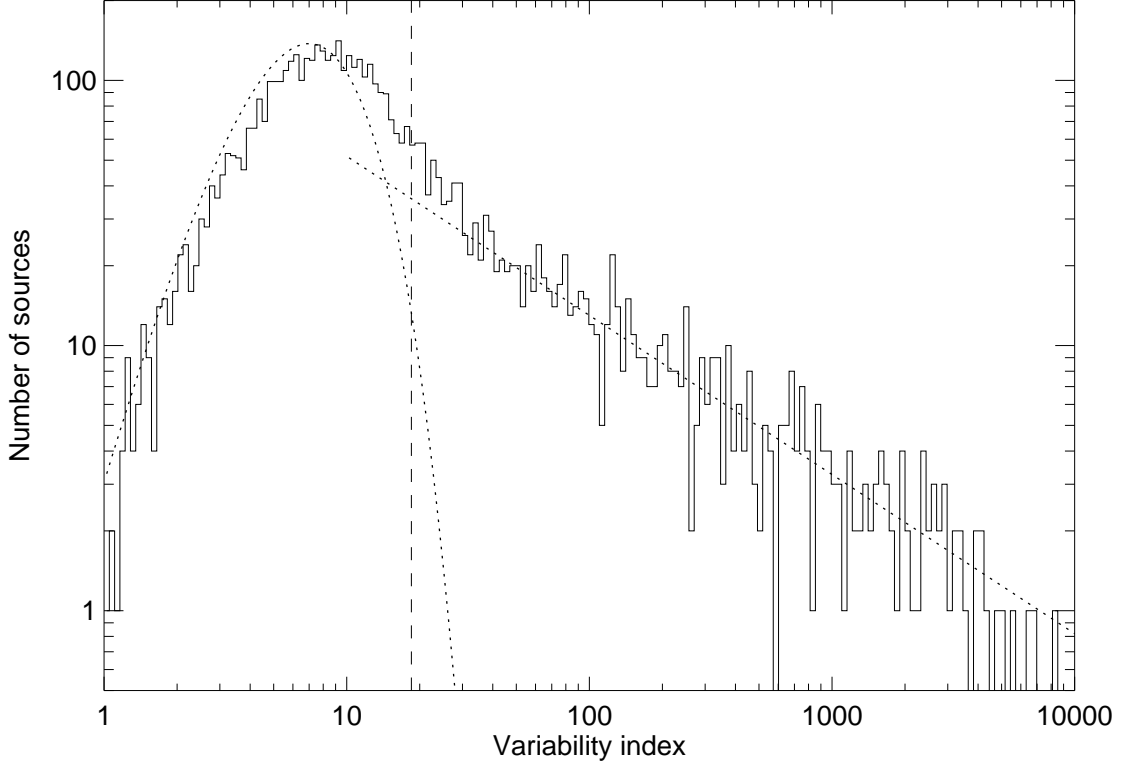


Figure 4. Distribution of the variability index (Eq. 5) with respect to $\log(TS_{\text{var}})$. The dotted line at left is the χ^2 distribution for 7 degrees of freedom, expected for a set of non-variable sources. The dotted line at right is a power-law decreasing as $TS_{\text{var}}^{-0.6}$. The vertical dashed line is the threshold above which we consider that a source is likely variable.

$$\chi^2(F) = \sum_i \frac{(F_i - F)^2}{\sigma_i^2} \quad (6)$$

576 where F_i are the individual flux values, $\mathcal{L}_i(F)$ the likelihood in interval i assuming flux F and σ_i the
 577 errors on F_i (upper error if $F_i \leq F$, lower error if $F_i > F$). The first term in Eq. 5 is the same as
 578 Eq. 4 of 2FGL. The second term corrects (in the Gaussian limit) for the difference between F_{glob} and
 579 F_{av} (since the average flux is known only at the very end, it could not be entered when computing
 580 $\mathcal{L}_i(F)$). We subtract the second term only when it is positive (it is not necessarily positive because
 581 the best χ^2 is reached at the average weighted by σ_i^{-2} , not the straight average). On the other hand,
 582 we did not correct the variability index for the relative systematic error, which is already accounted
 583 for in the weighting procedure.

584 The distribution of observed TS_{var} is shown in Figure 4. It looks like a composite of a power-law
 585 distribution and a $\chi^2(7)$ distribution. The left branch corresponds both to constant sources (such as
 586 most pulsars) and sources too faint to have measurable variability. There are many blazars among
 587 them, which are most likely just as variable as brighter blazars. This contribution of real variability to
 588 TS_{var} is probably the reason why the histogram is a little offset to the right of the $\chi^2(7)$ distribution.
 589 Variability is considered probable when $TS_{\text{var}} > 18.48$, corresponding to 99% confidence in a χ^2
 590 distribution with $N_{\text{int}} - 1 = 7$ degrees of freedom, where N_{int} is the number of intervals. We find

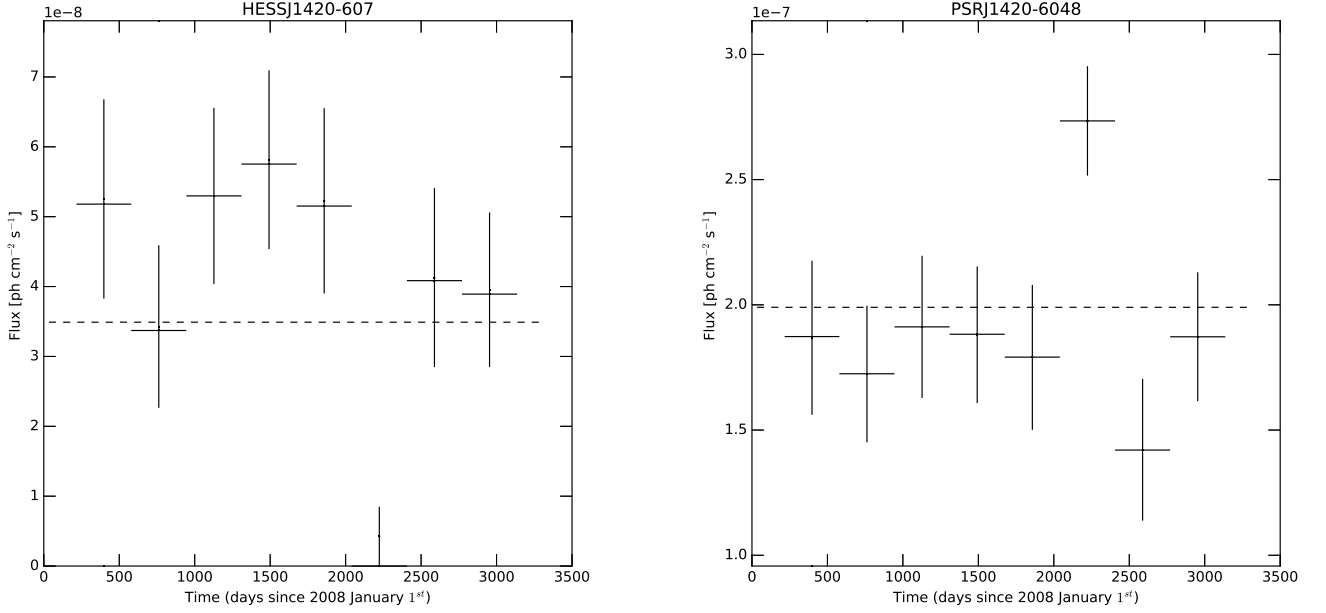


Figure 5. Light curves of the pulsar wind nebula HESS J1420–607 at $TS_{\text{var}} = 23.4$ and its parent pulsar PSR J1420–6048. The apparent variability of HESS J1420–607 is due to the low point in the 6th year, which corresponds to a high point in the light curve of PSR J1420–6048. This is clearly a case of incorrect flux transfer due to the strong spatial confusion (the nebula is only $0^{\circ}.12$ in radius), despite the spectral difference between the two sources. The perturbation of the pulsar (brighter than the nebula) is not enough to exceed the variability threshold.

591 1327 variable sources with that criterion. After the χ^2 -based correction, Vela X remains below that
 592 threshold. One extended source still exceeds the variability threshold. This is HESS J1420–607
 593 (Figure 5), confused with its parent pulsar PSR J1420–6048. A similar flux transfer occurred in the
 594 third year between the Crab pulsar and the Crab Nebula. This one can be understood because the
 595 nebula becomes much harder during flares, while our pipeline assumes the soft power-law fit over the
 596 full interval applies throughout. None of those variabilities are real.

597 Besides the Crab and the known variable pulsars PSR J1227–4853 (Johnson et al. 2015) and PSR
 598 J2021+4026 (Allafort et al. 2013), three other pulsars are above the variability threshold. Two are
 599 just above it and can be chance occurrences (there are more than 200 pulsars, so we expect two above
 600 the 1% threshold). The last one is PSR J2043+2740 (Figure 6), which looks like a real variability
 601 (regular flux decrease by a factor of 3).

602 In 4FGL we report the fractional variability of the sources in the FITS file as `Frac_Variability`.
 603 It is defined for each source from the excess variance on top of the statistical and systematic
 604 fluctuations:

$$Var = \frac{1}{N_{\text{int}} - 1} \sum_i (F_i - F_{\text{av}})^2 \quad (7)$$

$$\delta F = \sqrt{\max\left(Var - \frac{\sum_i \sigma_i^2}{N_{\text{int}}}, 0\right)} \quad (8)$$

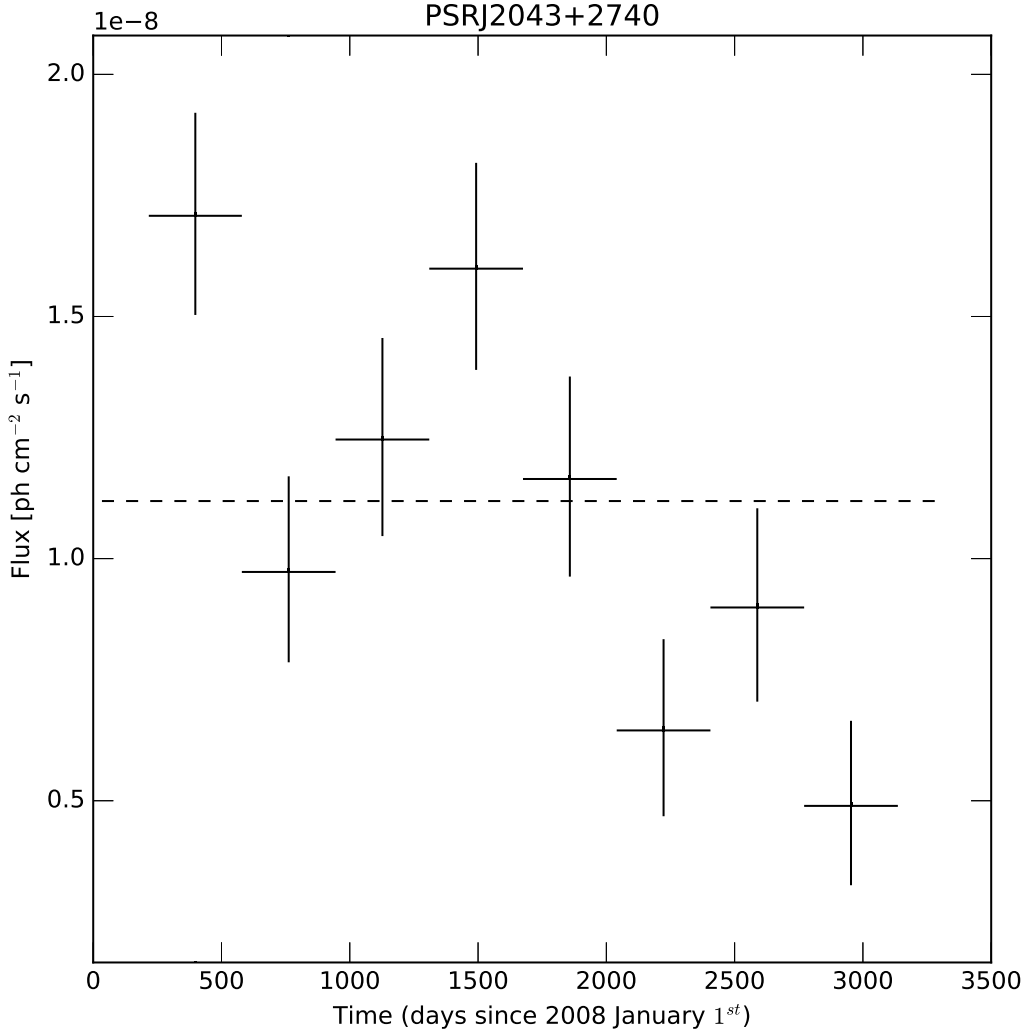


Figure 6. Light curve of the pulsar PSR J2043+2740, at $TS_{\text{var}} = 33$. The flux of this pulsar appears to be decreasing regularly.

$$\frac{\sigma F}{F} = \max \left(\frac{1}{\sqrt{2(N_{\text{int}} - 1)}} \frac{V_i}{F_{\text{av}} \delta F}, 10 \right) \quad (9)$$

605 where the fractional variability itself is simply $\delta F/F_{\text{av}}$. This is similar to Eq. 3 of 1FGL, except we
 606 omit the systematic error term because it is now incorporated in the σ_i^2 via the weights. The error
 607 $\sigma F/F$ is estimated approximately from the expected scatter on the sample variance Var , which is the
 608 dominant source of uncertainty. We cap it to 10 to avoid reporting meaningless high uncertainties.
 609 Figure 7 can be compared to Figure 8 of [Abdo et al. \(2009c\)](#), which was based on 1-week intervals
 610 (and contained many fewer sources, of course). The fractional variability is similar, going up to 1,
 611 indicating that there is no preferred variability time scale in blazars. The criterion we use is not
 612 sensitive to relative variations smaller than 50% at $TS = 100$, so only bright sources can populate

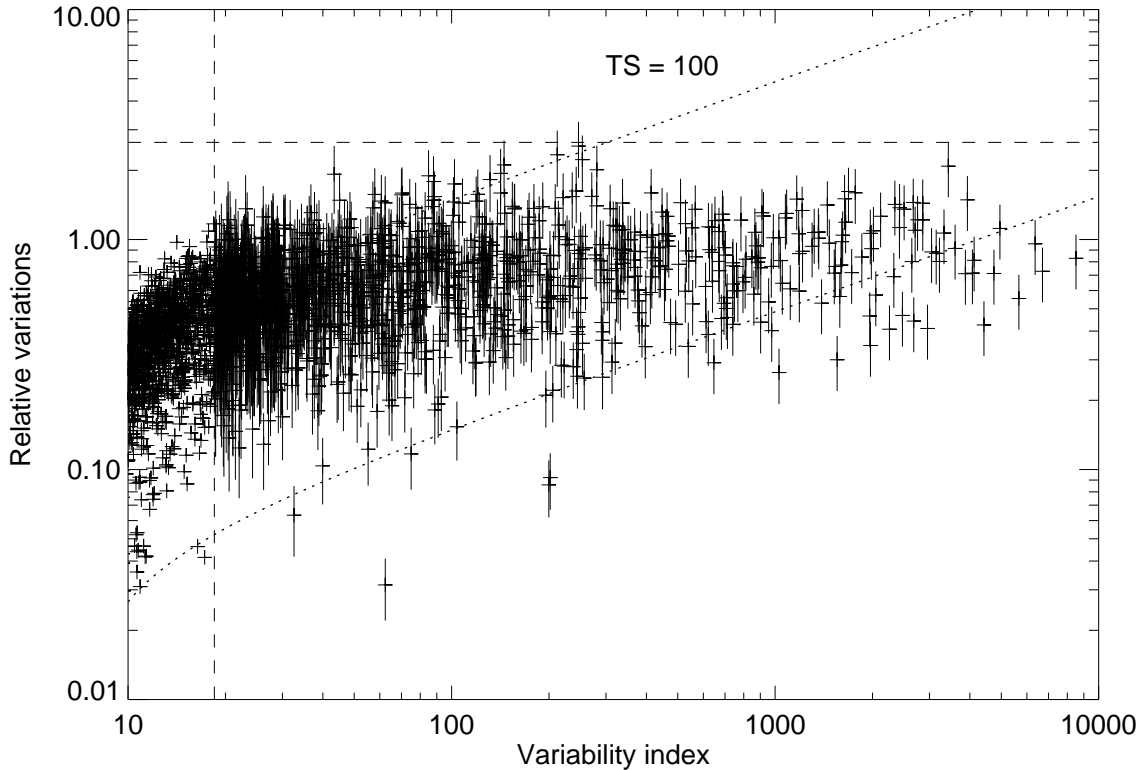


Figure 7. Fractional variability of all sources plotted as a function of variability index. The vertical dashed line (below which the points have no error bar) is the variability threshold. The horizontal dashed line is the maximum fractional variability that can be reached ($\sqrt{N_{\text{int}} - 1}$). The dotted lines show how the variability index depends on $\delta F/F$ at $TS = 100$ and at $TS = 10,000$. At a given TS threshold, the lower right part of the diagram is not accessible. The error bars are omitted below the variability threshold for clarity.

613 the lower part of the plot. There is no indication that fainter sources are less variable than brighter
 614 ones, but we simply cannot measure their variability.

615 3.7. Limitations and Systematic Uncertainties

616 3.7.1. Diffuse emission model

617 The model of diffuse emission is the main source of uncertainties for faint sources. Contrary to the
 618 effective area, it does not affect all sources equally: its effects are smaller outside the Galactic plane
 619 where the diffuse emission is fainter and varying on larger angular scales. It is also less of a concern
 620 at high energy (> 3 GeV) where the core of the PSF is narrow enough that the sources dominate the
 621 background under the PSF. But it is a serious concern inside the Galactic plane at low energy ($<$
 622 1 GeV) and particularly inside the Galactic ridge ($|l| < 60^\circ$) where the diffuse emission is strongest
 623 and very structured, following the molecular cloud distribution. It is not easy to assess precisely how
 624 large the uncertainties are, because they relate to uncertainties in the distributions of interstellar gas,
 625 the interstellar radiation field, and cosmic rays, which depend in detail on position on the sky.

626 We estimate, from the residuals over the entire Galactic plane, that the systematics are at the
 627 3% level. This is already an achievement, but the statistical Poisson errors corresponding to the
 628 diffuse emission integrated over the PSF (as described in Appendix B) are much smaller than this.

629 Integrating energies up to twice the current one in the Galactic ridge, the statistical precision is 0.2,
 630 0.4, 1, 2, 5% above 100, 200, 500 MeV, 1, 2 GeV respectively.

631 The weights are able to mitigate the systematic effects globally, but cannot correct the model
 632 locally. In particular underestimating the mass of an interstellar cloud will always tend to create
 633 spurious sources on top of it, and overestimating diffuse emission at a particular place tends to make
 634 the sources on top of it harder than they should be (because the model creates negative residuals
 635 there, and those are felt mostly at low energy).

636 3.7.2. *Analysis method*

637 As in 3FGL, we use the *pointlike*-based method described in § 3.1 to estimate systematic errors due
 638 to the way the main *gtlike*-based method (§ 3.2) is set up in detail. Many aspects differ between the
 639 two methods: the code, the weights implementation, the RoIs, and the diffuse model adjustments.
 640 The *pointlike*-based method does not remove faint sources (with $TS < 25$) from the model. Even
 641 the data differ, since the *pointlike*-based method uses *Front* and *Back* event types whereas the
 642 *gtlike*-based method uses PSF event types with a different zenith angle cut. Both methods reject a
 643 fraction of the events below 1 GeV, but not the same one.

644 Because of all those differences, we expect that comparing the results of the two methods source
 645 by source can provide an estimate of the sensitivity of the source list to details of the analysis. In
 646 particular we use it to flag sources whose spectral characterization differs a lot with the two methods
 647 (Flags 1 and 3 in Table 5).

648 3.7.3. *Analysis Flags*

649 As in 3FGL we identified a number of conditions that should be considered cautionary regarding
 650 the reality of a source or the magnitude of the systematic uncertainties of its measured properties.
 651 They are described in Table 5, together with the number of sources flagged for each reason. Flags
 652 1, 2 and 3 alert to a different result with *pointlike* or the previous diffuse model. Flag 4 indicates
 653 a low source to background ratio. Flag 5 alerts to confusion, flag 9 to a bad localization, flag 10 to
 654 a bad spectral representation and flag 12 to a very highly curved spectrum. Flag 6 is not filled yet.
 655 The localization check with *gtfindsrc* (flag 7 in 3FGL) was not done because unbinned likelihood is
 656 very slow and does not support energy dispersion nor weights. The Sun check (flag 11 in 3FGL) is
 657 not necessary any more since we now have a good model of the Sun.

658 In total 1081 sources are flagged in 4FGL (about 21%, similar to 3FGL). Only 14% of the sources
 659 with power-law index $\Gamma < 2.5$ are flagged, but 43% of the soft sources with $\Gamma \geq 2.5$. This attests
 660 of the exacerbated sensitivity of soft sources to the underlying background emission. For the same
 661 reason, and also because of more confusion, 50% of sources close to the Galactic plane (latitude less
 662 than 10°) are flagged while only 10% outside that region are. Only 14% of associated sources are
 663 flagged but 42% of the non-associated ones are flagged. This is in part because the associated sources
 664 tend to be brighter, therefore more robust, and also because many flagged sources are close to the
 665 Galactic plane where the association rate is low.

666 4. THE 4FGL CATALOG

667 4.1. *Catalog Description*

Table 5. Definitions of the Analysis Flags

Flag ^a	N_{sources}	Meaning
1	215	Source with $TS > 35$ which went to $TS < 25$ when changing the diffuse model (§ 3.7.1) or the analysis method (§ 3.7.2). Sources with $TS \leq 35$ are not flagged with this bit because normal statistical fluctuations can push them to $TS < 25$.
2	216	Moved beyond its 95% error ellipse when changing the diffuse model.
3	342	Flux (> 1 GeV) or energy flux (> 100 MeV) changed by more than 3σ when changing the diffuse model or the analysis method. Requires also that the flux change by more than 35% (to not flag strong sources).
4	212	Source-to-background ratio less than 10% in highest band in which $TS > 25$. Background is integrated over πr_{68}^2 or 1 square degree, whichever is smaller.
5	320	Closer than θ_{ref}^b from a brighter neighbor.
6	...	Not used.
7	...	Not used.
8	...	Not used.
9	136	Localization Quality > 8 in <i>pointlike</i> (§ 3.1) or long axis of 95% ellipse > 0.25 .
10	27	$\sum_i S_i^2 > 20.5$ or $S_i^2 > 9$ in any band (Eq. 4).
11	...	Not used.
12	102	Highly curved spectrum; LP_beta fixed to 1 or PLEC_Index fixed to 0 (see § 3.3).

^aIn the FITS version (Table 9 in Appendix A) the values are encoded as individual bits in a single column, with Flag n having value $2^{(n-1)}$.

^b θ_{ref} is defined in the highest band in which source $TS > 25$, or the band with highest TS if all are < 25 . θ_{ref} is set to 1.68 (FWHM) below 300 MeV, 1.03 between 300 MeV and 1 GeV, 0.76 between 1 GeV and 3 GeV (in-between FWHM and $2r_{68}$), 0.49 between 3 and 10 GeV and 0.25 above 10 GeV ($2r_{68}$).

668 The catalog contains 5065 sources⁸. The source designation is 4FGL JHHMM.m+DDMM where the 4
669 indicates that this is the fourth LAT catalog, FGL represents *Fermi* Gamma-ray LAT. The 75 sources
670 that were modeled as extended for 4FGL (§ 3.4) are singled out by an e appended to their names.
671 The catalog columns are described in Appendix A. Figure 8 illustrates the distribution of the 4FGL
672 sources over the sky, separately for AGN (blue) and other (red) classes.

673 4.2. Comparison with 3FGL and earlier

674 4.2.1. General comparison

675 Figure 9 shows the energy flux distribution in 1FGL, 2FGL, 3FGL and 4FGL. Comparing the
676 current flux threshold with those published in previous LAT Catalog papers we see that in 4FGL the
677 threshold is down to $\simeq 2 \times 10^{-12}$ erg cm⁻² s⁻¹, quantifying the gain from 3FGL. Above 10^{-11} erg cm⁻²
678 s⁻¹ the 2FGL and 3FGL distributions are entirely compatible with 4FGL. The 1FGL distribution
679 shows a distinct bump between 1 and 2×10^{-11} erg cm⁻² s⁻¹. That accumulation of fluxes was clearly
680 incorrect. We attribute it primarily to overestimating significances and fluxes due to the unbinned
681 likelihood bias in the 1FGL analysis, and also to the less accurate procedure then used to extract
682 source flux (see discussion in the 2FGL paper).

683 The threshold at low flux is less sharp in 4FGL than it was in 2FGL or 3FGL. This reflects a larger
684 dependence of the detection threshold on the power-law index (Figure 10). The expected detection

⁸ The file has 5066 entries because the PWN component of the Crab Nebula is represented by two cospatial sources (§ 3.3).

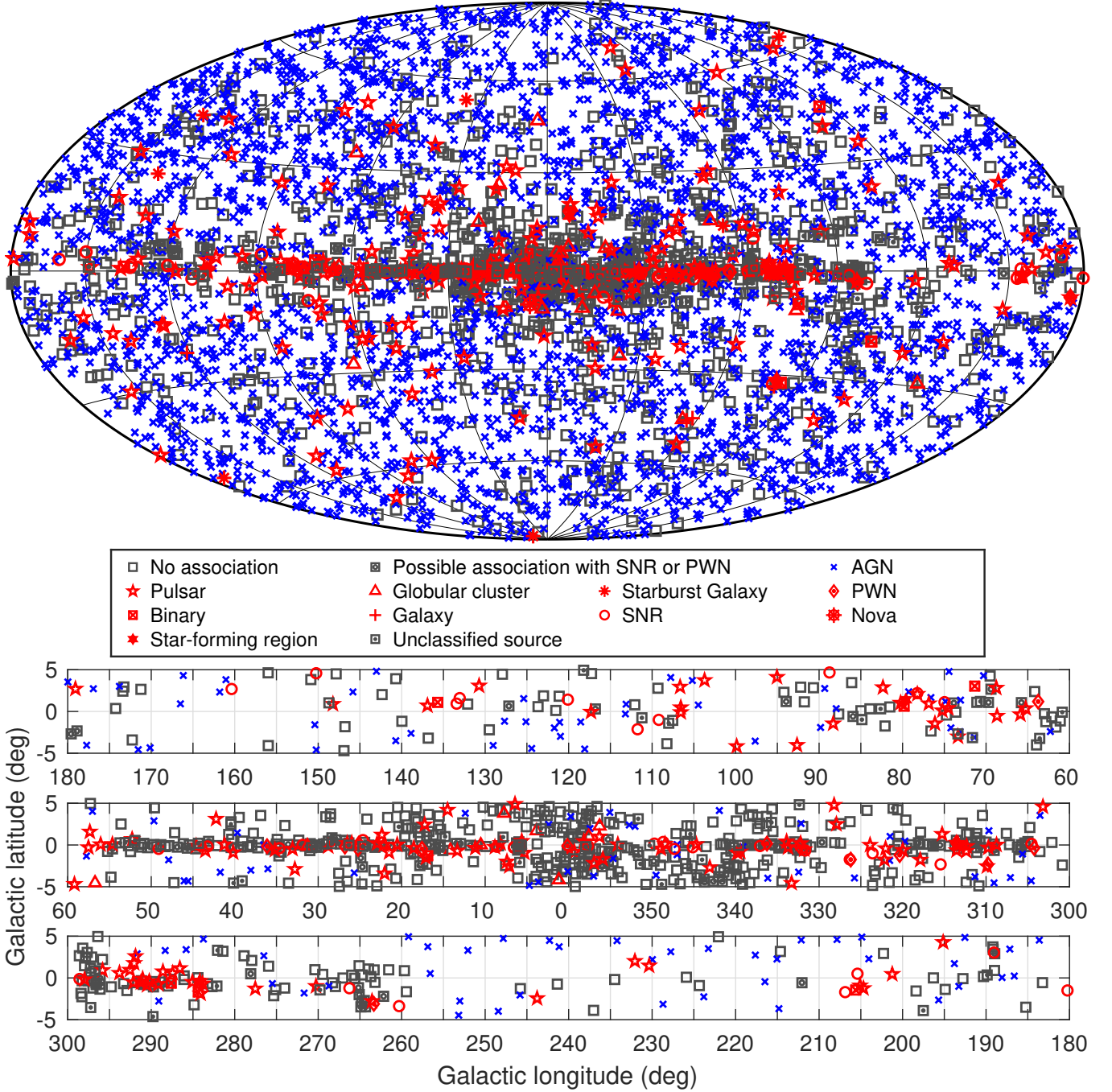


Figure 8. Full sky map (top) and blow-up of the Galactic plane split into three longitude bands (bottom) showing sources by source class (see Table 7, no distinction is made between associations and identifications). All AGN classes are plotted with the same blue symbol for simplicity. Other associations to a well-defined class are plotted in red. Unassociated sources and sources associated to counterparts of unknown nature are plotted in black.

685 threshold is computed from Eq. A1 of [Abdo et al. \(2010a\)](#). The systematic limitation ϵ (entered in
 686 the weighted log-likelihood as described in Appendix B) is accounted for approximately by limiting
 687 the integral over angles to $\theta_{max}(E)$ such that $g(\theta_{max}, E) = \epsilon$, since $g(\theta_{max}, E)$ in that equation is

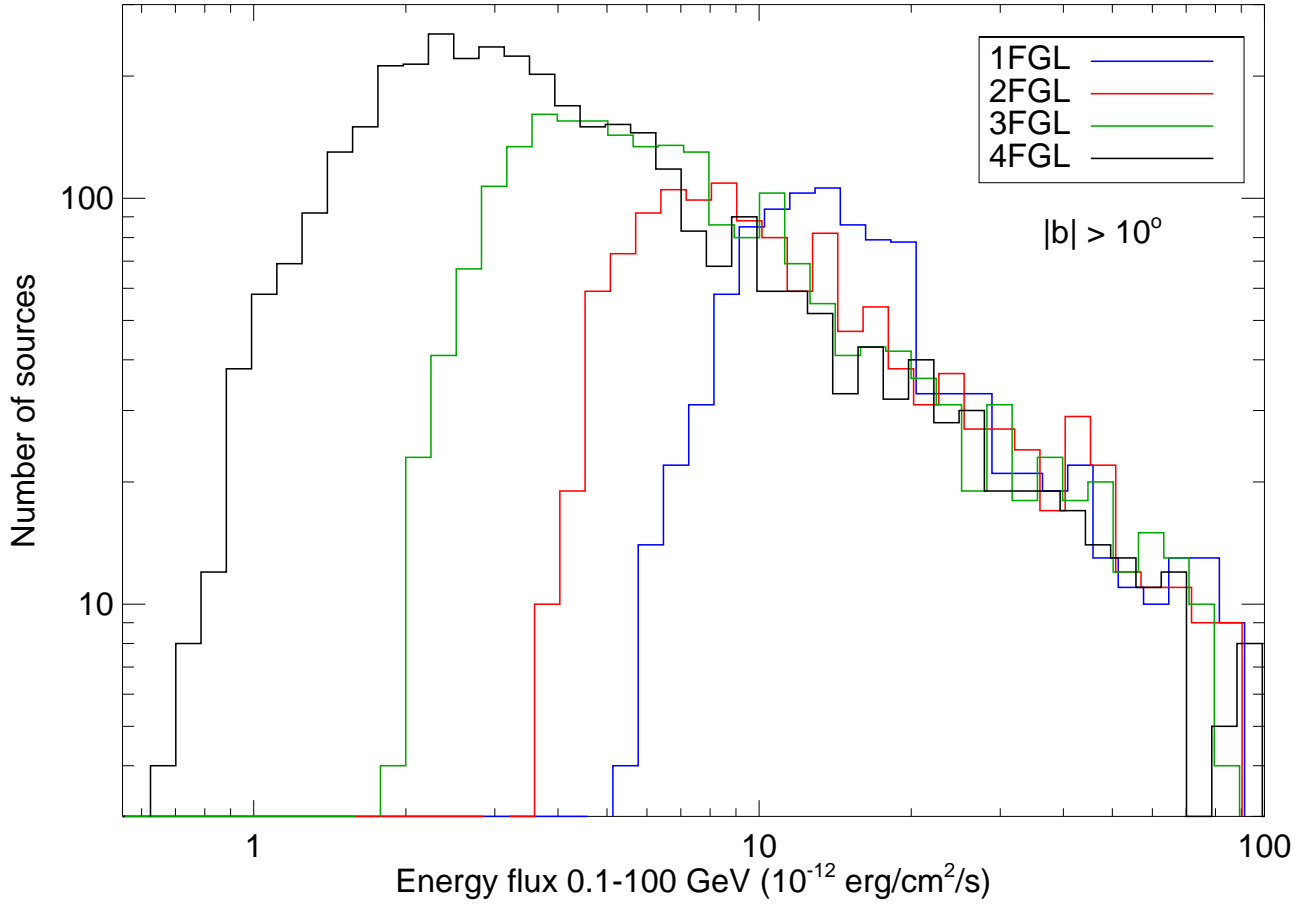


Figure 9. Distributions of the energy flux for the high-latitude sources ($|b| > 10^\circ$) in the 1FGL (1043 sources, blue), 2FGL (1319 sources, red), 3FGL (2193 sources, green) and 4FGL (3647 sources, black) catalogs, illustrating the approximate detection threshold.

688 exactly the source to background ratio. The detection threshold for soft sources decreases only slowly
 689 with exposure due to that.

690 The power-law index Γ is a way to compare all sources over all catalog generations, ignoring
 691 the complexities of the curved models. Figure 11 shows the four distributions of the power-law
 692 indices of the sources at high Galactic latitude are very similar. Their averages and widths are
 693 $\Gamma_{1\text{FGL}} = 2.22 \pm 0.33$, $\Gamma_{2\text{FGL}} = 2.17 \pm 0.30$, $\Gamma_{3\text{FGL}} = 2.22 \pm 0.31$ and $\Gamma_{4\text{FGL}} = 2.23 \pm 0.30$.

694 Small differences in the power-law index distributions could be related to slightly different
 695 systematic uncertainties in the effective area between the IRFs used respectively for 4FGL, 3FGL,
 696 2FGL, and 1FGL (Table 1). There is actually no reason why the distribution should remain the
 697 same, since the detection threshold depends on the index and the log N-log S of flat-spectrum radio
 698 quasars, which are soft *Fermi* sources, differs from that of BL Lacs, which are hard in the *Fermi* band
 699 (Ackermann et al. 2015, Fig. 7). The apparent constancy may largely be the result of competing
 700 effects.

701 We have compared the distribution of error radii (defined as the geometric mean of the semi-
 702 major and semi-minor axes of the 95% confidence error ellipse) of the 1FGL, 2FGL, 3FGL and

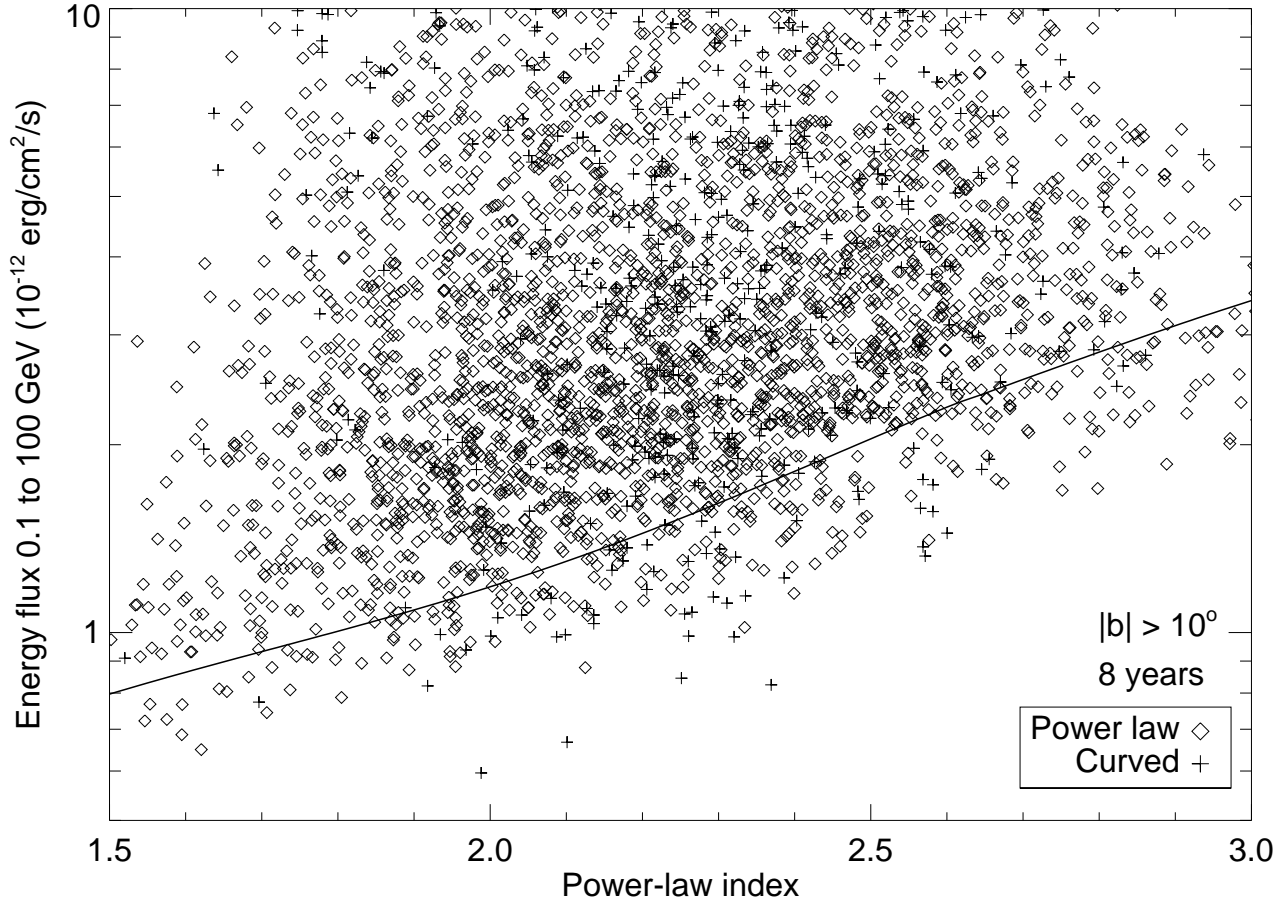


Figure 10. Energy flux and power-law index of all sources outside the Galactic plane ($|b| > 10^\circ$). The full line shows the expected detection threshold for a power-law spectrum. It is consistent with the fluxes of detected power-law sources (diamonds). A number of curved sources (+ signs) are distinctly below that curve. Indeed the detection threshold (in terms of energy flux from 100 MeV to 100 GeV) is lower for curved sources.

703 4FGL sources at high Galactic latitude. Overall the source localization improves mechanically as
 704 more photons are added to previously detected sources. We concentrate instead on what happens
 705 specifically for faint sources. Figure 12 shows the distribution of 95% confidence error radii for those
 706 sources with $25 < TS < 100$ in any of the catalogs. The improvement at a given TS level is partly
 707 due to the event-level analysis (from Pass 6 to 7 and 8, see Table 1) and partly to the fact that, at a
 708 given significance level and for a given spectrum, fainter sources over longer exposures are detected
 709 with more photons. This improvement is key to preserving a high rate of source associations (§ 6)
 710 even though the source density increases.

711

4.2.2. Step-by-step from 3FGL to 4FGL

712 In order to understand the improvements of the 4FGL analysis with respect to 3FGL, we have
 713 considered the effects of changing the analysis and the data set without changing the time range (i.e.,
 714 leaving it as four years). To that end we started with the same seeds as the 3FGL catalog, changed

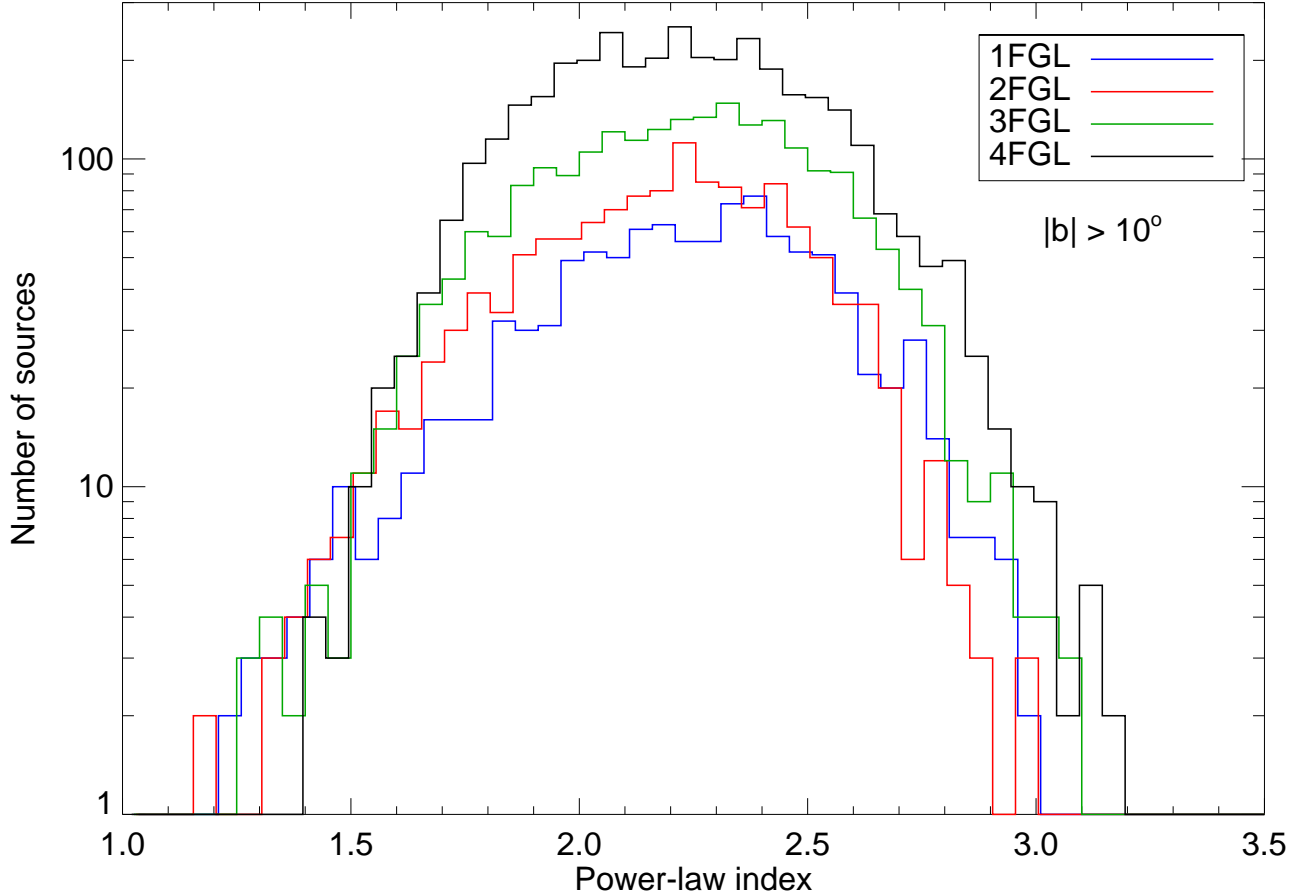


Figure 11. Distributions of the power-law index for the high-latitude sources in the 1FGL (blue), 2FGL (red), 3FGL (green) and 4FGL (black) catalogs. The sources are the same as in Fig 9.

715 each element in sequence (in the order of the list below) and compared each intermediate result with
 716 the previous one. The effect of introducing energy dispersion was described in § 3.2.

- 717
- 718 • We first switched from P7REP to Pass 8, eliminating the Earth limb by cutting zenith angles
 719 $< 90^\circ$ at 100 to 300 MeV and $< 97.5^\circ$ at 300 MeV to 1 GeV for Front, $< 80^\circ$ at 100 to 300 MeV
 720 and $< 95^\circ$ at 300 MeV to 1 GeV for Back. The resulting TS increased by 27%, in keeping with
 721 the effective area increase (the number of sources at $TS > 25$ did not rise, for lack of seeds).
 722 Energy flux decreased by 7% in faint sources. In the Galactic plane sources softened by 0.04
 723 on average. Both effects appear to be due to the diffuse emission modeling, because they are
 724 absent in the bright sources. The isotropic spectrum was recomputed, and even though the
 725 Galactic diffuse model was the same, its effects differed because the effective area increase with
 726 Pass8 is stronger at low energy. Those offsets are accompanied by a large scatter: only 72% of
 P7REP events are still in P8R3, and even for those the reconstructed direction differs.
 - 727 • Switching from Front/Back to PSF event types increased TS by 10% (140 more sources).
 728 This was the intended effect (keep good events and bad ones apart as much as possible). No
 729 systematic effect was noted on energy flux. Soft sources got somewhat softer with PSF event

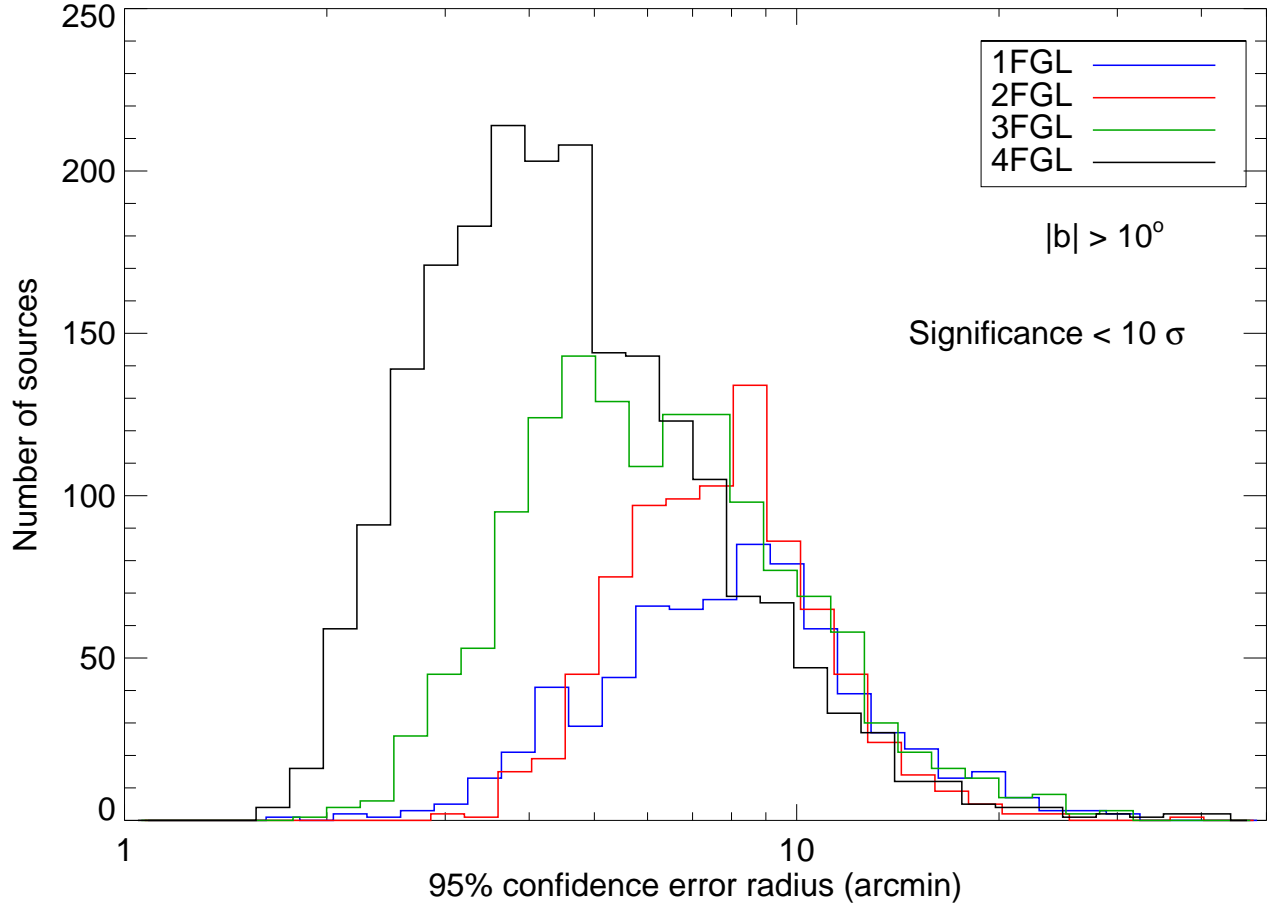


Figure 12. Distributions of the 95% confidence error radii for high-latitude sources with significance < 10 in 1FGL (713 sources, blue), 2FGL (843 sources, red), 3FGL (1387 sources, green) and 4FGL (2091 sources, black), illustrating the improvement of localizations for sources of equivalent detection significances.

730 types (power-law indices larger than 2.7 increased by 0.1 on average), but the bias averaged over
 731 all sources was only +0.01. The number of curved sources decreased by 50 and the curvature β
 732 by 0.025 (this is the same effect: low energies moved up, so spectra got closer to a power law).

- 733 • Applying the weights results in a general decrease of TS and increase of errors, as expected.
 734 However, because source detection is dominated by energies above 1 GeV even without weights,
 735 the effect is modest (the number of sources decreased by only 40). The difference is of course
 736 largest for soft sources and in the Galactic plane, where the background is larger and the weights
 737 are smaller. There are a few other side effects. The number of curved sources went down by
 738 30. This is because the lever arm is less as low energies have been played down. The pivot
 739 energy tended to go up for the same reason, and this resulted in a softening of the power-law
 740 index of curved sources (not exceeding 0.1). Overall in the Galactic ridge the power-law index
 741 increased by 0.025.

742 We evaluated the other two changes on eight years of data:

- 743 • Changing the energy range to start at 50 MeV did not improve TS , as expected (the PSF is
744 too broad below 100 MeV to contribute to significance). The energy flux (defined in the same
745 100 MeV to 100 GeV band) tended to go down in the Galactic plane (by as much as -10% in
746 the Galactic ridge) and the power-law index tended to become harder (by as much as -0.05
747 in the Galactic ridge). This is because the low-energy information tends to stabilize artificially
748 soft sources. Neither effect was noticeable outside the Galactic plane. The other consequence
749 was to increase the number of significantly curved sources by 80, because the broader energy
750 range made it easier to detect curvature (this was true everywhere in the sky).
- 751 • Changing the Galactic diffuse emission model from `gll_iem_v06` used in 3FGL to that used
752 here (§ 2.4), without changing the analysis or the data. The flags in § 3.7.3 are based on
753 comparing to a version of the FL8Y source list (using `gll_iem_v06`) extending the energy
754 range to start at 50 MeV, and using the same extended sources and TS_{curv} threshold as 4FGL.
755 The source significance is lower in 4FGL by 0.1σ on average and the number of sources went
756 down by 10% . The energy flux is lower in 4FGL by 2% , the power-law index is smaller (harder)
757 by 0.02 and there are more curved sources than in FL8Y. This is all because the intensity
758 of the new diffuse model is somewhat higher below 100 MeV. Because this is a background-
759 related effect, it affects primarily the faint sources. The strong overprediction west of Carina
760 in `gll_iem_v06` is gone but overall the residuals are at a similar level.

761 In conclusion, to first order the resulting net changes are not very large, consistent with the general
762 comparison between 4FGL and 3FGL in § 4.2.1. Systematic effects are collectively visible but within
763 calibration errors, and within statistical errors of individual sources.

764

5. AUTOMATED SOURCE ASSOCIATIONS

Table 6. Catalogs Used for the Automatic Source Association Methods

Name	Objects ^a	Ref.
High \dot{E}/d^2 pulsars	313	Manchester et al. (2005) ^b
Other normal pulsars	2248	Manchester et al. (2005) ^b
Millisecond pulsars	240	Manchester et al. (2005) ^b
Pulsar wind nebulae	69	Collaboration internal
High-mass X-ray binaries	137	Chaty et al. (2018)
Low-mass X-ray binaries	187	Liu et al. (2007)
Point-like SNR	158	Green (2014) ^c
Extended SNR ^f	295	Green (2014) ^c
Globular clusters	160	Harris (1996)
Dwarf galaxies ^f	100	McConnachie (2012)
Nearby galaxies	276	Schmidt et al. (1993)
IRAS bright galaxies	82	Sanders et al. (2003)
BZCAT (Blazars)	3561	Massaro et al. (2009)
BL Lac	1371	Véron-Cetty & Véron (2010)
AGN	10066	Véron-Cetty & Véron (2010)
QSO	129,853	Véron-Cetty & Véron (2010)

Table 6 continued on next page

Table 6 (*continued*)

Name	Objects ^a	Ref.
Seyfert galaxies	27651	Véron-Cetty & Véron (2010)
Radio loud Seyfert galaxies	29	Collaboration internal
Radio-loud Seyfert galaxies	556	Rakshit et al. (2017)
FRICAT (Radiogalaxies)	233	Capetti, A. et al. (2017a)
FRIICAT (Radiogalaxies)	123	Capetti, A. et al. (2017b)
Giant Radio Source	349	Kuźmicz et al. (2018)
2WHSP	1691	Chang et al. (2017)
WISE blazar catalog	12319	D’Abrusco et al. (2014)
Radio Fundamental Catalog (2019a)	14786	http://astrogeo.org/rfc
CGRaBS	1625	Healey et al. (2008)
CRATES	11499	Healey et al. (2007)
ATCA 20 GHz southern sky survey	5890	Murphy et al. (2010)
105-month <i>Swift</i> /BAT catalog	1632	Oh et al. (2018)
4 th IBIS catalog	939	Bird et al. (2016)
2nd <i>AGILE</i> catalog ^e	175	Bulgarelli et al. (2019)
3rd EGRET catalog ^e	271	Hartman et al. (1999)
EGR catalog ^e	189	Casandjian & Grenier (2008)
0FGL list ^e	205	Abdo et al. (2009c, 0FGL)
1FGL catalog ^e	1451	Abdo et al. (2010a, 1FGL)
2FGL catalog ^e	1873	Nolan et al. (2012, 2FGL)
3FGL catalog ^e	3033	Acero et al. (2015, 3FGL)
1FHL catalog ^e	514	Ackermann et al. (2013, 1FHL)
2FHL catalog ^e	360	Ackermann et al. (2016b, 1FHL)
3FHL catalog ^e	1556	Ajello et al. (2017, 1FHL)
TeV point-like source catalog ^e	108	http://tevcat.uchicago.edu/
TeV extended source catalog ^f	72	http://tevcat.uchicago.edu/
LAT pulsars	234	Collaboration internal ^d
LAT identified	145	Collaboration internal

^aNumber of objects in the catalog.

^bversion 1.56, <http://www.atnf.csiro.au/research/pulsar/psrcat>

^cGreen D. A., 2017, ‘A Catalogue of Galactic Supernova Remnants (2017 June version)’, Cavendish Laboratory, Cambridge, United Kingdom (available at <http://www.mrao.cam.ac.uk/surveys/snrs/>)

^d<https://confluence.slac.stanford.edu/display/GLAMCOG/Public+List+of+LAT-Detected+Gamma-Ray+Pulsars>

^eFor these catalogs, the association is performed by requiring that the separation from the 4FGL sources is less than the quadratic sum of the 99.9% confidence error radii.

^fFor these catalogs of extended sources, the association is performed by requiring that the separation from the 4FGL sources is less than the quadratic sum of the 95% confidence error radii.

765 The Bayesian method (Abdo et al. 2010a) for the *Fermi*-LAT, implemented with the *gtsrcid* tool⁹,
 766 was developed following the prescription devised by Mattox et al. (1997) for EGRET. It relies on
 767 the fact that the angular distance between a LAT source and a candidate counterpart is driven by
 768 i) the position uncertainty in the case of a real association ii) the counterpart density in the case

⁹ <https://fermi.gsfc.nasa.gov/ssc/data/analysis/scitools/overview.html>

769 of a false (random) association. In addition to the angular-distance probability density functions
 770 for real and false associations, the posterior probability depends on a prior. This prior is calibrated
 771 via Monte Carlo simulations so that the number of false associations, N_{false} is equal to the sum of
 772 the association-probability complements. For a given counterpart catalog, the so-obtained prior is
 773 found to be close to N_{assoc}/N_{tot} , where N_{assoc} is the number of associations from this catalog and
 774 N_{tot} is the number of catalog sources. The sum of the association probabilities over all pairs (γ -ray
 775 source, potential counterpart) gives the total number of real associations for a particular catalog. The
 776 total numbers of associations are reported below for the various classes, where the overlap between
 777 associations from different catalogs is taken into account. A uniform threshold of 0.8 is applied to the
 778 posterior probability for the association to be retained. The reliability of the Bayesian associations is
 779 assessed by verifying that the distribution of the angular offset between γ -ray source and counterpart
 780 matches well the expected one in the case of a true association, i.e., a Rayleigh function with its
 781 width parameter given by the sources positional uncertainties.

782 The list of counterpart catalogs, listed in Table 6, includes known γ -ray-emitting source classes:
 783 Active Galactic Nuclei (AGN, Ackermann et al. (2015)), galaxies (Abdo et al. 2010g), pulsars (Abdo
 784 et al. 2013), pulsar-wind nebulae (Ackermann et al. 2011c), supernova remnants (Acero et al. 2016c),
 785 globular clusters (Abdo et al. 2010h), low- and high-mass X-ray binaries (Abdo et al. 2010i, 2009d) or
 786 surveys of candidate blazars at other frequencies (radio, IR, X-rays). The reported source classes are
 787 derived in the same way as in 3FGL. For non-AGN sources, this classification is based on the nature
 788 of the association catalogs. For AGN, the subclasses as flat-spectrum radio quasars (FSRQ), BL Lac-
 789 type objects (BLL), blazar candidates of uncertain type (BCU), radio galaxies (RDG), narrow-line
 790 Seyfert 1 (NLSY1), steep spectrum radio quasar (SSRQ), Seyfert galaxies (SEY) or simply AGN (if no
 791 other particular subclass can be assigned), have been selected according to the counterpart properties
 792 at other wavelengths. Please note that we did not use the blazar classes from the Simbad database
 793 ¹⁰ since some of them correspond to predictions based on the *WISE*-strip approach (D’Abrusco et al.
 794 2014) and not to assessment with the measured strengths of the emission lines.

795 In complement to the Bayesian method, the Likelihood-Ratio (LR) method (Ackermann et al.
 796 2011b, 2015), following de Ruiter et al. (1977) provides supplementary associations with blazar
 797 candidates based on large radio and X-ray surveys: NVSS (Condon et al. 1998), SUMSS (Mauch
 798 et al. 2003), *ROSAT* (Voges et al. 1999, 2000) and AT20G (Murphy et al. 2010). This method is
 799 similar in essence to the Bayesian method but the false association rate is derived from the density
 800 of objects brighter than the considered candidate, assessed from the survey log N-log S distribution.
 801 While the LR method is able to handle large surveys, its fraction of false associations is notably
 802 larger than in the Bayesian method (typically 10% vs 2%). The overlap between the results of the
 803 Bayesian and LR methods is about 75% for blazars. Because the surveys include a large number
 804 of Galactic sources at low Galactic latitudes, the class of $|b| < 10^\circ$ sources associated solely via the
 805 LR-method has been set to ‘UNK’ (standing for unknown) as opposed to the ‘BCU’ class used by
 806 default for sources at larger latitudes.

807 The cross-correlation with previous γ -ray catalogs has been performed by requiring that the 99.9%
 808 ellipse regions overlap (using $r_{99.9}/r_{95}=1.52$). Firm identifications are based on periodic variability

¹⁰ <http://simbad.u-strasbg.fr/simbad/>

809 for LAT-detected pulsars or X-ray binaries, correlated variability at other wavelengths for AGN or
 810 spatial morphology related to that found in another band for extended sources.

811 The association and classification procedures greatly benefited from data of recent intensive follow-
 812 up programs, motivated by the study of the unidentified/unassociated γ -ray sources. This study
 813 was set as one of the major scientific goals of the *Fermi* mission. Many groups carried out follow
 814 up observations and/or applied statistical procedures to investigate and discern the nature of the
 815 unassociated sources from their gamma-ray properties (see e.g., [Ackermann et al. 2012d](#); [Hassan
 816 et al. 2013](#); [Doert & Errando 2014](#)). In particular, follow up campaigns were carried out at different
 817 wavelengths with both ground based and space telescopes above GHz frequencies(see e.g., [Kovalev
 818 2009](#); [Petrov et al. 2011, 2013](#); [Hovatta et al. 2012, 2014](#); [Schinzel et al. 2015, 2017](#)) and below (see
 819 e.g., [Massaro et al. 2013](#); [Nori et al. 2014](#); [Giroletti et al. 2016](#)), or using sub millimeter (see e.g.,
 820 [Giommi et al. 2012](#); [López-Caniego et al. 2013](#)) and infrared observations (see e.g., [Massaro et al.
 821 2011, 2012b,a](#); [Arsioli et al. 2015](#); [Massaro & D’Abrusco 2016](#); [D’Abrusco et al. 2014](#)) up to the
 822 X-rays with *SWIFT* (e.g., [Mirabal & Halpern 2009](#); [Paggi et al. 2013](#); [Takeuchi et al. 2013](#); [Stroh
 823 & Falcone 2013](#); [Acero et al. 2013](#); [Landi et al. 2015](#); [Paiano et al. 2017b](#)) as well as with *Chandra*
 824 and *Suzaku* (e.g., [Maeda et al. 2011](#); [Cheung et al. 2012](#); [Kataoka et al. 2012](#); [Takahashi et al.
 825 2012](#); [Takeuchi et al. 2013](#)). Over the years, these observations allowed new additions to the lists
 826 of potential counterparts, which were then validated and associated with the methods previously
 827 described. In addition, to asses the real nature and classify all newly associated sources, it has been
 828 crucial to perform additional spectroscopic optical observations, which for extragalactic objects were
 829 also able to provide estimates of their cosmological distances (see e.g., [Shaw et al. 2013b,a](#); [Paggi et al.
 830 2014](#); [Massaro et al. 2015b](#); [Ricci et al. 2015](#); [Massaro et al. 2015a](#); [Landoni et al. 2015b,a](#); [Chiaro
 831 et al. 2016](#); [Álvarez Crespo et al. 2016a,b](#); [Landoni et al. 2018](#); [Paiano et al. 2017a,c,d](#); [Peña-Herazo
 832 et al. 2017](#); [Marchesi et al. 2018](#); [Marchesini et al. 2019](#)). These campaigns are continuously updated
 833 including searches in the optical databases of the major surveys (see e.g., [Cowperthwaite et al. 2013](#);
 834 [Massaro et al. 2014](#); [Maselli et al. 2015](#); [Álvarez Crespo et al. 2016c](#); [Massaro et al. 2016](#)).

835 The false-association rate is difficult to estimate for the new associations resulting from these
 836 follow-up observations, preventing them from being treated on the same footing as those obtained
 837 as described above. The most recent RFC catalog includes many new additions that came from
 838 dedicated follow-up observations. Applying the Bayesian method to the whole catalog and retaining
 839 associations with $P > 0.8$, the association probability attached to the recent additions (181 sources)
 840 are reported as NULL to distinguish them for the others.

841

6. ASSOCIATION SUMMARY

842 The association summary is given in table 7. Out of 5065 LAT sources in 4FGL, 1323 are
 843 unassociated (30%). Some 92 others are classified as "unknown", and 90 as "SPP" (sources of
 844 unknown nature but overlapping with known SNR or PWN and thus candidates to these classes),
 845 representing 4% in total. Some 3464 sources are associated with the Bayesian method (1070
 846 associations from this method only, overall $N_{false}=36.6$), 2604 sources with the LR method (210
 847 associations from this method only, $N_{false}= 22.2$ for the latter). The overall association fraction,
 848 70%, is similar to that obtained in previous LAT catalogs. It must be noted that the association
 849 fraction is lower for fainter sources (all bright sources are associated), in particular due to their larger
 850 error regions. This fraction also drops as sources lie closer to the Galactic plane as illustrated in
 851 Figure 13. It decreases from about 85% at high Galactic latitudes to $\simeq 40\%$ close to the Galactic

Table 7. LAT 4FGL Source Classes

Description	Identified		Associated	
	Designator	Number	Designator	Number
Pulsar, identified by pulsations	PSR	229
Pulsar, no pulsations seen in LAT yet	psr	10
Pulsar wind nebula	PWN	12	pwn	6
Supernova remnant	SNR	24	snr	16
Supernova remnant / Pulsar wind nebula	SPP	0	spp	90
Globular cluster	GLC	0	glc	30
Star-forming region	SFR	3	sfr	0
High-mass binary	HMB	5	hmb	3
Low-mass binary	LMB	1	lmb	1
Binary	BIN	1	bin	0
Nova	NOV	1	nov	0
BL Lac type of blazar	BLL	22	bll	1094
FSRQ type of blazar	FSRQ	42	fsrq	644
Radio galaxy	RDG	6	rdg	36
Non-blazar active galaxy	AGN	1	agn	17
Steep spectrum radio quasar	SSRQ	0	ssrq	2
Compact Steep Spectrum radio source	CSS	0	css	5
Blazar candidate of uncertain type	BCU	3	bcu	1327
Narrow line Seyfert 1	NLSY1	4	nlsy1	5
Seyfert galaxy	SEY	0	sey	1
Starburst galaxy	SBG	0	sbg	7
Normal galaxy (or part)	GAL	2	gal	2
Unknown	UNK	0	unk	92
Total	...	356	...	3388
Unassociated	1323

NOTE—The designation ‘spp’ indicates potential association with SNR or PWN. Designations shown in capital letters are firm identifications; lower case letters indicate associations.

852 plane. The reason for such an effect is twofold. First, the number of unassociated Galactic sources is
853 large. Secondly, the flux limits of the extragalactic-counterpart catalogs are larger due to extinction
854 effects in these directions. The properties of the unassociated sources are discussed below.

855 Sources reported as new below mean that they were not in previous FGL catalogs, although their
856 detections may have been reported in other works (e.g., [Arsioli & Polenta 2018](#); [Zhang et al. 2016](#))
857 or in specialized LAT catalogs.

858 6.1. Extragalactic sources

859 6.1.1. Active Galactic Nuclei

860 The largest source population in 4FGL is that of AGN, with 3131 blazars, 42 radio galaxies and
861 35 other AGN. The blazar sample comprises 686 FSRQ, 1116 BLL and 1330 BCU. The detailed
862 properties of the 4FGL AGN, including redshifts and fitted synchrotron-peak positions, will be the
863 subject of the 4LAC companion catalog. We note here that the relative separation in γ -ray spectral
864 hardness between FSRQs and BL Lacs already reported in previous LAC AGN catalogs is confirmed:
865 93% of FSRQs and 81% of BL Lacs have power-law photon indices greater and lower than 2.2
866 respectively. Among the 77 non-blazar AGN, 38 were present in the 3FGL. Note that the location of

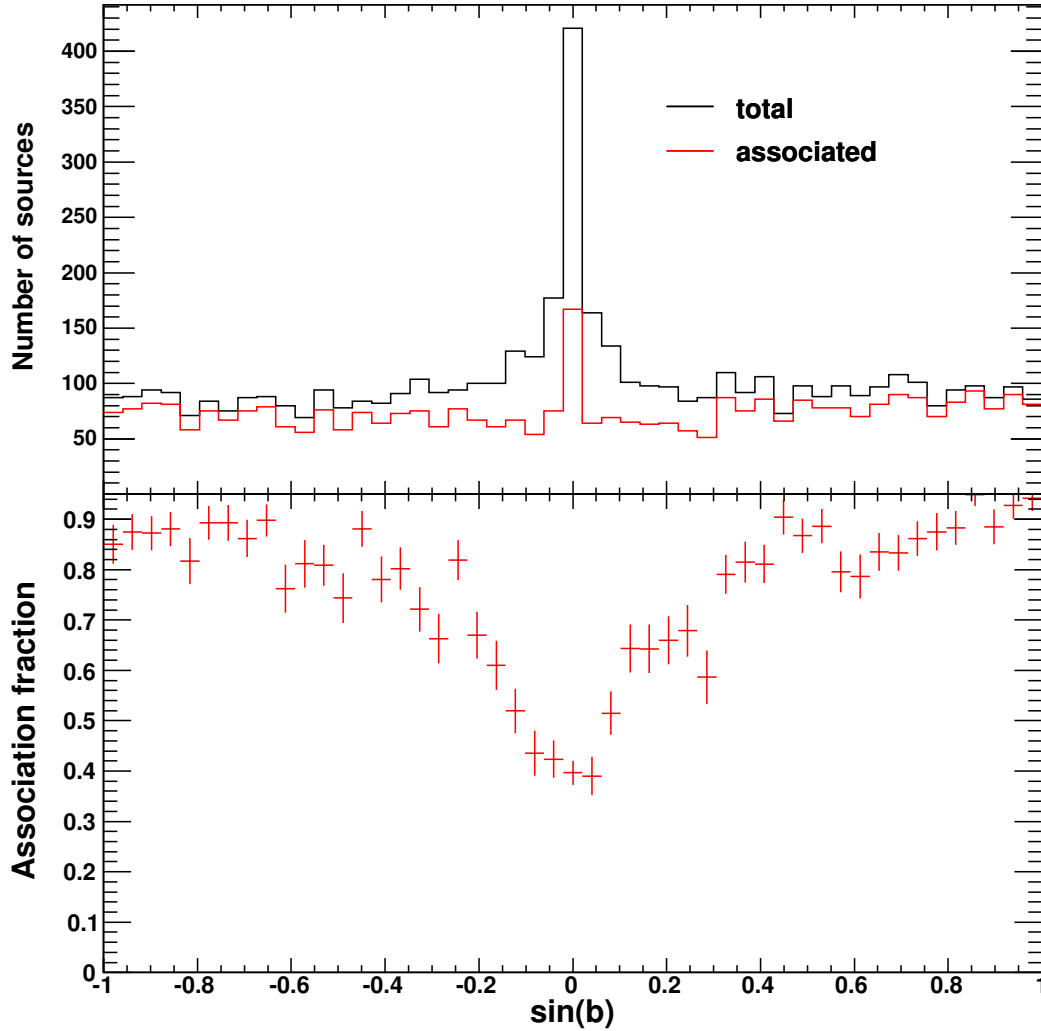


Figure 13. Upper panel: Distributions in Galactic latitude b of 4FGL sources (black histogram) and associated sources (blue histogram). Lower panel: Association fraction as a function of Galactic latitude.

⁸⁶⁷ the γ -ray source associated with Cen B is not coincident with that of the radio-galaxy core but points
⁸⁶⁸ to the southern radio jet. The 18 new radio galaxies are: NGC 315, PKS 0235+017, B3 0309+411B,
⁸⁶⁹ 3C 120, NGC 2329, B2 1113+29, NGC 3894, TXS 1303+114, B2 1447+27, PKS 1514+00, TXS
⁸⁷⁰ 1516+064, PKS B1518+045, PKS 1839–48, PKS 2153–69, PKS 2225–308, PKS 2300–18, PKS
⁸⁷¹ 2324–02, PKS 2327–215, PKS 2338–295. Five 3FGL sources have changed classes to radio galaxies,
⁸⁷² four former bcu (IC 1531, TXS 0149+710, PKS 1304–215, CGCG 050–083) and one former bl (B3
⁸⁷³ 1009+427). The 35 ‘other AGN’ sources include five compact steep spectrum radio sources (CSS,
⁸⁷⁴ three are new: 3C 138, 3C 216, 3C 309.1), two step spectrum radio quasars (SSRQ, new is 3C 212),
⁸⁷⁵ 9 narrow-line Seyferts 1 (NLSY1), one Seyfert galaxy (the Circinus galaxy, SEY) and 18 AGN of
⁸⁷⁶ other types (AGN). Three NLSY1 are new: IERS B1303+515, B3 1441+476, TXS 2116–077.

878 No other nearby galaxies, besides the SMC, LMC, and M 31, are detected. Seven starburst galaxies
 879 in the *IRAS* catalog (Sanders et al. 2003) are associated with 4FGL sources. Two sources, Arp 220
 880 (Peng et al. 2016; Griffin et al. 2016; Yoast-Hull et al. 2017) and NGC 2146 (Tang et al. 2014), have
 881 been reported as LAT detections since the 3FGL release. Yoast-Hull et al. (2017) found an excess
 882 of γ rays over the expected starburst contribution in Arp 220, similar to the case of the Circinus
 883 galaxy (Hayashida et al. 2013). NGC 2146 being close ($0^\circ 1'$) to the FSRQ 1REX J061757+7816.1,
 884 the association is ambiguous. We favor the NGC 2146 association as no evidence for variability is
 885 found and the 4FGL photon index (2.16) is somewhat low for a FSRQ. Another source, NGC 3424,
 886 was not present in 3FGL. The *IRAS* source UGC 11041, which could have been classified as sbg
 887 shows significant variability in the LAT band, so the γ -ray emission most likely arises from an AGN
 888 (there is a flat-spectrum radio source, MG2 J175448+3442 at a distance of $2.4'$) and it is classified as
 889 such. In addition to these seven associations, the Bayesian method predicts that three more 4FGL
 890 sources should be starburst galaxies. Some 4FGL sources are positionally consistent with known
 891 galaxy clusters, but these clusters host radio galaxies which are the most likely emitters. No dwarf
 892 galaxies have been detected.

893 6.2. Galactic sources

894 The Galactic sources include:

- 895 • 239 pulsars (PSR). The public list of LAT-detected pulsars is regularly updated¹¹. Some 229
 896 pulsars in this list are included in 4FGL (65 would have been missed by the association pipeline
 897 using the ATNF catalog), while 6 are absent because they did not pass the $TS > 25$ criterion.
 898 These pulsars represent by far the largest population of identified sources in 4FGL. Another
 899 10 pulsars from the ATNF database are associated with 4FGL sources with high-confidence
 900 via the Bayesian method that we consider γ -ray pulsar candidates. This method predicts that
 901 about 30 extra 4FGL sources are ATNF pulsars. Note that out of the 24 pulsar candidates
 902 presented in 3FGL, pulsations have now been detected for 19 of them. The other 5 are not
 903 associated with pulsars in 4FGL anymore.
- 904 • 40 supernova remnants (SNR). Out of them, 24 are extended and thus firmly identified. The
 905 other 16 are not resolved. SNR G150.3+4.5 having a log-normal spectral shape with a very
 906 hard photon index, Γ of 1.6 indicates that the emission is most likely leptonic and makes this
 907 source an excellent candidate for the Cherenkov Telescope Array (CTA). In contrary, the softer
 908 spectrum of SNR N132D (photon index=2.07) makes the hypothesis of a dominant hadronic
 909 emission likely. The significant spectral curvature seen in Puppis A is in accord with its non-
 910 detection in the TeV domain.
- 911 • 18 pulsar wind nebulae (PWN), 15 of them being extended. New additions are N 157B,
 912 PWN G63.7+1.1, HESS J1356–645, FGES J1631.6–4756, FGES J1836.5–0651, FGES
 913 J1838.9–0704, HESS J1857+026. The median photon index of the 4FGL PWN is 2.31.
 914 N 157B, located in the LMC, has a photon index of 2.0, hinting at an additional contribution
 915 from a (yet-undetected) pulsar at low energy on top of the PWN.

¹¹ See <https://confluence.slac.stanford.edu/display/GLAMCOG/Public+List+of+LAT-Detected+Gamma-Ray+Pulsars>

- 916 • 90 unassociated sources overlapping with known PWN or SNR (SPP). The estimation of missed
917 associations of SNR, PWNe and SPP sources is made difficult by the intrinsic spatial extension
918 of the sources; no attempts have thus been made along this line.
- 919 • 30 globular clusters (GLC). Missing relative to 3FGL is 2MS-GC01. The 16 new associations
920 are NGC 362, NGC 1904, NGC 5286, NGC 5904, NGC 6139, NGC 6218, NGC 6304, NGC
921 6341, Terzan 2, Terzan 1, NGC 6402, NGC 6397, GLIMPSE02, GLIMPSE01, NGC 6838, NGC
922 7078. Only 2 extra 4FGL sources are estimated to be globular clusters.
- 923 • Six high-mass X-ray binaries (HMB). The three new sources are HESS J0632+057, which
924 has a reported LAT detection after the 3FGL (Li et al. 2017b), Cyg X-1, an archetypical
925 black-hole binary reported after the 3FGL (Zdziarski et al. 2017; Zanin et al. 2016), and RX
926 J0648.0–4418/HD 49798, which is a peculiar X-ray binary (Mereghetti et al. 2011; Popov et al.
927 2018). We note that the association probability of RX J0648.0–4418/HD 49798 is just barely
928 larger (0.85 vs 0.80) than that of the blazar candidate SUMSS J064744–441946. Three extra
929 4FGL sources are estimated to be HMB according to the Bayesian method.
- 930 • Three star-forming regions; new since 3FHL is the association of the extended source FHES
931 J1626.9–2431 (§ 3.4) with the ρ Ophiuchi star-forming region.
- 932 • Two low-mass X-ray binaries (LMB). PSR J1023+0038 is a known binary MSP/LXB transition
933 system, with a change in γ -ray flux detected (Stappers et al. 2014) simultaneously with a state
934 change, and was previously detected as 2FGL J1023.6+0040 (but not detected in the 3FGL).
935 The LMB 2S 0921–630 (V395 Car) is a well-studied binary involving a neutron star and a K0
936 III star with an orbital period of 9 days (Shahbaz & Watson 2007) and is a new LAT detection.
- 937 • One binary star (BIN), η Carinae.
- 938 • One nova, V5668 Sagittarii (Cheung et al. 2016). Other novae detected by the LAT are missing.
939 Novae have short durations, and most are below the significance threshold because their signal
940 is diluted over the eight years of 4FGL data.

941 6.3. *Low-probability associations*

942 As a new feature relative to previous catalogs, the most probable counterpart to a 4FGL
943 unassociated source is given in a separate column of the FITS table, along with the corresponding
944 association probability (applying a threshold of 0.1 on that probability). This additional information,
945 to be used with care given its low confidence, is meant to foster further investigations regarding the
946 nature of these 4FGL sources and to help clarify why detections claimed in other works are sometimes
947 missing in 4FGL. We report 124 low-confidence ($0.1 < P < 0.8$) associations with the Bayesian method.
948 Note that the relative distances between γ -ray and counterpart sources remain quite small (53 are
949 within r_{95} and all within $1.85 r_{95}$). This quite small number of low-association sources illustrates
950 how quickly the Bayesian association probability drops with increasing relative distance in the case
951 of 4FGL. Except for rare exceptions, the other 1199 4FGL sources (having not even low-confidence
952 associations) will not get associated with any of the tested sources (i.e., belonging to the catalogs
953 listed in Table 6) in the very near future. We also report 42 matches (classified as "UNK") with
954 sources from the *Planck* surveys (with $0.1 < P < 1$) to guide future investigations.

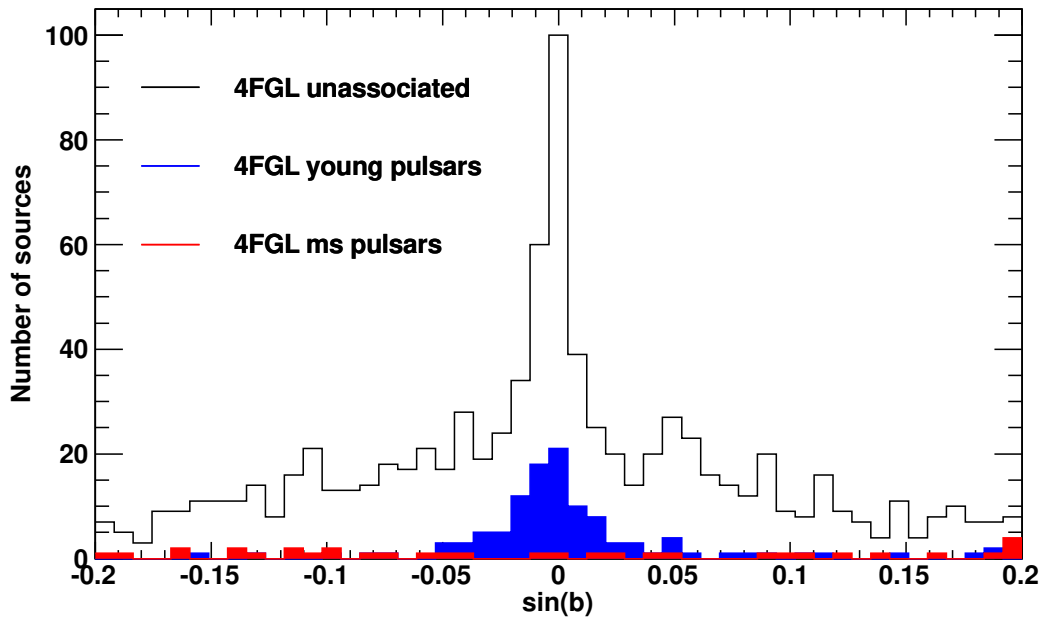


Figure 14. Distributions in Galactic latitude b of 4FGL unassociated sources (black histogram) compared to those of LAT-detected pulsars (young pulsars: blue histogram, millisecond pulsars: red histogram).

955

6.4. Unassociated sources

956 Out of the 1323 sources unassociated in 4FGL, 368 already present in 3FGL had no associations
 957 there. Another 27 sources previously associated in 3FGL have now lost their associations because of
 958 a shift in their locations relative to 3FGL.

959 About half of the unassociated sources are located less than 10° away from the Galactic plane.
 960 Their wide latitude extension is hard to reconcile with those of known classes of Galactic γ -ray
 961 sources. For instance, Figure 14 compares this latitude distribution with that of LAT pulsars. In
 962 addition to nearby millisecond pulsars, which have a quasi isotropic distribution, the LAT detects
 963 only young isolated pulsars (age $< 10^6$ y) which are by nature clustered close to the plane. Older
 964 pulsars, which have had time to drift further off the plane, show a wider Galactic-latitude distribution,
 965 more compatible with the observed distribution of the unassociated sources, but these pulsars have
 966 crossed the ‘ γ -ray death line’ and are hence undetectable. Attempts to spatially cross correlate the
 967 unassociated population with other potential classes, e.g., LMXB (Liu et al. 2007), O stars¹², B stars
 968¹³ have been unsuccessful. The observed clustering of these unassociated sources in high-density ‘hot
 969 spots’ may be a clue that they actually correspond to yet-to-be identified, relatively nearby extended
 970 sources. The Galactic latitude distribution near the plane is clearly non-gaussian as visible in Figure
 971 14, which may indicate the presence of several components.

972 The spectral properties of these sources as well can provide insight into their nature, as illustrated
 973 in Figure 15 showing the power-law photon index versus the Galactic latitude. The change in spectral
 974 hardness with sky location demonstrates the composite nature of the unassociated population. The

¹² GOSC <https://gosc.cab.inta-csic.es/>

¹³ BeSS <http://basebe.obspm.fr/basebe/>

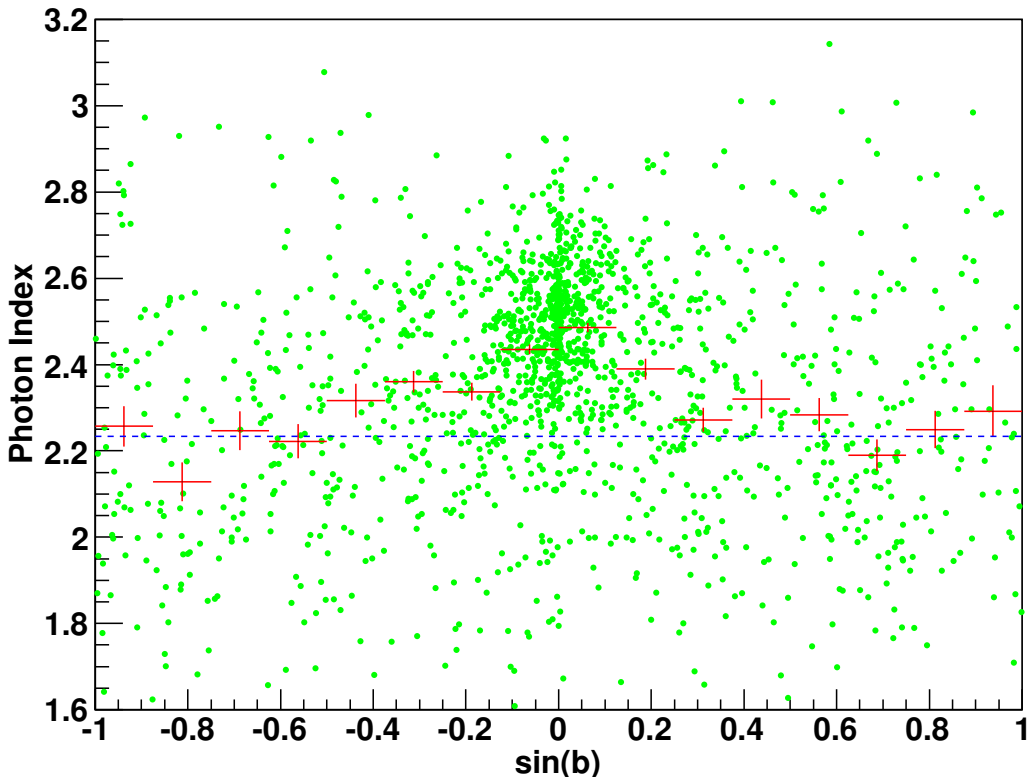


Figure 15. Green symbols: Power-law photon index versus Galactic latitude, b , for the unassociated 4FGL sources. Red bars: average photon index for different bins in b . Dashed blue line: average photon index of 4FGL BCU blazars.

975 high-latitude sources shows an average photon index compatible with that of blazars of unknown
 976 type ($\Gamma=2.24$), a hint that these sources could predominantly be blazars. Unassociated sources lying
 977 closer to the Galactic plane have softer spectra, closer to that expected of young pulsars ($\Gamma=2.42$).
 978 Another interesting possibility is that some of these unassociated sources actually correspond to
 979 WIMP dark matter annihilating in Galactic subhalos (Ackermann et al. 2012e). Indeed, Λ CDM
 980 cosmology predicts the existence of thousands of them below $\sim 10^7 M_{\odot}$, i.e., not massive enough to
 981 retain gas or stars at all. As a result, they are not expected to emit at other wavelengths and therefore
 982 they would not possess astrophysical counterparts. Interestingly, this dark matter annihilation may
 983 yield a pulsar-like spectrum (Baltz et al. 2007).

984 *6.5. Sources missing from previous catalogs*

985 Out of 3033 3FGL sources, 410 are missing in 4FGL for various reasons, including the change of
 986 diffuse emission model, point sources being absorbed into new extended ones or variability effects.
 987 Most of these missing sources had low significance in 3FGL. Only 74 sources were associated. The
 988 majority are blazars (32 BCU, 15 FSRQ, 1 BLL and 1 SSRQ) plus one AGN. It is remarkable that
 989 while BLL are 36% more numerous relative to FSRQ in 3FGL, a much lower fraction (by a factor of
 990 20) has gone away in 4FGL, an effect possibly related to the larger variability of FSRQ relative to BLL
 991 observed in the LAT energy band (Ackermann et al. 2015). Other missing sources include 20 SPP, 2

992 PSR and one PWN. The nova V407 Cyg is now missing as it no longer fulfills the average-significance
993 criterion.

994 Concerning sources missing from 3FHL, established with the same data set, they amount to 30,
995 with 14 unassociated, 10 blazars (4 BLL and 6 BCU), 1 AGN, 4 ‘unknown’ and the HMB PSR
996 B1259–63. All these sources had a TS close to the $TS = 25$ significance threshold.

997

6.6. *TeV sources***Table 8.** Associations of 4FGL with Extended TeV Sources

TeVCat Name ^a	4FGL Name
Boomerang	J2229.0+6114
CTA 1	J0007.0+7303
CTB 37A	J1714.4–3830
CTB 37B	J1714.1–3811
Crab	J0534.5+2201e
G318.2+00.1	J1453.4–5858
Geminga	J0633.9+1746
HESS J1018–589 B	J1016.3–5857
HESS J1026–582	J1028.5–5819
HESS J1303–631	J1303.0–6312e
HESS J1356–645	J1355.2–6420e
HESS J1420–607	J1420.3–6046e
HESS J1427–608	J1427.8–6051
HESS J1458–608	J1456.7–6050, J1459.5–6053
HESS J1507–622	J1507.9–6228e
HESS J1534–571	J1533.9–5712e
HESS J1614–518	J1615.3–5146e
HESS J1616–508	J1616.2–5054e
HESS J1632–478	J1633.0–4746e
HESS J1640–465	J1640.6–4632
HESS J1702–420	J1705.7–4124
HESS J1718–385	J1718.2–3825
HESS J1729–345	J1730.1–3422
HESS J1745–303	J1745.8–3028e
HESS J1800–240 A	J1801.8–2358
HESS J1800–240B	J1800.2–2403 , J1800.7–2355 , J1800.9–2407
HESS J1804–216	J1804.7–2144e
HESS J1808–204	J1808.2–2028e
HESS J1809–193	J1810.3–1925e
HESS J1813–126	J1813.4–1246
HESS J1813–178	J1813.1–1737e
HESS J1825–137	J1824.5–1351e
HESS J1826–130	J1826.1–1256
HESS J1834–087	J1834.5–0846e
HESS J1841–055	J1840.9–0532e
HESS J1848–018	J1847.2–0141, J1848.6–0202, J1848.7–0129
HESS J1857+026	J1857.7+0246e
HESS J1858+020	J1858.3+0209

Table 8 continued on next page

Table 8 (*continued*)

TeVCat Name ^a	4FGL Name
HESS J1912+101	J1911.7+1014, J1912.7+0957, J1913.3+1019
IC 443	J0617.2+2234e
Kookaburra (Rabbit)	J1417.7–6057, J1418.7–6057
Kookaburra PWN	J1420.0–6048
MGRO J1908+06	J1906.2+0631, J1907.9+0602
MGRO J2031+41	J2028.6+4110e
MSH 15–52	J1514.2–5909e
RCW 86	J1443.0–6227e
RX J0852.0–4622	J0851.9–4620e
RX J1713.7–3946	J1713.5–3945e
SNR G292.2–00.5	J1119.1–6127
TeV J1626-490	J1628.2-4848
Terzan 5	J1748.0–2446
VER J2019+407	J2021.0+4031e
Vela X	J0833.1-4511e
W 28	J1801.3–2326e
W 51	J1923.2+1408e
Westerlund 1	J1645.8–4533, J1648.4–4611, J1649.2–4513, J1650.3–4600, J1652.2–4516
Westerlund 2	J1023.3–5747e

^aFrom <http://tevcat.uchicago.edu>.

998 The synergy between the LAT and the Cherenkov telescopes operating in the TeV energy domain
999 has proven extremely fruitful, in particular by bringing out promising TeV candidates in the LAT
1000 catalogs. This approach, further motivated by the upcoming deployment of the Cherenkov Telescope
1001 Array, has justified the release of LAT source catalogs above 10 GeV, like the 3FHL (Ajello et al. 2017)
1002 based on 7 years of data. The associations of 4FGL sources with extended sources listed in TeVCat¹⁴
1003 are presented in Table 8. Relative to 3FHL, 9 new extended TeV sources are associated with 4FGL
1004 extended sources (TeV sources: HESS J1534–571, HESS J1808–204, HESS J1809–193, see § 3.4), or
1005 (sometimes multiple) 4FGL point sources (TeV sources: HESS J1718–385, HESS J1729–345, HESS
1006 J1848–018, HESS J1858+020, MGRO J1908+06, HESS J1912+101). All TeV blazars have 4FGL
1007 counterparts. The median value of Γ for 4FGL point sources associated with TeV point sources is
1008 1.95, indicating hard spectra as expected. In associations with extended TeV sources, the median Γ
1009 changes from 2.09 to 2.38 depending on whether the 4FGL sources are extended or not. This fairly
1010 large difference favors the interpretation that most associations between extended TeV sources and
1011 non-extended 4FGL sources are accidental.

1012

6.7. Counterpart positions

1013 Whenever a high-confidence association with a point-like counterpart is obtained, we provide the
1014 most accurate counterpart position available and its uncertainty. In particular, 2292 4FGL AGN
1015 have Very Long Baseline Interferometry (VLBI) counterparts. VLBI, i.e., radio interferometry with
1016 baseline lengths of >1000 km is sensitive to radio emission from compact regions of AGN that are
1017 smaller than 20 milliarcsecond (mas), which corresponds to parsec scales. Such observations allow

¹⁴ <http://tevcat.uchicago.edu/>

1018 the determination of positions of the AGN jet base with mas level accuracy. We used the Radio
 1019 Fundamental Catalog¹⁵ based on the dedicated on-going observing program (Schinzel et al. 2015,
 1020 2017) with the Very Long Baseline Array (Napier et al. 1994), as well as VLBI data under other
 1021 programs. The association between γ -ray source and VLBI counterpart was carried out along a
 1022 similar, but distinct, scheme as that presented in § 5. This scheme (see Petrov et al. (2013) for more
 1023 details) is based on the strong connection between the γ -ray emission and radio emission at parsec
 1024 scales and on the sky density of bright compact radio sources being relatively low. The chance to
 1025 find a bright background, unrelated compact radio source within the LAT positional error ellipse is
 1026 low enough to establish association. The likelihood ratio (with a somewhat different definition from
 1027 that implemented in the LR-method) was required to be greater than 8 to claim an association, with
 1028 an estimated false association fraction of 1%.

1029 For AGN without VLBI counterparts, the position uncertainties were set to typical values of
 1030 20'' for sources associated from the RASS survey and 10'' otherwise. For identified pulsars, the
 1031 position uncertainties come from the rotation ephemeris used to find γ -ray pulsations, many of which
 1032 were obtained from radio observations (Smith et al. 2019). If the ephemeris does not include the
 1033 uncertainties and for pulsar candidates, we use the ATNF psrcat values. If neither of those exist, we
 1034 use the 0.1° uncertainties from the list maintained by the WVU Astrophysics group¹⁶. Ephemeris
 1035 position uncertainties are often underestimated, so we arbitrarily apply a minimum uncertainty of
 1036 1 mas. For globular clusters from Harris (1996), the position uncertainties were assigned a typical
 1037 value of 2''¹⁷.

1038 The *Fermi* LAT Collaboration acknowledges generous ongoing support from a number of agencies
 1039 and institutes that have supported both the development and the operation of the LAT as well as
 1040 scientific data analysis. These include the National Aeronautics and Space Administration and the
 1041 Department of Energy in the United States, the Commissariat à l'Énergie Atomique and the Centre
 1042 National de la Recherche Scientifique / Institut National de Physique Nucléaire et de Physique des
 1043 Particules in France, the Agenzia Spaziale Italiana and the Istituto Nazionale di Fisica Nucleare in
 1044 Italy, the Ministry of Education, Culture, Sports, Science and Technology (MEXT), High Energy
 1045 Accelerator Research Organization (KEK) and Japan Aerospace Exploration Agency (JAXA) in
 1046 Japan, and the K. A. Wallenberg Foundation, the Swedish Research Council and the Swedish National
 1047 Space Board in Sweden.

1048 Additional support for science analysis during the operations phase is gratefully acknowledged from
 1049 the Istituto Nazionale di Astrofisica in Italy and the Centre National d'Études Spatiales in France.
 1050 This work performed in part under DOE Contract DE-AC02-76SF00515.

1051 This work made extensive use of the ATNF pulsar catalog¹⁸ (Manchester et al. 2005). This
 1052 research has made use of the NASA/IPAC Extragalactic Database (NED) which is operated by
 1053 the Jet Propulsion Laboratory, California Institute of Technology, under contract with the National
 1054 Aeronautics and Space Administration, and of archival data, software and online services provided
 1055 by the ASI Science Data Center (ASDC) operated by the Italian Space Agency.

¹⁵ Available at <http://astrogeo.org/rfc>

¹⁶ <http://astro.phys.wvu.edu/GalacticMSPs/GalacticMSPs.txt>

¹⁷ <https://heasarc.gsfc.nasa.gov/w3browse/all/globclust.html>

¹⁸ <http://www.atnf.csiro.au/research/pulsar/psrcat>

1056 This research has made use of Aladin¹⁹, TOPCAT²⁰ and APLpy, an open-source plotting package
 1057 for Python²¹. The authors acknowledge the use of HEALPix²² (Górski et al. 2005). The extended
 1058 sources were taken from the Manitoba SNR catalog (Ferrand & Safi-Harb 2012).

1059 *Facility: Fermi-LAT*

REFERENCES

- 1060 Abdo, A. A., Ackermann, M., Ajello, M., et al.
 1061 2009a, *Astroparticle Physics*, 32, 193,
 1062 doi: [10.1016/j.astropartphys.2009.08.002](https://doi.org/10.1016/j.astropartphys.2009.08.002)
 1063 —. 2009b, *ApJL*, 706, L1,
 1064 doi: [10.1088/0004-637X/706/1/L1](https://doi.org/10.1088/0004-637X/706/1/L1)
 1065 —. 2009c, *ApJS*, 183, 46,
 1066 doi: [10.1088/0067-0049/183/1/46](https://doi.org/10.1088/0067-0049/183/1/46)
 1067 —. 2009d, *ApJL*, 701, L123,
 1068 doi: [10.1088/0004-637X/701/2/L123](https://doi.org/10.1088/0004-637X/701/2/L123)
 1069 —. 2010a, *ApJS*, 188, 405,
 1070 doi: [10.1088/0067-0049/188/2/405](https://doi.org/10.1088/0067-0049/188/2/405)
 1071 —. 2010b, *ApJ*, 712, 459,
 1072 doi: [10.1088/0004-637X/712/1/459](https://doi.org/10.1088/0004-637X/712/1/459)
 1073 —. 2010c, *ApJ*, 713, 146,
 1074 doi: [10.1088/0004-637X/713/1/146](https://doi.org/10.1088/0004-637X/713/1/146)
 1075 —. 2010d, *Science*, 328, 725,
 1076 doi: [10.1126/science.1184656](https://doi.org/10.1126/science.1184656)
 1077 —. 2010e, *ApJ*, 718, 348,
 1078 doi: [10.1088/0004-637X/718/1/348](https://doi.org/10.1088/0004-637X/718/1/348)
 1079 —. 2010f, *Science*, 327, 1103,
 1080 doi: [10.1126/science.1182787](https://doi.org/10.1126/science.1182787)
 1081 —. 2010g, *ApJL*, 709, L152,
 1082 doi: [10.1088/2041-8205/709/2/L152](https://doi.org/10.1088/2041-8205/709/2/L152)
 1083 —. 2010h, *A&A*, 524, A75,
 1084 doi: [10.1051/0004-6361/201014458](https://doi.org/10.1051/0004-6361/201014458)
 1085 —. 2010i, *ApJ*, 723, 649,
 1086 doi: [10.1088/0004-637X/723/1/649](https://doi.org/10.1088/0004-637X/723/1/649)
 1087 —. 2011, *ApJ*, 734, 116,
 1088 doi: [10.1088/0004-637X/734/2/116](https://doi.org/10.1088/0004-637X/734/2/116)
 1089 Abdo, A. A., Ajello, M., Allafort, A., et al. 2013,
 1090 *ApJS*, 208, 17,
 1091 doi: [10.1088/0067-0049/208/2/17](https://doi.org/10.1088/0067-0049/208/2/17)
 1092 Abramowski, A., Aharonian, F., Ait Benkhali, F.,
 1093 et al. 2015, *A&A*, 574, A27,
 1094 doi: [10.1051/0004-6361/201322694](https://doi.org/10.1051/0004-6361/201322694)
- 1095 Acero, F., Ackermann, M., Ajello, M., et al. 2015,
 1096 *ApJS*, 218, 23,
 1097 doi: [10.1088/0067-0049/218/2/23](https://doi.org/10.1088/0067-0049/218/2/23)
 1098 —. 2016a, *ApJS*, 223, 26,
 1099 doi: [10.3847/0067-0049/223/2/26](https://doi.org/10.3847/0067-0049/223/2/26)
 1100 —. 2016b, *ApJS*, 224, 8,
 1101 doi: [10.3847/0067-0049/224/1/8](https://doi.org/10.3847/0067-0049/224/1/8)
 1102 Acero, F., Donato, D., Ojha, R., et al. 2013, *ApJ*,
 1103 779, 133, doi: [10.1088/0004-637X/779/2/133](https://doi.org/10.1088/0004-637X/779/2/133)
 1104 Acero, F., Ackermann, M., Ajello, M., et al. 2016c,
 1105 *ApJS*, 224, 8, doi: [10.3847/0067-0049/224/1/8](https://doi.org/10.3847/0067-0049/224/1/8)
 1106 Ackermann, M., Ajello, M., Albert, A., et al.
 1107 2012a, *ApJS*, 203, 4,
 1108 doi: [10.1088/0067-0049/203/1/4](https://doi.org/10.1088/0067-0049/203/1/4)
 1109 —. 2016a, *PhRvD*, 93, 082001,
 1110 doi: [10.1103/PhysRevD.93.082001](https://doi.org/10.1103/PhysRevD.93.082001)
 1111 Ackermann, M., Ajello, M., Allafort, A., et al.
 1112 2011a, *Science*, 334, 1103
 1113 —. 2011b, *ApJ*, 743, 171,
 1114 doi: [10.1088/0004-637X/743/2/171](https://doi.org/10.1088/0004-637X/743/2/171)
 1115 —. 2012b, *Astroparticle Physics*, 35, 346,
 1116 doi: [10.1016/j.astropartphys.2011.10.007](https://doi.org/10.1016/j.astropartphys.2011.10.007)
 1117 —. 2013, *ApJS*, 209, 34,
 1118 doi: [10.1088/0067-0049/209/2/34](https://doi.org/10.1088/0067-0049/209/2/34)
 1119 Ackermann, M., Ajello, M., Atwood, W. B., et al.
 1120 2012c, *ApJ*, 750, 3,
 1121 doi: [10.1088/0004-637X/750/1/3](https://doi.org/10.1088/0004-637X/750/1/3)
 1122 —. 2015, *ApJ*, 810, 14,
 1123 doi: [10.1088/0004-637X/810/1/14](https://doi.org/10.1088/0004-637X/810/1/14)
 1124 —. 2016b, *ApJS*, 222, 5,
 1125 doi: [10.3847/0067-0049/222/1/5](https://doi.org/10.3847/0067-0049/222/1/5)
 1126 Ackermann, M., Ajello, M., Baldini, L., et al.
 1127 2011c, *ApJ*, 726, 35,
 1128 doi: [10.1088/0004-637X/726/1/35](https://doi.org/10.1088/0004-637X/726/1/35)
 1129 —. 2016c, *ApJ*, 826, 1,
 1130 doi: [10.3847/0004-637X/826/1/1](https://doi.org/10.3847/0004-637X/826/1/1)
 1131 —. 2017, *ApJ*, 843, 139,
 1132 doi: [10.3847/1538-4357/aa775a](https://doi.org/10.3847/1538-4357/aa775a)
 1133 —. 2018, *ApJS*, 237, 32,
 1134 doi: [10.3847/1538-4365/aacdf7](https://doi.org/10.3847/1538-4365/aacdf7)

¹⁹ <http://aladin.u-strasbg.fr/>

²⁰ <http://www.star.bristol.ac.uk/~mbt/topcat/>

²¹ <http://aplpy.github.com>

²² <http://healpix.jpl.nasa.gov/>

- 1135 Ackermann, M., Albert, A., Atwood, W. B., et al.
 1136 2016d, *A&A*, 586, A71,
 1137 doi: [10.1051/0004-6361/201526920](https://doi.org/10.1051/0004-6361/201526920)
- 1138 Ackermann, M., Ajello, M., Allafort, A., et al.
 1139 2012d, *ApJ*, 753, 83,
 1140 doi: [10.1088/0004-637X/753/1/83](https://doi.org/10.1088/0004-637X/753/1/83)
- 1141 Ackermann, M., Ajello, M., Atwood, W. B., et al.
 1142 2012e, *ApJ*, 761, 91,
 1143 doi: [10.1088/0004-637X/761/2/91](https://doi.org/10.1088/0004-637X/761/2/91)
- 1144 Aharonian, F., Akhperjanian, A. G., Aye, K.-M.,
 1145 et al. 2005, *A&A*, 439, 1013,
 1146 doi: [10.1051/0004-6361:20053195](https://doi.org/10.1051/0004-6361:20053195)
- 1147 Aharonian, F., Akhperjanian, A. G., Barres de
 1148 Almeida, U., et al. 2008, *A&A*, 477, 353,
 1149 doi: [10.1051/0004-6361:20078516](https://doi.org/10.1051/0004-6361:20078516)
- 1150 Ajello, M., Allafort, A., Baldini, L., et al. 2012,
 1151 *ApJ*, 744, 80, doi: [10.1088/0004-637X/744/1/80](https://doi.org/10.1088/0004-637X/744/1/80)
- 1152 Ajello, M., Atwood, W. B., Baldini, L., et al. 2017,
 1153 *ApJS*, 232, 18, doi: [10.3847/1538-4365/aa8221](https://doi.org/10.3847/1538-4365/aa8221)
- 1154 Ajello, M., Baldini, L., Barbiellini, G., et al. 2016,
 1155 *ApJ*, 819, 98, doi: [10.3847/0004-637X/819/2/98](https://doi.org/10.3847/0004-637X/819/2/98)
- 1156 Allafort, A., Baldini, L., Ballet, J., et al. 2013,
 1157 *ApJL*, 777, L2,
 1158 doi: [10.1088/2041-8205/777/1/L2](https://doi.org/10.1088/2041-8205/777/1/L2)
- 1159 Álvarez Crespo, N., Masetti, N., Ricci, F., et al.
 1160 2016a, *AJ*, 151, 32,
 1161 doi: [10.3847/0004-6256/151/2/32](https://doi.org/10.3847/0004-6256/151/2/32)
- 1162 Álvarez Crespo, N., Massaro, F., Milisavljevic, D.,
 1163 et al. 2016b, *AJ*, 151, 95,
 1164 doi: [10.3847/0004-6256/151/4/95](https://doi.org/10.3847/0004-6256/151/4/95)
- 1165 Álvarez Crespo, N., Massaro, F., D'Abrusco, R.,
 1166 et al. 2016c, *Ap&SS*, 361, 316,
 1167 doi: [10.1007/s10509-016-2902-1](https://doi.org/10.1007/s10509-016-2902-1)
- 1168 Araya, M. 2014, *MNRAS*, 444, 860,
 1169 doi: [10.1093/mnras/stu1484](https://doi.org/10.1093/mnras/stu1484)
- 1170 Araya, M. 2017, *ApJ*, 843, 12,
 1171 doi: [10.3847/1538-4357/aa7261](https://doi.org/10.3847/1538-4357/aa7261)
- 1172 Araya, M. 2018a, *MNRAS*, 474, 102,
 1173 doi: [10.1093/mnras/stx2779](https://doi.org/10.1093/mnras/stx2779)
- 1174 —. 2018b, *ApJ*, 859, 69,
 1175 doi: [10.3847/1538-4357/aabd7e](https://doi.org/10.3847/1538-4357/aabd7e)
- 1176 Arsioli, B., Fraga, B., Giommi, P., Padovani, P., &
 1177 Marrese, P. M. 2015, *A&A*, 579, A34,
 1178 doi: [10.1051/0004-6361/201424148](https://doi.org/10.1051/0004-6361/201424148)
- 1179 Arsioli, B., & Polenta, G. 2018, *A&A*, 616, A20,
 1180 doi: [10.1051/0004-6361/201832786](https://doi.org/10.1051/0004-6361/201832786)
- 1181 Atwood, W., Albert, A., Baldini, L., et al. 2013,
 1182 *ArXiv:1303.3514*.
 1183 <https://arxiv.org/abs/1303.3514>
- 1184 Atwood, W. B., Abdo, A. A., Ackermann, M.,
 1185 et al. 2009, *ApJ*, 697, 1071,
 1186 doi: [10.1088/0004-637X/697/2/1071](https://doi.org/10.1088/0004-637X/697/2/1071)
- 1187 Ballet, J., et al. 2015, in *ICRC*, Vol. 34, ICRC
 1188 2015, ed. A. S. Borisov et al., 848
- 1189 Baltz, E. A., Taylor, J. E., & Wai, L. L. 2007,
 1190 *ApJ*, 659, L125, doi: [10.1086/517882](https://doi.org/10.1086/517882)
- 1191 Bird, A. J., Bazzano, A., Malizia, A., et al. 2016,
 1192 *ApJS*, 223, 15,
 1193 doi: [10.3847/0067-0049/223/1/15](https://doi.org/10.3847/0067-0049/223/1/15)
- 1194 Bregeon, J., Charles, E., & Wood, M. 2013,
 1195 *ArXiv:1304.5456*.
 1196 <https://arxiv.org/abs/1304.5456>
- 1197 Bruel, P., Burnett, T. H., Digel, S. W., et al. 2018,
 1198 *arXiv:1810.11394*.
 1199 <https://arxiv.org/abs/1810.11394>
- 1200 Buehler, R., Scargle, J. D., Blandford, R. D.,
 1201 et al. 2012, *ApJ*, 749, 26,
 1202 doi: [10.1088/0004-637X/749/1/26](https://doi.org/10.1088/0004-637X/749/1/26)
- 1203 Bulgarelli, A., Fioretti, V., Parmiggiani, N., et al.
 1204 2019, *arXiv e-prints*, *arXiv:1903.06957*.
 1205 <https://arxiv.org/abs/1903.06957>
- 1206 Capetti, A., Massaro, F., & Baldi, R. D. 2017a,
 1207 *A&A*, 598, A49,
 1208 doi: [10.1051/0004-6361/201629287](https://doi.org/10.1051/0004-6361/201629287)
- 1209 —. 2017b, *A&A*, 601, A81,
 1210 doi: [10.1051/0004-6361/201630247](https://doi.org/10.1051/0004-6361/201630247)
- 1211 Caputo, R., Buckley, M. R., Martin, P., et al.
 1212 2016, *PhRvD*, 93, 062004,
 1213 doi: [10.1103/PhysRevD.93.062004](https://doi.org/10.1103/PhysRevD.93.062004)
- 1214 Casandjian, J.-M., & Grenier, I. A. 2008, *A&A*,
 1215 489, 849, doi: [10.1051/0004-6361:200809685](https://doi.org/10.1051/0004-6361:200809685)
- 1216 Chang, Y.-L., Arsioli, B., Giommi, P., &
 1217 Padovani, P. 2017, *A&A*, 598, A17,
 1218 doi: [10.1051/0004-6361/201629487](https://doi.org/10.1051/0004-6361/201629487)
- 1219 Chaty, S., Fortin, F., & Garcia, F. 2018, in
 1220 preparation
- 1221 Cheung, C. C., Donato, D., Gehrels, N.,
 1222 Sokolovsky, K. V., & Giroletti, M. 2012, *ApJ*,
 1223 756, 33, doi: [10.1088/0004-637X/756/1/33](https://doi.org/10.1088/0004-637X/756/1/33)
- 1224 Cheung, C. C., Jean, P., Shore, S. N., et al. 2016,
 1225 *ApJ*, 826, 142,
 1226 doi: [10.3847/0004-637X/826/2/142](https://doi.org/10.3847/0004-637X/826/2/142)
- 1227 Chiaro, G., Salvetti, D., La Mura, G., et al. 2016,
 1228 *MNRAS*, 462, 3180,
 1229 doi: [10.1093/mnras/stw1830](https://doi.org/10.1093/mnras/stw1830)
- 1230 Condon, J. J., Cotton, W. D., Greisen, E. W.,
 1231 et al. 1998, *AJ*, 115, 1693, doi: [10.1086/300337](https://doi.org/10.1086/300337)

- 1232 Cowperthwaite, P. S., Massaro, F., D'Abrusco, R.,
1233 et al. 2013, *AJ*, 146, 110,
1234 doi: [10.1088/0004-6256/146/5/110](https://doi.org/10.1088/0004-6256/146/5/110)
- 1235 D'Abrusco, R., Massaro, F., Paggi, A., et al. 2014,
1236 *ApJS*, 215, 14,
1237 doi: [10.1088/0067-0049/215/1/14](https://doi.org/10.1088/0067-0049/215/1/14)
- 1238 de Ruiter, H. R., Willis, A. G., & Arp, H. C. 1977,
1239 *A&AS*, 28, 211
- 1240 Devin, J., Acero, F., Ballet, J., & Schmid, J. 2018,
1241 *A&A*, 617, A5,
1242 doi: [10.1051/0004-6361/201833008](https://doi.org/10.1051/0004-6361/201833008)
- 1243 Doert, M., & Errando, M. 2014, *ApJ*, 782, 41,
1244 doi: [10.1088/0004-637X/782/1/41](https://doi.org/10.1088/0004-637X/782/1/41)
- 1245 Ferrand, G., & Safi-Harb, S. 2012, *Advances in*
1246 *Space Research*, 49, 1313,
1247 doi: [10.1016/j.asr.2012.02.004](https://doi.org/10.1016/j.asr.2012.02.004)
- 1248 Giommi, P., Polenta, G., Lähteenmäki, A., et al.
1249 2012, *A&A*, 541, A160,
1250 doi: [10.1051/0004-6361/201117825](https://doi.org/10.1051/0004-6361/201117825)
- 1251 Giroletti, M., Massaro, F., D'Abrusco, R., et al.
1252 2016, *A&A*, 588, A141,
1253 doi: [10.1051/0004-6361/201527817](https://doi.org/10.1051/0004-6361/201527817)
- 1254 Górski, K. M., Hivon, E., Banday, A. J., et al.
1255 2005, *ApJ*, 622, 759, doi: [10.1086/427976](https://doi.org/10.1086/427976)
- 1256 Green, D. A. 2014, *Bulletin of the Astronomical*
1257 *Society of India*, 42, 47,
1258 <https://arxiv.org/abs/1409.0637>
- 1259 Griffin, R. D., Dai, X., & Thompson, T. A. 2016,
1260 *ApJL*, 823, L17,
1261 doi: [10.3847/2041-8205/823/1/L17](https://doi.org/10.3847/2041-8205/823/1/L17)
- 1262 Grondin, M.-H., Funk, S., Lemoine-Goumard, M.,
1263 et al. 2011, *ApJ*, 738, 42,
1264 doi: [10.1088/0004-637X/738/1/42](https://doi.org/10.1088/0004-637X/738/1/42)
- 1265 H. E. S. S. Collaboration, Abdalla, H.,
1266 Abramowski, A., et al. 2018a, *A&A*, 612, A6,
1267 doi: [10.1051/0004-6361/201629790](https://doi.org/10.1051/0004-6361/201629790)
- 1268 —. 2018b, *A&A*, 619, A71,
1269 doi: [10.1051/0004-6361/201832640](https://doi.org/10.1051/0004-6361/201832640)
- 1270 Hanabata, Y., Katagiri, H., Hewitt, J. W., et al.
1271 2014, *ApJ*, 786, 145,
1272 doi: [10.1088/0004-637X/786/2/145](https://doi.org/10.1088/0004-637X/786/2/145)
- 1273 Harris, W. E. 1996, *AJ*, 112, 1487,
1274 doi: [10.1086/118116](https://doi.org/10.1086/118116)
- 1275 Hartman, R. C., Bertsch, D. L., Bloom, S. D.,
1276 et al. 1999, *ApJS*, 123, 79, doi: [10.1086/313231](https://doi.org/10.1086/313231)
- 1277 Hassan, T., Mirabal, N., Contreras, J. L., & Oya,
1278 I. 2013, *MNRAS*, 428, 220,
1279 doi: [10.1093/mnras/sts022](https://doi.org/10.1093/mnras/sts022)
- 1280 Hayashida, M., Stawarz, Ł., Cheung, C. C., et al.
1281 2013, *ApJ*, 779, 131,
1282 doi: [10.1088/0004-637X/779/2/131](https://doi.org/10.1088/0004-637X/779/2/131)
- 1283 Healey, S. E., Romani, R. W., Cotter, G., et al.
1284 2008, *ApJS*, 175, 97, doi: [10.1086/523302](https://doi.org/10.1086/523302)
- 1285 Healey, S. E., Romani, R. W., Taylor, G. B., et al.
1286 2007, *ApJS*, 171, 61, doi: [10.1086/513742](https://doi.org/10.1086/513742)
- 1287 HI4PI Collaboration, Ben Bekhti, N., Flöer, L.,
1288 et al. 2016, *A&A*, 594, A116,
1289 doi: [10.1051/0004-6361/201629178](https://doi.org/10.1051/0004-6361/201629178)
- 1290 Hovatta, T., Lister, M. L., Aller, M. F., et al.
1291 2012, *AJ*, 144, 105,
1292 doi: [10.1088/0004-6256/144/4/105](https://doi.org/10.1088/0004-6256/144/4/105)
- 1293 Hovatta, T., Aller, M. F., Aller, H. D., et al. 2014,
1294 *AJ*, 147, 143, doi: [10.1088/0004-6256/147/6/143](https://doi.org/10.1088/0004-6256/147/6/143)
- 1295 Hu, F., & Zidek, J. V. 2002, *Canad. J. Statist.*,
1296 30, 347
- 1297 Johannesson, G., Orlando, E., & the Fermi-LAT
1298 collaboration. 2013, *ArXiv:1307.0197*,
1299 <https://arxiv.org/abs/1307.0197>
- 1300 Johnson, T. J., Ray, P. S., Roy, J., et al. 2015,
1301 *ApJ*, 806, 91, doi: [10.1088/0004-637X/806/1/91](https://doi.org/10.1088/0004-637X/806/1/91)
- 1302 Katagiri, H., Tibaldo, L., Ballet, J., et al. 2011,
1303 *ApJ*, 741, 44, doi: [10.1088/0004-637X/741/1/44](https://doi.org/10.1088/0004-637X/741/1/44)
- 1304 Katagiri, H., Yoshida, K., Ballet, J., et al. 2016a,
1305 *ApJ*, 818, 114,
1306 doi: [10.3847/0004-637X/818/2/114](https://doi.org/10.3847/0004-637X/818/2/114)
- 1307 Katagiri, H., Sugiyama, S., Ackermann, M., et al.
1308 2016b, *ApJ*, 831, 106,
1309 doi: [10.3847/0004-637X/831/1/106](https://doi.org/10.3847/0004-637X/831/1/106)
- 1310 Kataoka, J., Yatsu, Y., Kawai, N., et al. 2012,
1311 *ApJ*, 757, 176,
1312 doi: [10.1088/0004-637X/757/2/176](https://doi.org/10.1088/0004-637X/757/2/176)
- 1313 Katsuta, J., Uchiyama, Y., Tanaka, T., et al.
1314 2012, *ApJ*, 752, 135,
1315 doi: [10.1088/0004-637X/752/2/135](https://doi.org/10.1088/0004-637X/752/2/135)
- 1316 Kerr, M. 2010, PhD thesis, University of
1317 Washington, *ArXiv:1101.6072*,
1318 <https://arxiv.org/abs/1101.6072>
- 1319 Kovalev, Y. Y. 2009, *ApJ*, 707, L56,
1320 doi: [10.1088/0004-637X/707/1/L56](https://doi.org/10.1088/0004-637X/707/1/L56)
- 1321 Kuźmicz, A., Jamrozy, M., Bronarska, K.,
1322 Janda-Boczar, K., & Saikia, D. J. 2018, *ApJS*,
1323 238, 9, doi: [10.3847/1538-4365/aad9ff](https://doi.org/10.3847/1538-4365/aad9ff)
- 1324 Lande, J., Ackermann, M., Allafort, A., et al.
1325 2012, *ApJ*, 756, 5,
1326 doi: [10.1088/0004-637X/756/1/5](https://doi.org/10.1088/0004-637X/756/1/5)
- 1327 Landi, R., Bassani, L., Stephen, J. B., et al. 2015,
1328 *A&A*, 581, A57,
1329 doi: [10.1051/0004-6361/201526221](https://doi.org/10.1051/0004-6361/201526221)

- 1330 Landoni, M., Falomo, R., Treves, A., Scarpa, R.,
 1331 & Reverte Payá, D. 2015a, *AJ*, 150, 181,
 1332 doi: [10.1088/0004-6256/150/6/181](https://doi.org/10.1088/0004-6256/150/6/181)
- 1333 Landoni, M., Paiano, S., Falomo, R., Scarpa, R.,
 1334 & Treves, A. 2018, *ApJ*, 861, 130,
 1335 doi: [10.3847/1538-4357/aac77c](https://doi.org/10.3847/1538-4357/aac77c)
- 1336 Landoni, M., Massaro, F., Paggi, A., et al. 2015b,
 1337 *AJ*, 149, 163, doi: [10.1088/0004-6256/149/5/163](https://doi.org/10.1088/0004-6256/149/5/163)
- 1338 Li, J., Rea, N., Torres, D. F., & de Oña-Wilhelmi,
 1339 E. 2017a, *ApJ*, 835, 30,
 1340 doi: [10.3847/1538-4357/835/1/30](https://doi.org/10.3847/1538-4357/835/1/30)
- 1341 Li, J., Torres, D. F., Cheng, K. S., et al. 2017b,
 1342 *ApJ*, 846, 169, doi: [10.3847/1538-4357/aa7ff7](https://doi.org/10.3847/1538-4357/aa7ff7)
- 1343 Liu, Q. Z., van Paradijs, J., & van den Heuvel,
 1344 E. P. J. 2007, *VizieR Online Data Catalog*, 346,
 1345 90807
- 1346 López-Cañiego, M., González-Nuevo, J., Massardi,
 1347 M., et al. 2013, *MNRAS*, 430, 1566,
 1348 doi: [10.1093/mnras/sts680](https://doi.org/10.1093/mnras/sts680)
- 1349 Maeda, K., Kataoka, J., Nakamori, T., et al. 2011,
 1350 *ApJ*, 729, 103,
 1351 doi: [10.1088/0004-637X/729/2/103](https://doi.org/10.1088/0004-637X/729/2/103)
- 1352 Manchester, R. N., Hobbs, G. B., Teoh, A., &
 1353 Hobbs, M. 2005, *AJ*, 129, 1993,
 1354 doi: [10.1086/428488](https://doi.org/10.1086/428488)
- 1355 Marchesi, S., Kaur, A., & Ajello, M. 2018, *AJ*,
 1356 156, 212, doi: [10.3847/1538-3881/aae201](https://doi.org/10.3847/1538-3881/aae201)
- 1357 Marchesini, E. J., Peña-Herazo, H. A., Álvarez
 1358 Crespo, N., et al. 2019, *Ap&SS*, 364, 5,
 1359 doi: [10.1007/s10509-018-3490-z](https://doi.org/10.1007/s10509-018-3490-z)
- 1360 Maselli, A., Massaro, F., D'Abrusco, R., et al.
 1361 2015, *Ap&SS*, 357, 141,
 1362 doi: [10.1007/s10509-015-2372-x](https://doi.org/10.1007/s10509-015-2372-x)
- 1363 Massaro, E., Giommi, P., Leto, C., et al. 2009,
 1364 *A&A*, 495, 691,
 1365 doi: [10.1051/0004-6361:200810161](https://doi.org/10.1051/0004-6361:200810161)
- 1366 Massaro, F., & D'Abrusco, R. 2016, *ApJ*, 827, 67,
 1367 doi: [10.3847/0004-637X/827/1/67](https://doi.org/10.3847/0004-637X/827/1/67)
- 1368 Massaro, F., D'Abrusco, R., Ajello, M., Grindlay,
 1369 J. E., & Smith, H. A. 2011, *ApJ*, 740, L48,
 1370 doi: [10.1088/2041-8205/740/2/L48](https://doi.org/10.1088/2041-8205/740/2/L48)
- 1371 Massaro, F., D'Abrusco, R., Giroletti, M., et al.
 1372 2013, *ApJS*, 207, 4,
 1373 doi: [10.1088/0067-0049/207/1/4](https://doi.org/10.1088/0067-0049/207/1/4)
- 1374 Massaro, F., D'Abrusco, R., Tosti, G., et al.
 1375 2012a, *ApJ*, 750, 138,
 1376 doi: [10.1088/0004-637X/750/2/138](https://doi.org/10.1088/0004-637X/750/2/138)
- 1377 —. 2012b, *ApJ*, 752, 61,
 1378 doi: [10.1088/0004-637X/752/1/61](https://doi.org/10.1088/0004-637X/752/1/61)
- 1379 Massaro, F., Landoni, M., D'Abrusco, R., et al.
 1380 2015a, *A&A*, 575, A124,
 1381 doi: [10.1051/0004-6361/201425119](https://doi.org/10.1051/0004-6361/201425119)
- 1382 Massaro, F., Masetti, N., D'Abrusco, R., Paggi,
 1383 A., & Funk, S. 2014, *AJ*, 148, 66,
 1384 doi: [10.1088/0004-6256/148/4/66](https://doi.org/10.1088/0004-6256/148/4/66)
- 1385 Massaro, F., D'Abrusco, R., Landoni, M., et al.
 1386 2015b, *ApJS*, 217, 2,
 1387 doi: [10.1088/0067-0049/217/1/2](https://doi.org/10.1088/0067-0049/217/1/2)
- 1388 Massaro, F., Álvarez Crespo, N., D'Abrusco, R.,
 1389 et al. 2016, *Ap&SS*, 361, 337,
 1390 doi: [10.1007/s10509-016-2926-6](https://doi.org/10.1007/s10509-016-2926-6)
- 1391 Mattox, J. R., Bertsch, D. L., Chiang, J., et al.
 1392 1996, *ApJ*, 461, 396, doi: [10.1086/177068](https://doi.org/10.1086/177068)
- 1393 Mattox, J. R., Wagner, S. J., Malkan, M., et al.
 1394 1997, *ApJ*, 476, 692, doi: [10.1086/303639](https://doi.org/10.1086/303639)
- 1395 Mauch, T., Murphy, T., Buttery, H. J., et al.
 1396 2003, *MNRAS*, 342, 1117,
 1397 doi: [10.1046/j.1365-8711.2003.06605.x](https://doi.org/10.1046/j.1365-8711.2003.06605.x)
- 1398 McConnachie, A. W. 2012, *AJ*, 144, 4,
 1399 doi: [10.1088/0004-6256/144/1/4](https://doi.org/10.1088/0004-6256/144/1/4)
- 1400 Mereghetti, S., Palombara, N. L., Tiengo, A.,
 1401 et al. 2011, *ApJ*, 737, 51,
 1402 doi: [10.1088/0004-637x/737/2/51](https://doi.org/10.1088/0004-637x/737/2/51)
- 1403 Mirabal, N., & Halpern, J. P. 2009, *ApJ*, 701,
 1404 L129, doi: [10.1088/0004-637X/701/2/L129](https://doi.org/10.1088/0004-637X/701/2/L129)
- 1405 Murphy, T., Sadler, E. M., Ekers, R. D., et al.
 1406 2010, *MNRAS*, 402, 2403,
 1407 doi: [10.1111/j.1365-2966.2009.15961.x](https://doi.org/10.1111/j.1365-2966.2009.15961.x)
- 1408 Napier, P. J., Bagri, D. S., Clark, B. G., et al.
 1409 1994, *IEEE Proceedings*, 82, 658
- 1410 Nolan, P. L., Abdo, A. A., Ackermann, M., et al.
 1411 2012, *ApJS*, 199, 31,
 1412 doi: [10.1088/0067-0049/199/2/31](https://doi.org/10.1088/0067-0049/199/2/31)
- 1413 Nori, M., Giroletti, M., Massaro, F., et al. 2014,
 1414 *ApJS*, 212, 3, doi: [10.1088/0067-0049/212/1/3](https://doi.org/10.1088/0067-0049/212/1/3)
- 1415 Oh, K., Koss, M., Markwardt, C. B., et al. 2018,
 1416 *ApJS*, 235, 4, doi: [10.3847/1538-4365/aaa7fd](https://doi.org/10.3847/1538-4365/aaa7fd)
- 1417 Paggi, A., Massaro, F., D'Abrusco, R., et al. 2013,
 1418 *ApJS*, 209, 9, doi: [10.1088/0067-0049/209/1/9](https://doi.org/10.1088/0067-0049/209/1/9)
- 1419 Paggi, A., Milisavljevic, D., Masetti, N., et al.
 1420 2014, *AJ*, 147, 112,
 1421 doi: [10.1088/0004-6256/147/5/112](https://doi.org/10.1088/0004-6256/147/5/112)
- 1422 Paiano, S., Falomo, R., Franceschini, A., Treves,
 1423 A., & Scarpa, R. 2017a, *ApJ*, 851, 135,
 1424 doi: [10.3847/1538-4357/aa9af4](https://doi.org/10.3847/1538-4357/aa9af4)
- 1425 Paiano, S., Franceschini, A., & Stamerra, A.
 1426 2017b, *MNRAS*, 468, 4902,
 1427 doi: [10.1093/mnras/stx749](https://doi.org/10.1093/mnras/stx749)

- 1428 Paiano, S., Landoni, M., Falomo, R., Treves, A.,
1429 & Scarpa, R. 2017c, *ApJ*, 844, 120,
1430 doi: [10.3847/1538-4357/aa7aac](https://doi.org/10.3847/1538-4357/aa7aac)
- 1431 Paiano, S., Landoni, M., Falomo, R., et al. 2017d,
1432 *ApJ*, 837, 144,
1433 doi: [10.3847/1538-4357/837/2/144](https://doi.org/10.3847/1538-4357/837/2/144)
- 1434 Peña-Herazo, H. A., Marchesini, E. J., Álvarez
1435 Crespo, N., et al. 2017, *Ap&SS*, 362, 228,
1436 doi: [10.1007/s10509-017-3208-7](https://doi.org/10.1007/s10509-017-3208-7)
- 1437 Peng, F.-K., Wang, X.-Y., Liu, R.-Y., Tang,
1438 Q.-W., & Wang, J.-F. 2016, *ApJL*, 821, L20,
1439 doi: [10.3847/2041-8205/821/2/L20](https://doi.org/10.3847/2041-8205/821/2/L20)
- 1440 Petrov, L., Mahony, E. K., Edwards, P. G., et al.
1441 2013, *MNRAS*, 432, 1294,
1442 doi: [10.1093/mnras/stt550](https://doi.org/10.1093/mnras/stt550)
- 1443 Petrov, L., Phillips, C., Bertarini, A., Murphy, T.,
1444 & Sadler, E. M. 2011, *MNRAS*, 414, 2528,
1445 doi: [10.1111/j.1365-2966.2011.18570.x](https://doi.org/10.1111/j.1365-2966.2011.18570.x)
- 1446 Pivato, G., Hewitt, J. W., Tibaldo, L., et al. 2013,
1447 *ApJ*, 779, 179,
1448 doi: [10.1088/0004-637X/779/2/179](https://doi.org/10.1088/0004-637X/779/2/179)
- 1449 Planck Collaboration, Aghanim, N., Ashdown, M.,
1450 et al. 2016, *A&A*, 596, A109,
1451 doi: [10.1051/0004-6361/201629022](https://doi.org/10.1051/0004-6361/201629022)
- 1452 Popov, S. B., Mereghetti, S., Blinnikov, S. I.,
1453 Kuranov, A. G., & Yungelson, L. R. 2018,
1454 *MNRAS*, 474, 2750, doi: [10.1093/mnras/stx2910](https://doi.org/10.1093/mnras/stx2910)
- 1455 Porter, T. A., Jóhannesson, G., & Moskalenko,
1456 I. V. 2017, *ApJ*, 846, 67,
1457 doi: [10.3847/1538-4357/aa844d](https://doi.org/10.3847/1538-4357/aa844d)
- 1458 Principe, G., Malyshev, D., Ballet, J., & Funk, S.
1459 2018, *A&A*, 618, A22,
1460 doi: [10.1051/0004-6361/201833116](https://doi.org/10.1051/0004-6361/201833116)
- 1461 Rakshit, S., Stalin, C. S., Chand, H., & Zhang,
1462 X.-G. 2017, *ApJS*, 229, 39,
1463 doi: [10.3847/1538-4365/aa6971](https://doi.org/10.3847/1538-4365/aa6971)
- 1464 Ricci, F., Massaro, F., Landoni, M., et al. 2015,
1465 *AJ*, 149, 160, doi: [10.1088/0004-6256/149/5/160](https://doi.org/10.1088/0004-6256/149/5/160)
- 1466 Sanders, D. B., Mazzarella, J. M., Kim, D.-C.,
1467 Surace, J. A., & Soifer, B. T. 2003, *AJ*, 126,
1468 1607, doi: [10.1086/376841](https://doi.org/10.1086/376841)
- 1469 Schinzel, F. K., Petrov, L., Taylor, G. B., &
1470 Edwards, P. G. 2017, *ApJ*, 838, 139,
1471 doi: [10.3847/1538-4357/aa6439](https://doi.org/10.3847/1538-4357/aa6439)
- 1472 Schinzel, F. K., Petrov, L., Taylor, G. B., et al.
1473 2015, *ApJS*, 217, 4,
1474 doi: [10.1088/0067-0049/217/1/4](https://doi.org/10.1088/0067-0049/217/1/4)
- 1475 Schmidt, K., Priebe, A., & Boller, T. 1993,
1476 *Astronomische Nachrichten*, 314, 371
- 1477 Shahbaz, T., & Watson, C. A. 2007, *A&A*, 474,
1478 969, doi: [10.1051/0004-6361:20078251](https://doi.org/10.1051/0004-6361:20078251)
- 1479 Shaw, M. S., Filippenko, A. V., Romani, R. W.,
1480 Cenko, S. B., & Li, W. 2013a, *AJ*, 146, 127,
1481 doi: [10.1088/0004-6256/146/5/127](https://doi.org/10.1088/0004-6256/146/5/127)
- 1482 Shaw, M. S., Romani, R. W., Cotter, G., et al.
1483 2013b, *ApJ*, 764, 135,
1484 doi: [10.1088/0004-637X/764/2/135](https://doi.org/10.1088/0004-637X/764/2/135)
- 1485 Smith, D. A., Bruel, P., Cognard, I., et al. 2019,
1486 *ApJ*, 871, 78, doi: [10.3847/1538-4357/aaf57d](https://doi.org/10.3847/1538-4357/aaf57d)
- 1487 Stappers, B. W., Archibald, A. M., Hessels,
1488 J. W. T., et al. 2014, *ApJ*, 790, 39,
1489 doi: [10.1088/0004-637X/790/1/39](https://doi.org/10.1088/0004-637X/790/1/39)
- 1490 Stroh, M. C., & Falcone, A. D. 2013, *ApJS*, 207,
1491 28, doi: [10.1088/0067-0049/207/2/28](https://doi.org/10.1088/0067-0049/207/2/28)
- 1492 Takahashi, Y., Kataoka, J., Nakamori, T., et al.
1493 2012, *ApJ*, 747, 64,
1494 doi: [10.1088/0004-637X/747/1/64](https://doi.org/10.1088/0004-637X/747/1/64)
- 1495 Takeuchi, Y., Kataoka, J., Maeda, K., et al. 2013,
1496 *ApJS*, 208, 25,
1497 doi: [10.1088/0067-0049/208/2/25](https://doi.org/10.1088/0067-0049/208/2/25)
- 1498 Tang, Q.-W., Wang, X.-Y., & Tam, P.-H. T. 2014,
1499 *ApJ*, 794, 26, doi: [10.1088/0004-637X/794/1/26](https://doi.org/10.1088/0004-637X/794/1/26)
- 1500 Véron-Cetty, M.-P., & Véron, P. 2010, *A&A*, 518,
1501 A10, doi: [10.1051/0004-6361/201014188](https://doi.org/10.1051/0004-6361/201014188)
- 1502 Voges, W., Aschenbach, B., Boller, T., et al. 1999,
1503 *A&A*, 349, 389
- 1504 —. 2000, *VizieR Online Data Catalog*, 9029
- 1505 Yeung, P. K. H., Kong, A. K. H., Tam, P. H. T.,
1506 et al. 2017, *ApJ*, 837, 69,
1507 doi: [10.3847/1538-4357/aa5df1](https://doi.org/10.3847/1538-4357/aa5df1)
- 1508 —. 2016, *ApJ*, 827, 41,
1509 doi: [10.3847/0004-637X/827/1/41](https://doi.org/10.3847/0004-637X/827/1/41)
- 1510 Yoast-Hull, T. M., Gallagher, John S., I., Aalto,
1511 S., & Varenus, E. 2017, *MNRAS*, 469, L89,
1512 doi: [10.1093/mnras/slx054](https://doi.org/10.1093/mnras/slx054)
- 1513 Zanin, R., Fernández-Barral, A., de Oña
1514 Wilhelmi, E., et al. 2016, *A&A*, 596, A55,
1515 doi: [10.1051/0004-6361/201628917](https://doi.org/10.1051/0004-6361/201628917)
- 1516 Zdziarski, A. A., Malyshev, D., Chernyakova, M.,
1517 & Pooley, G. G. 2017, *MNRAS*, 471, 3657,
1518 doi: [10.1093/mnras/stx1846](https://doi.org/10.1093/mnras/stx1846)
- 1519 Zhang, P. F., Xin, Y. L., Fu, L., et al. 2016,
1520 *MNRAS*, 459, 99, doi: [10.1093/mnras/stw567](https://doi.org/10.1093/mnras/stw567)

APPENDIX

A. DESCRIPTION OF THE FITS VERSION OF THE 4FGL CATALOG

Table 9. LAT 4FGL FITS Format: LAT_Point_Source_Catalog Extension

Column	Format	Unit	Description
Source_Name	18A	...	Source name 4FGL JHHMM.m+DDMMa ^a
RAJ2000	E	deg	Right Ascension
DEJ2000	E	deg	Declination
GLON	E	deg	Galactic Longitude
GLAT	E	deg	Galactic Latitude
Conf_68_SemiMajor	E	deg	Long radius of error ellipse at 68% confidence ^b
Conf_68_SemiMinor	E	deg	Short radius of error ellipse at 68% confidence ^b
Conf_68_PosAng	E	deg	Position angle of the 68% ellipse ^b
Conf_95_SemiMajor	E	deg	Long radius of error ellipse at 95% confidence
Conf_95_SemiMinor	E	deg	Short radius of error ellipse at 95% confidence
Conf_95_PosAng	E	deg	Position angle (eastward) of the long axis from celestial North
ROI_num	I	...	ROI number (cross-reference to ROIs extension)
Extended_Source_Name	18A	...	Cross-reference to the ExtendedSources extension
Signif_Avg	E	...	Source significance in σ units over the 100 MeV to 1 TeV band
Pivot_Energy	E	MeV	Energy at which error on differential flux is minimal
Flux1000	E	cm ⁻² s ⁻¹	Integral photon flux from 1 to 100 GeV
Unc_Flux1000	E	cm ⁻² s ⁻¹	1 σ error on integral photon flux from 1 to 100 GeV
Energy_Flux100	E	erg cm ⁻² s ⁻¹	Energy flux from 100 MeV to 100 GeV obtained by spectral fitting
Unc_Energy_Flux100	E	erg cm ⁻² s ⁻¹	1 σ error on energy flux from 100 MeV to 100 GeV
SpectrumType	18A	...	Spectral type in the global model (PowerLaw, LogParabola, PLSuperExpCutoff)
PL_Flux_Density	E	cm ⁻² MeV ⁻¹ s ⁻¹	Differential flux at Pivot_Energy in PowerLaw fit
Unc_PL_Flux_Density	E	cm ⁻² MeV ⁻¹ s ⁻¹	1 σ error on PL_Flux_Density
PL_Index	E	...	Photon index when fitting with PowerLaw
Unc_PL_Index	E	...	1 σ error on PL_Index
LP_Flux_Density	E	cm ⁻² MeV ⁻¹ s ⁻¹	Differential flux at Pivot_Energy in LogParabola fit
Unc_LP_Flux_Density	E	cm ⁻² MeV ⁻¹ s ⁻¹	1 σ error on LP_Flux_Density
LP_Index	E	...	Photon index at Pivot_Energy (α of Eq. 2) when fitting with LogParabola
Unc_LP_Index	E	...	1 σ error on LP_Index
LP_beta	E	...	Curvature parameter (β of Eq. 2) when fitting with LogParabola
Unc_LP_beta	E	...	1 σ error on LP_beta
LP_SigCurv	E	...	Significance (in σ units) of the fit improvement between PowerLaw and LogParabola. A value greater than 4 indicates significant curvature
PLEC_Flux_Density	E	cm ⁻² MeV ⁻¹ s ⁻¹	Differential flux at Pivot_Energy in PLSuperExpCutoff fit
Unc_PLEC_Flux_Density	E	cm ⁻² MeV ⁻¹ s ⁻¹	1 σ error on PLEC_Flux_Density
PLEC_Index	E	...	Low-energy photon index (Γ of Eq. 3) when fitting with PLSuperExpCutoff
Unc_PLEC_Index	E	...	1 σ error on PLEC_Index
PLEC_Expfactor	E	...	Exponential factor (a of Eq. 3) when fitting with PLSuperExpCutoff
Unc_PLEC_Expfactor	E	...	1 σ error on PLEC_Expfactor
PLEC_Exp_Index	E	...	Exponential index (b of Eq. 3) when fitting with PLSuperExpCutoff
Unc_PLEC_Exp_Index	E	...	1 σ error on PLEC_Exp_Index
PLEC_SigCurv	E	...	Same as LP_SigCurv for PLSuperExpCutoff model
Npred	E	...	Predicted number of events in the model

Table 9 continued on next page

Table 9 (continued)

Column	Format	Unit	Description
Flux_Band	7E	cm ⁻² s ⁻¹	Integral photon flux in each spectral band
Unc_Flux_Band	2 × 7E	cm ⁻² s ⁻¹	1σ lower and upper error on Flux_Band ^c
nuFnu	7E	erg cm ⁻² s ⁻¹	Spectral energy distribution over each spectral band
Sqrt_TS_Band	7E	...	Square root of the Test Statistic in each spectral band
Variability_Index	E	...	Sum of 2×log(Likelihood) difference between the flux fitted in each time interval and the average flux over the full catalog interval; a value greater than 18.48 over 12 intervals indicates <1% chance of being a steady source
Frac_Variability	E	...	Fractional variability computed from the fluxes in each year
Unc_Frac_Variability	E	...	1σ error on fractional variability
Signif_Peak	E	...	Source significance in peak interval in σ units
Flux_Peak	E	cm ⁻² s ⁻¹	Peak integral photon flux from 100 MeV to 100 GeV
Unc_Flux_Peak	E	cm ⁻² s ⁻¹	1σ error on peak integral photon flux
Time_Peak	D	s (MET)	Time of center of interval in which peak flux was measured
Peak_Interval	E	s	Length of interval in which peak flux was measured
Flux_History	12E	cm ⁻² s ⁻¹	Integral photon flux from 100 MeV to 100 GeV in each year (best fit from likelihood analysis with spectral shape fixed to that obtained over full interval)
Unc_Flux_History	2 × 12E	cm ⁻² s ⁻¹	1σ lower and upper error on integral photon flux in each year ^c
Sqrt_TS_History	12E	...	Square root of the Test Statistic in each year
ASSOC_FGL	18A	...	Most recent correspondence to previous FGL source catalogs, if any
ASSOC_FHL	18A	...	Most recent correspondence to previous FHL source catalogs, if any
ASSOC_GAM1	18A	...	Name of likely corresponding 2AGL source, if any
ASSOC_GAM2	18A	...	Name of likely corresponding 3EG source, if any
ASSOC_GAM3	18A	...	Name of likely corresponding EGR source, if any
TEVCAT_FLAG	A	...	P if positional association with non-extended source in TeVCat E if associated with an extended source in TeVCat, N if no TeV association
ASSOC_TEV	24A	...	Name of likely corresponding TeV source from TeVCat, if any
CLASS1	5A	...	Class designation for associated source; see Table 7
CLASS2	5A	...	Class designation for low-confidence association
ASSOC1	28A	...	Name of identified or likely associated source
ASSOC2	26A	...	Name of low-confidence association or of enclosing extended source
ASSOC_PROB_BAY	E	...	Probability of association according to the Bayesian method ^d
ASSOC_PROB_LR	E	...	Probability of association according to the Likelihood Ratio method ^e
RA_Counterpart	D	deg	Right Ascension of the counterpart ASSOC1
DEC_Counterpart	D	deg	Declination of the counterpart ASSOC1
Unc_Counterpart	E	deg	95% precision of the counterpart localization ^f
Flags	I	...	Source flags (binary coding as in Table 5) ^g

^aThe letter at the end can be **e** (extended source), **i** (for Crab nebula inverse Compton) or **s** (for Crab nebula synchrotron).

^bfrom the 95% ellipse, assuming a Gaussian distribution.

^cSeparate 1σ errors are computed from the likelihood profile toward lower and larger fluxes. The lower error is set equal to NULL and the upper error is derived from a Bayesian upper limit if the 1σ interval contains 0 ($TS < 1$).

^dNaN in this column when ASSOC1 is defined means that the probability could not be computed, either because the source is extended or because the counterpart is the result of dedicated follow-up.

^eProbabilities < 0.8 are formally set to 0.

^fFor extended counterparts, this reports their extension radius.

^gEach condition is indicated by one bit among the 16 bits forming **Flags**. The bit is raised (set to 1) in the dubious case, so that sources without any warning sign have **Flags** = 0.

Table 10. LAT 4FGL FITS Format: Components Extension

Column	Format	Unit	Description
Emin	E	MeV	Lower bound of component's energy interval
Emax	E	MeV	Upper bound of component's energy interval
ENumBins	I	...	Number of bins inside energy interval
EvType	I	...	Event type selection for this component
ZenithCut	E	deg	Maximum zenith angle for this component
RingWidth	E	deg	Difference between RoI radius and core radius
PixelSize	E	deg	Pixel size for this component (of exposure map in unbinned mode)
BinnedMode	I	...	0=Unbinned, 1=Binned
Weighted	I	...	1 if weights were applied to this component

1523 The FITS format version of the second release of the 4FGL catalog has seven binary table extensions.
 1524 The extension `LAT_Point_Source_Catalog_Extension` has all of the information about the sources.
 1525 Its format is described in Table 9.

1526 The extension `GTI` is a standard Good-Time Interval listing the precise time intervals (start and
 1527 stop in Mission Elapsed Time) included in the data analysis. The number of intervals is fairly large
 1528 because on most orbits (~ 95 min) *Fermi* passes through the South Atlantic Anomaly (SAA), and
 1529 science data taking is stopped during these times. In addition, data taking is briefly interrupted
 1530 on each non-SAA-crossing orbit, as *Fermi* crosses the ascending node. Filtering of time intervals
 1531 with large rocking angles, gamma-ray bursts, solar flares, data gaps, or operation in non-standard
 1532 configurations introduces some more entries. The GTI is provided for reference and would be useful,
 1533 e.g., for reconstructing the precise data set that was used for the analysis.

1534 The extension `ExtendedSources` (format unchanged since 2FGL) contains information about the
 1535 75 spatially extended sources that are modeled in the 4FGL source list (§ 3.4), including locations
 1536 and shapes. The extended sources are indicated by an e appended to their names in the main table.

1537 The extension `ROIs` contains information about the 1748 RoIs over which the analysis ran. In
 1538 particular it reports the best-fit diffuse parameters. Its format is very close to that in 3FGL, with
 1539 one exception. The `RADIUS` column is replaced by `CoreRadius` which reports the radius of the RoI
 1540 core (in which the sources which belong to the RoI are located). The RoI radius (half-width in binned
 1541 mode) depends on the component, and is given by the core radius plus `RingWidth`, where the latter
 1542 is given in the `Components` extension.

1543 The extension `Components` is new to 4FGL. It reports the settings of each individual component
 1544 (15 in all) whose sum forms the entire data set for the SummedLikelihood approach, as described in
 1545 Table 2. Its format is given by Table 10.

1546 The extension `EnergyBounds` is new to 4FGL. It contains the definitions of the bands in which
 1547 the fluxes reported in the `xx_Band` columns of the main extension were computed, and the settings
 1548 of the analysis. Its format is the same as that of the `Components` extension, plus one more column
 1549 (`SysRel`) reporting the systematic uncertainty on effective area used to flag the sources with Flag
 1550 10 (Table 5). When several components were used in one band, several lines appear with the same
 1551 `LowerEnergy` and `UpperEnergy`.

1552 The extension `Hist_Start` (format unchanged since 1FGL) contains the definitions of the time
 1553 intervals used to build the light curves.

B. WEIGHTED LOG-LIKELIHOOD

1554
 1555 In 3FGL we introduced a first attempt at accounting for systematic errors in the maximum
 1556 likelihood process itself, at the source detection level. It was not used in the source characterization,
 1557 however, for lack of a suitable framework. The standard way to account for systematic errors (for
 1558 example in *XSPEC*²³) is to define them as a fraction ϵ of the signal and add them to the statistical
 1559 errors in quadrature, in a χ^2 formalism. This can be adapted to the maximum likelihood framework
 1560 by introducing weights $w_i < 1$ (Hu & Zidek 2002) as

$$\log \mathcal{L} = \sum_i w_i (n_i \log M_i - M_i) \quad (\text{B1})$$

1561 where M_i and n_i are the model and observed counts in each bin, and the sum runs over all bins
 1562 in space and energy. The source significance can then be quantified in the same way, via the Test
 1563 Statistic $TS = 2 \log(\mathcal{L}/\mathcal{L}_0)$ in which \mathcal{L} and \mathcal{L}_0 are the (weighted) likelihood with and without the
 1564 source of interest, respectively.

1565 Since the statistical variance in Poisson statistics is the signal itself, a first guess for the weights
 1566 could be

$$w_i = \frac{M_i}{M_i + (\epsilon M_i)^2} = \frac{1}{1 + \epsilon^2 M_i} \quad (\text{B2})$$

1567 However, that formulation has a serious flaw, which is that it is not stable to rebinning. If one splits
 1568 the bins in half, then M_i is split in half while ϵ stays the same (it is defined externally). In the limit
 1569 of very small bins, obviously the weights will all tend to 1 and the $\log \mathcal{L}$ formula will tend to the
 1570 unweighted one, even though nothing has changed in the underlying data or the model.

1571 The solution we propose, originally presented in Ballet et al. (2015), is to define a suitable integral
 1572 over energy (E) and space (\mathbf{r}) $N(\mathbf{r}, E)$ which does not depend on binning. M_i in the weight formula
 1573 is then replaced by $N(\mathbf{r}_i, E_i)$ taken at the event's coordinates. For the integral over space, since the
 1574 catalog mostly deals with point sources, the logical solution is to integrate the background under the
 1575 PSF, i.e., convolve the model with the PSF $P(\mathbf{r}, E)$, normalized to 1 at the peak (this is equivalent,
 1576 for a flat diffuse emission, to multiplying by the PSF solid angle). Note that the model already
 1577 contains the PSF, so this amounts to applying a double convolution to the sky model.

1578 For the energy integral the choice is less obvious. The source spectrum is not a narrow line, so
 1579 convolving with the energy dispersion (similar to what is done for space) is not justified. An integral
 1580 over the full energy range would give the same weight to all energies, which is clearly not what we
 1581 want (there is no reason to downplay the few high-energy events). The option we adopt here is to
 1582 start the integration at the current energy.

$$w_i = \frac{1}{1 + \epsilon^2 N(\mathbf{r}_i, E_i)} \quad (\text{B3})$$

$$N(\mathbf{r}_i, E_i) = \int_{E_i}^{E_{\max}} S(\mathbf{r}_i, E) dE \quad (\text{B4})$$

$$S(\mathbf{r}, E) = \frac{dM}{dE}(\mathbf{r}, E) * P(\mathbf{r}, E) \quad (\text{B5})$$

²³ <https://heasarc.gsfc.nasa.gov/xanadu/xspec/>

1583 where dM/dE is the differential model. As energy increases, the spectra (in counts) decrease and
 1584 the LAT PSF gets narrower so the convolution makes S even steeper than dM/dE . As a result, the
 1585 integral giving N is nearly always dominated by the lowest energies, so the exact upper bound E_{\max}
 1586 is not critical. The only spectral region where it is important is the very lowest energies (< 100 MeV)
 1587 where the effective area rises steeply. In order not to penalize the lowest energies too much, we set
 1588 $E_{\max} = 2E_i$ in Eq B4.

1589 There are two possibilities to define dM/dE . Since the main origin of the systematic error is the
 1590 diffuse emission, we can restrict dM/dE to the diffuse emission model only (we call the result model-
 1591 based weights). On the other hand there are also systematic uncertainties on sources due to PSF
 1592 calibration and our imperfect spectral representation, so another option is to enter the full model (or
 1593 the data themselves) into dM/dE (we call the result data-based weights). That second choice limits
 1594 spurious sources next to bright sources. There is of course no reason why the level of systematics ϵ
 1595 should be the same for the diffuse emission model and the sources, but in practice it is a reasonable
 1596 approximation.

1597 Another important point, for the procedure to be stable, is that the weights should not change
 1598 with the model parameters. So dM/dE must be defined beforehand (for example from a previous
 1599 fit). In this work we use data-based weights computed from the data themselves, with a common ϵ .
 1600 The data are not as smooth as the model, but this is not a problem in the regime of large counts
 1601 where weights play a role.

1602 We assume here that ϵ is a true constant (it depends neither on space nor on energy). For a given
 1603 ϵ the weights are close to 1 at high energy and decrease toward low energy. At a given energy the
 1604 weights are smallest where the model is largest (in the Galactic ridge). Considering all event types
 1605 (not what we do in 4FGL), for 8 years and $\epsilon = 3\%$, at 100 MeV the weights are everywhere less than
 1606 12%. They reach 50% at high latitude at 250 MeV, and 90% at 500 MeV. In the Galactic ridge, the
 1607 weights are 0.5% at 100 MeV, 1.5% at 250 MeV, 5% at 500 MeV, 20% at 1 GeV, 60% at 2 GeV and
 1608 reach 90% at 4.5 GeV.

1609 There remains a specific difficulty, due to the fact that at a given energy we split the data into
 1610 several components, each corresponding to a particular event type (with a different PSF). Since the
 1611 systematics play in the same way on all components, the weights must be computed globally (i.e.,
 1612 weights must be lower when using PSF2 and PSF3 events than when using PSF3 alone). On the
 1613 other hand, the resulting uncertainties with two components should be smaller than those with a
 1614 single component (adding a second one adds information). In this work, we started by computing
 1615 weights w_k individually for each component k (the dependence on E and \mathbf{r} is left implicit). Then we
 1616 assumed that the final weights are simply proportional to the original ones, with a factor $\alpha < 1$ (α
 1617 depends on E and \mathbf{r} as well). A reasonable solution is then

$$N_{\min} = \min_k N_k \quad (\text{B6})$$

$$K_{\text{tot}} = \sum_k \left(\frac{N_{\min}}{N_k} \right)^2 \quad (\text{B7})$$

$$\alpha = \frac{1 + \epsilon^2 N_{\min}}{1 + \epsilon^2 N_{\min} K_{\text{tot}}} \quad (\text{B8})$$

$$w_k = \frac{\alpha}{1 + \epsilon^2 N_k} \quad (\text{B9})$$

¹⁶¹⁸ K_{tot} and α are 1 if one component dominates over the others, and K_{tot} is the number of components
¹⁶¹⁹ if they are all similar.